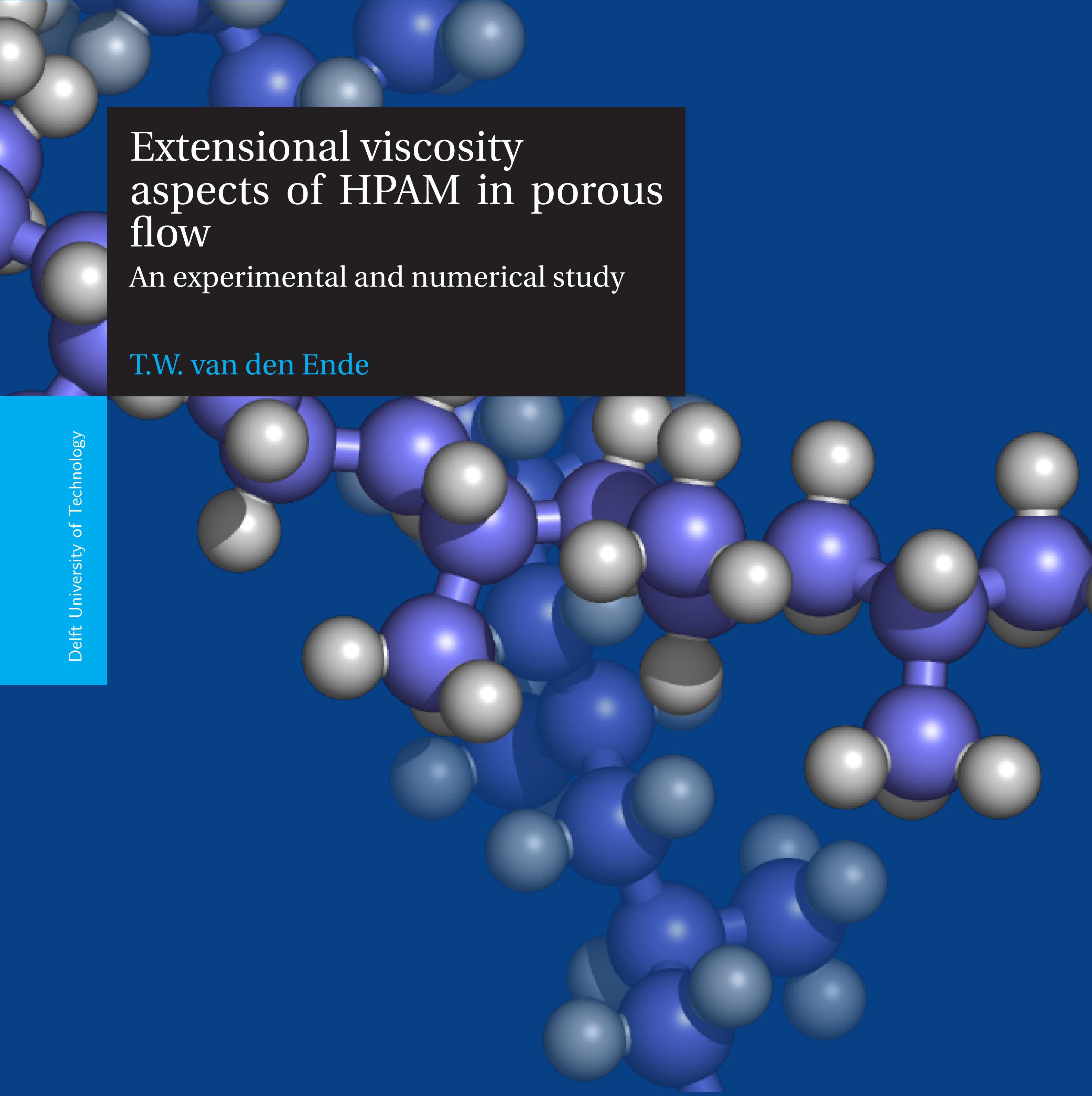

Extensional viscosity aspects of HPAM in porous flow

An experimental and numerical study

T.W. van den Ende

Delft University of Technology

EXTENSIONAL VISCOSITY ASPECTS OF HPAM IN POROUS FLOW

AN EXPERIMENTAL AND NUMERICAL STUDY

by

T.W. van den Ende

in partial fulfilment of the requirements for the degree of

Master of Science
in Applied Physics

at the Delft University of Technology,
to be defended publicly on Friday July 3, 2015 at 2:00 PM.

Professor:	Prof. ir. C.P.J.W. van Kruijsdijk,	TU Delft/Shell
Supervisor:	Dr. M. Welling,	Shell
Thesis committee:	Prof. dr. J. Bruining,	TU Delft
	Dr. J. Romate,	TU Delft/Shell

ABSTRACT

Polymer flooding is the most widely used chemical EOR method. Despite being widely used, the apparent shear-thickening behaviour of the polymer solutions in porous flow at high flow rates is poorly understood. One of the supposed mechanisms is the strain-thickening behaviour of polymer solutions. This fluid property will alter the flow dynamics during porous flow compared to Newtonian and purely shear-thinning flow. In this research, the objective is to improve our understanding of polymer flow through a simple single slit geometry (e-VROC) and more complex geometries (porous flow characterised by pore network models) in order to allow oil recovery optimisation for polymer flooding.

The intrinsic viscosity of HPAM3630S is investigated experimentally using the Extensional Viscometer/ Rheometer On a Chip (e-VROC). The e-VROC has a microfluidic hyperbolically-shaped contraction-expansion geometry. The water salinity is used as a control parameter to reduce the fluid viscosity. Initial calibration of the device with Newtonian fluids and analytical analysis of the e-VROC geometry indicate that the shear component of the flow is large in the converging section – contrary to the claimed advantages of the hyperbolic geometry. Newtonian flow can therefore not be regarded as extension dominated. Consequently, the provided analysis of the e-VROC pressure data is currently unable to determine the true extensional viscosity of a Newtonian fluid. Therefore the analysis should be regarded as an extensional viscosity indexer in comparing different fluids.

For polymer flow the pressure gradient over the contraction-expansion area increases more than linearly with increasing flow rate. This indicates strain-thickening behaviour. The salinity highly impacts the amount of strain-thickening; the higher the brine salinity the lower the pressure gradient over the contraction-expansion area. Furthermore, a high noise content in the time-pressure signal is observed together with reproducibility problems regarding polymer flow. Differences upto 30% in pressure gradients between measurements are reported for the same fluid. Both can probably be attributed to elasticity due to the short residence time of the polymer solutions in the contraction-expansion geometry compared to their relaxation times.

The fluid flow process is modelled using finite element modelling (GeoDict&COMSOL) and pore network modelling using MATLAB to study the (changed) fluid flow behaviour. It was shown that Newtonian flow through the e-VROC can be modelled using both COMSOL and GeoDict. Furthermore, it was shown that the pressure drop due to pure shear losses in the e-VROC can be significant during polymer flow.

The developed Matlab code enables modelling the steady state response of pore network systems. The systems contains more than 10000 non-linear throat equations. This captures both extension-thickening and shear-thinning pressure losses. This successfully demonstrates proof of concept set out at the beginning of this study. Using the pore network model, it is studied how a macroscopic pressure over a rock sample is redistributed in microscopic pressure drops between individual pores. It is shown that the microscopic pressure drop distribution for Newtonian flow predicted by the pore network model is in good agreement with the microscopic pressure drop distribution inside the porous medium predicted by GeoDict. However, the corresponding permeability predicted by the pore network modelling is one order of magnitude too low. From this it can be concluded that the resistance to flow between the pores is overestimated by the used transport equations. Nevertheless, a qualitative interpretation of the (changed) microscopic redistribution of pressure for non-Newtonian flow can still be made.

Secondly, the microscopic pressure drop distribution within the sample for purely shear-thinning flow is compared to Newtonian flow. The variance and kurtosis of the distribution decrease compared to Newtonian flow. This implies better conformance control during using purely shear-thinning flow. Above a critical flow rate, strain-thickening behaviour reverses this process. The variance and kurtosis of the pressure drop distribution increase. This has a negative impact on conformance control.

PREFACE

The first time I stepped into Cors office to discuss my graduation project, he told me he would try to challenge me. I am confident enough to say that he succeeded. From time to time it felt like a roller coaster ride, with ups and downs and the occasional corkscrew that made it difficult to see where I was heading. But I have to admit that I am happy with the final result and can say that I have learned a lot the past months. On an academic level but mostly on a personal level. I have learned that with perseverance and the right amount of guidance that I am able to tackle a problem that "challenges" me. I have enjoyed being part of the RO team with all these experienced and knowledgeable people.

Special thanks goes out to my supervisor Marco for his willingness to guide me through this project. Coming up with countless of ideas to improve the experimental and numerical work. Although I could not incorporate all of them, I think I picked up the most essential ones.

I would also like to thank Johan for his help on my numerical work. I still remember how I told him that I wanted to write a pore network solver that could solve non-linear flow with two exponents. And that I ignorantly planned to have a working algorithm in a month or so. He told me it probably would take some extra time; four months later he turned out to be right.

Furthermore, I would like to thank Cor for his guidance during my project. Despite all the ups and downs you were always confident that I would be able to tackle the problems and kept me on the right track. Besides Cor, Marco and Johan I would like to thank Steffen, Evren, Menno, Merit, Michael and Boaz for all the help with either the experiment or the modelling.

Also I would to thank Shell Global Solutions and the people within the RO department for giving me the opportunity to work within a major oil and gas company. Because of this opportunity I have developed my technical skills, but most of all my non-technical skills.

Last but not least, I would like to thank my fellow interns for the discussions, talks, laughs, lunches, cups of coffee and games of pool.

Thank you all.

"The purpose of mathematical programming is insight, not numbers."
Richard Hamming

T.W. van den Ende,

Rijswijk, June 2015

CONTENTS

1

INTRODUCTION

1.1. OIL RECOVERY

Rising living standards and growing population increase the global demand for energy. It is estimated that the world's population will grow from around 2 billion people to 9 billion by the middle of the century. Due to this population growth the global energy demand will increase around 60% by 2050 [1]. The global primary energy supply in 2012 is given in Figure 1.1 [2].

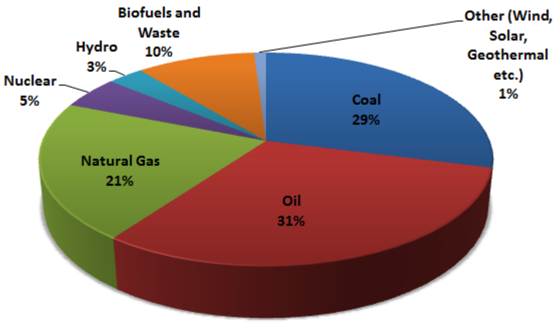

Figure 1.1: Global primary energy supply in 2012.

Approximately one third of the primary energy supply consists of oil. Although in the future more and more of the energy will come from renewables, most of the energy will still come from oil and gas [1]. To meet this demand for oil and gas, new reserves should be unlocked. Both by drilling and exploration campaigns and increasing the oil recovery in existing assets.

The conventional techniques for extracting oil include primary and secondary recovery. During primary recovery, oil production relies on the natural energy of the reservoir. This consists of three mechanisms: the aquifer drive, the gas cap drive and gravity flow. Over time the reservoir pressure decreases due to the extraction of the reservoir fluids (oil, gas and water) resulting in lower production rates. With time, the remaining natural energy in the system will not be sufficient to produce the oil to surface. Typically between 5-15% of the oil initial in place (OIIP) is recovered by primary recovery depending on the oil reservoir [3].

Secondary recovery involves the injection of water or gas into the reservoir, hence external energy is added to the system. Waterflooding is the most applied secondary recovery method with the main purpose to maintain reservoir pressure, thereby maintaining oil production rates and increasing oil recovery. However, after a certain time the injected water breaks through in the production wells and water production increases as production continues, resulting in less efficient oil production. On average secondary recovery methods have a recovery factor of 30-50% of the OIIP [3]. Although in the North Sea the recovery factors are between 45-55% of OIIP after secondary recovery [3].

1.2. ENHANCED OIL RECOVERY

Enhanced oil recovery (EOR) methods are recovery techniques in which substances are injected which are not naturally occurring in the reservoir [4]. These techniques can be subdivided in two main groups: Thermal and non-thermal methods. This thesis focusses on a non-thermal method, more specifically polymer flooding. Thermal methods are best suited for very viscous oil reservoirs. Non-thermal methods mainly use gas or chemicals (polymers and surfactant) to increase the oil recovery. Polymer flooding is the most used chemical EOR method.

1.2.1. POLYMER FLOODING

During waterflooding not all of the OIIP is contacted by the waterflood. This can be expressed by the volumetric sweep efficiency, E_V (Equation 1.1).

$$E_V = \frac{\text{Volume of oil contacted by displacement fluid}}{\text{Volume of oil initial in place}} \tag{1.1}$$

While displacing a viscous fluid (oil) using an immiscible less viscous fluid (water), the interface between these fluids is unstable and viscous fingering occurs (Figure 1.2). This effect causes a low sweep efficiency of the reservoir, leaving large volumes of oil behind. This problem can be solved by optimizing the water-oil mobility ratio [4] (Equation 1.2), which depends on the relative permeability of water and oil in the porous medium, k_w and k_o respectively, and their viscosity (μ_w and μ_o).

$$M = \frac{k_w}{k_o}\frac{\mu_o}{\mu_w} \tag{1.2}$$

For a water-oil mobility less than or equal to 1 the flow is more piston like and the sweep efficiency is increased. At high mobility ratios viscous fingering occurs and volumetric sweep efficiency can be low. However, it also depends, among others, on the heterogeneity of the reservoir, gravity and well locations. During a polymerflood, polymer is added to the water of a waterflood. The polymer molecules increase the viscosity of the water and hereby decrease the mobility ratio. This lowering causes more of the OIIP to be contacted by the polymerflood as compared to a waterflood, therefore more oil is mobilized to flow to the production well (Figure 1.2).

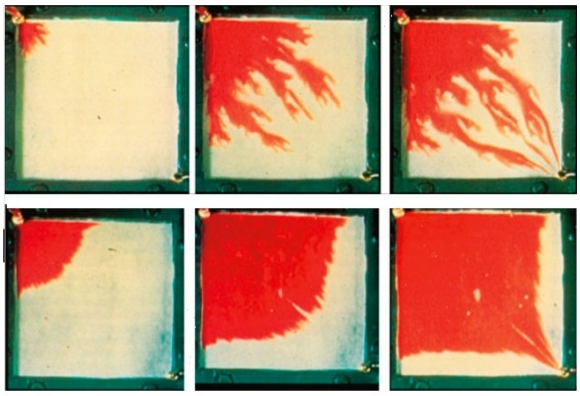

Figure 1.2: Viscous fingering of water (top) and polymer - more piston-like - flow (bottom) (modified from [5]).

1.3. POLYMERS SOLUTIONS

Roughly two types of polymer solutions for EOR exist: Synthetic polymers (PAM and HPAM) and biopolymers (e.g. xanthan). Synthetic partially hydrolysed polyacrylamides (HPAM) are the most widely used polymers in polymer flooding. The chemical structure of HPAM is shown in Figure 1.3. Generally, the degree of hydrolysis is between 25-30% [4]. Due to its long flexible coil structure, the molecules can be deformed while flowing through the porous reservoir rock. Unlike water, polymer solutions are non-Newtonian; they cannot be characterized by one viscosity value since the viscosity depends on the rate of shear stress e.g. flow rate through the porous medium. Generally, the viscosity of polymer solutions decreases with increasing shear stress, so-called shear-thinning behaviour. This behaviour is observed because the polymer molecules uncoil and align with the shear flow [4]. However, in a porous flow polymer solutions experience both compression and extensional forces. This affects the fluids apparent viscosity and may cause the apparent behaviour to alter. Previous research has shown that HPAM solutions exhibit apparent shear thickening behaviour in porous flow above a critical flow rate [6–8]. Xanthan solutions do not show this behaviour [9].

When the partially hydrolysed polymers (charge bearing) are dissolved in water containing salts a reduction in shear viscosity is observed, compared to water that does not contain salts. The loss of shear viscosity is attributed to the shielding effect of the electric repulsion between the polymer coils. Consequently the hydrodynamic volume is reduced resulting in a reduction off the shear viscosity (Figure 1.4).

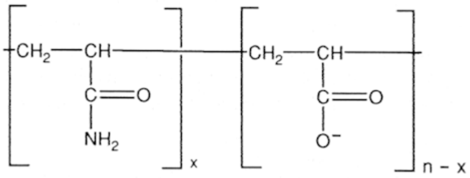

Figure 1.3: Chemical structure of HPAM.

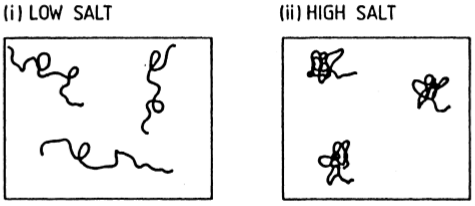

Figure 1.4: The effect of in the hydrodynamic volume of a polymer coil affecting its viscosity [10].

1.4. AIM AND SCOPE OF THIS THESIS

In this research, the objective is to improve our understanding of polymer flow through a simple single slit geometry (e-VROC) and more complex geometries (porous flow characterised by pore network models) in order to allow oil recovery optimisation for polymer flooding.

Firstly, the intrinsic viscosity is investigated experimentally using a microfluidic flow device (e-VROC). The experimental objective was to test and characterise polymer solutions flowing through the e-VROC for quantifying the pressure losses due to shear-and elongational-stress in order to improve our understanding of fluid properties. After the use of calibration fluids, HPAM polymer (FP3630S) is used and the water salinity is used as a control parameter to reduce the fluid viscosity.

Secondly, the fluid flow process is modelled using finite element modelling (GeoDict & COMSOL) and pore network modelling using MATLAB to study the (changed) fluid flow behaviour. The modelling objective was to develop a framework in MATLAB to calculate the total system pressure-rate steady state response of pore network systems. The systems should contain more than 10000 non-linear throat equations for single-phase flow. This should capture both extension-thickening and shear-thinning pressure losses. The model serves as a proof of concept for a very simplified polymer fluid flowing through a porous medium incorporating both the shear and extensional behaviour of polymer solutions.

This thesis report is subdivided into five parts. The first part covers the theoretical concepts, governing the flow of polymer solutions through porous media (Chapter 2). Secondly, the materials and methods used to improve our understanding and predictability of polymer flow through a pore throat are described in Chapter 3. Chapter 4 discusses the results of the flow experiments. Chapter 5 compares the experimental and numerical (Geodict & COMSOL) results of the flow experiments. Furthermore, the pore network modelling (MATLAB) and its results is explained in more detail. Finally, the conclusions and recommendations drawn from the results are given in Chapter 6 and 7.

2

THEORETICAL CONCEPTS

Polymer solutions are Non-Newtonian fluids; the relationship between stress and rate of strain is non-linear or an initial yield stress is present. Non-Newtonian fluids can be divided in three groups [11]:

1. **Time-independent fluids**: The strain rate is only dependent on the instantaneous stress.
2. **Viscoelastic fluids**: Fluids that have both properties of viscous fluids and elastic solids, therefore they show (partial) elastic recovery when the deforming stress is removed.
3. **Time-dependent fluids**: Apart from the magnitude of the deforming stress, the strain rate is also dependent on the duration of the deforming stress. They may also be dependent on the time between two subsequent deforming stresses.

Polymer solutions are generally classified as viscoelastic time-dependent fluids, since these fluids show elastic recovery upon deformation and because the strain rate is a function of the time between two subsequent deforming stresses. Both the viscous and elastic behaviour of the polymer solutions contribute to the resistance to flow due to the contraction-diverging geometry of porous media.

Understanding the complex rheology of polymer solutions is essential to know how the fluid will perform under porous flow conditions. The fluid's extensional viscosity can be several magnitudes higher than the corresponding shear viscosity at high flow rates (near wellbore). This can be decisive in the performance of a polymer flood, since it is likely to dominated the injection pressure response near the wellbore.

2.1. FLUID DYNAMICS AND RHEOLOGY

The motion of fluid can be described by the Cauchy equations. Applying Newton's second law, conservation of momentum, a general form is given by [12]:

$$\rho \frac{\partial \mathbf{u}}{\partial t} + \rho \mathbf{u} \cdot \nabla \mathbf{u} = -\nabla p + \nabla \cdot \mathbf{T} + \mathbf{f} \tag{2.1}$$

where ρ the density of the fluid, $\mathbf{u}$ is the fluid velocity, $\mathbf{p}$ the pressure tensor, $\mathbf{T}$ the stress tensor and $\mathbf{f}$ the body forces acting on the fluid such as gravity. If the velocity field can be linked to the deviatoric stress by a constitutive relation, these equations can be solved. For an incompressible Newtonian fluid, the stress tensor $\mathbf{T}$ in Equation 2.1 can be replaced with Newton's law, reducing it to the Navier-Stokes equations:

$$\rho \frac{\partial \mathbf{u}}{\partial t} + \rho \mathbf{u} \cdot \nabla \mathbf{u} = -\nabla p + \eta \nabla^2 \mathbf{u} + \mathbf{f} \tag{2.2}$$

in which η is the viscosity of the fluid. However, many fluids show Non-Newtonian behaviour and other constitutive laws have to be used, such as generalized Newtonian models [13]. For a generalized Newtonian fluid, the shear stress depends on the shear rate at a given time but is independent of the history of deformation [13, 14]:

$$\mathbf{T} = 2\eta(\gamma)\mathbf{E} \tag{2.3}$$

where γ is the shear rate and $\mathbf{E}$ is the strain tensor and given by[13]:

$$\mathbf{E} = \frac{1}{2}(\nabla\mathbf{u} + \nabla\mathbf{u}^T) \tag{2.4}$$

in which $\mathbf{u} + \nabla\mathbf{u}^T$ is the rate of deformation tensor. The deformation tensor describes both rotation and stretching of the fluid.

However, since polymer solutions have a memory regarding deformation history, Equation 2.3 cannot accurately describe the stress tensor when the polymer solution is subjected to two subsequent deforming stresses. No model yet exists that describes all visco-elastic phenomena of polymer solutions (shear-thinning, extension-thickening, normal stresses and time dependence), however most existing models account for time-dependence with characteristic time parameters that represent the memory of the fluid. The most popular model that includes the history of deformation is the Oldroyd-B model [15]:

$$\mathbf{T} + \tau_r \overset{\triangledown}{\mathbf{T}} = 2\eta\left(\mathbf{E} + \tau_{rt}\overset{\triangledown}{\mathbf{E}}\right) \tag{2.5}$$

where τ_{rt} is the retardation time, $\overset{\triangledown}{\mathbf{T}}$ and $\overset{\triangledown}{\mathbf{E}}$ are the rate of change of the stress and deformation tensors of a small parcel of fluid respectively. The so-called upper-convected time derivatives are defined as:

$$\overset{\triangledown}{\mathbf{T}} = \frac{\partial}{\partial t}\mathbf{T} + \mathbf{u}\cdot\nabla\mathbf{T} - ((\nabla\mathbf{u})^T\cdot\mathbf{T} + \mathbf{T}\cdot(\nabla\mathbf{u})) \tag{2.6}$$

$$\overset{\triangledown}{\mathbf{E}} = \frac{\partial}{\partial t}\mathbf{E} + \mathbf{u}\cdot\nabla\mathbf{E} - ((\nabla\mathbf{u})^T\cdot\mathbf{E} + \mathbf{E}\cdot(\nabla\mathbf{u})) \tag{2.7}$$

Although viscoelastic shear flow is adequately described by the model, at some extensional rates the calculated extensional viscosities are non-physical. This problem arises since the Oldroyd-B model is derived using infinitely extensible Hooke's Law springs. If the strain tensor can be linked to the stress tensor by a constitutive relation the Olderoyd-B model can be used together with the Cauchy equation (Equation 2.1) to solve these equations.

2.1.1. SHEAR FLOW

The typical behaviour of the shear viscosity of polymer solutions is depicted in Figure 2.1. After an initial Newtonian plateau at low shear rates, polymer solutions experiences shear-thinning behaviour at increasing shear rate. If the shear rate is increased even more a second plateau is reached, referred to as the upper Newtonian plateau. Many different fluid models exist to describe this behaviour [11, 16]. Of these methods the Carreau-Yasuda is most frequently used since it can accurately describe the shear-thinning as well as the lower and upper Newtonian plateaus:

$$\eta = \eta_\infty + (\eta_0 - \eta_\infty)[1 + (\lambda\gamma)^\alpha]^{(n-1)/\alpha} \tag{2.8}$$

in which η_0 and η_∞ are the limiting Newtonian viscosities at zero and infinite shear rate respectively, λ and n are fluid specific empirical constants; α is generally taken to be 2.

2.1.2. EXTENSIONAL FLOW

Besides shear forces, a fluid also experiences extension during porous flow. The resistance to extension is called extensional or elongational viscosity. The extensional behaviour of HPAM solutions, as opposed to shear, is typically strain-hardening as depicted in Figure 2.2. At low extensional rates, the elongational viscosity is constant, the so-called zero-extension rate extensional viscosity. This extensional viscosity is equal to that of a Newtonian fluid. Increasing the extensional rate results in a strain-hardening effect. At high extensional rates, the extensional viscosity reaches a second plateau. If the rate is increased even more the polymer chains will break and therefore the extensional viscosity will decrease. It also should be noted that polymer solutions that show the same shear response do not necessarily show the same extensional behaviour [17].

Furthermore, the extensional viscosity depends on the type of extension e.g. uniaxial, equibiaxial or planar extension and therefore on the geometry of the contraction (Figure 2.3). Generally, the rate of strain tensor for extension can be written as [17–19]:

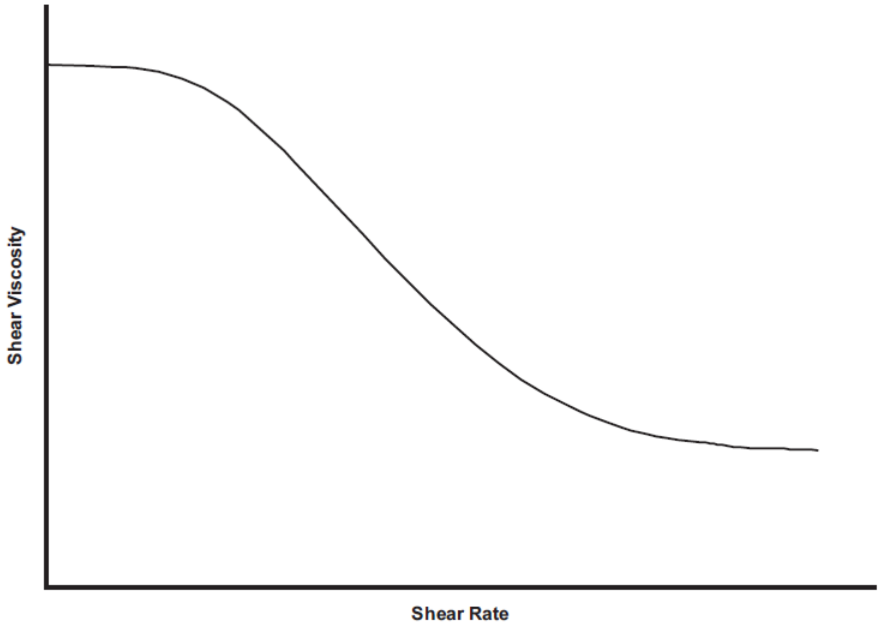

Figure 2.1: Schematic of the shear-thinning behaviour of polymer solutions on log-log scales [11].

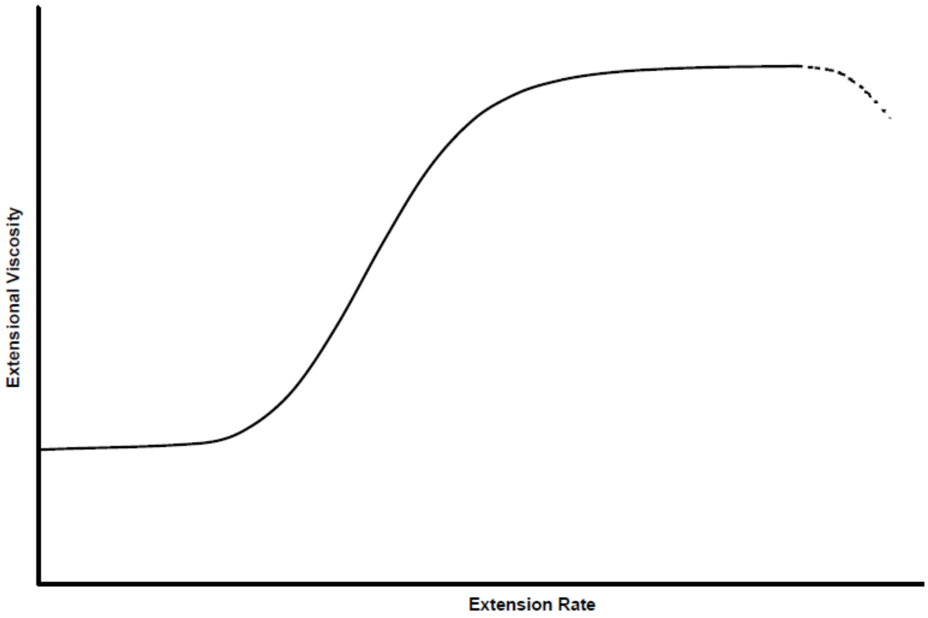

Figure 2.2: Schematic of the behaviour of polymer solutions under extensional flow on log-log scales [11].

$$\mathbf{E} = \epsilon \begin{bmatrix} 1 & 0 & 0 \\ 0 & m & 0 \\ 0 & 0 & -(1+m) \end{bmatrix} \tag{2.9}$$

where ϵ is the largest principal strain rate and the parameter m describes the geometry of the extensional flow, with $-\frac{1}{2} \leq m \leq 1$ in general. For three standard cases, uniaxial, equibiaxial and planer extension, the parameter m equals $-\frac{1}{2}$, 1 and 0 respectively. The extensional viscosity is defined as the ratio between tensile stress and extensional rate under steady flow conditions:

$$\eta_E = \frac{\tau_{11} - \tau_{22}}{\epsilon} = \frac{N_1}{\epsilon} \tag{2.10}$$

The extensional viscosity of polymer solutions is non-constant in both steady and unsteady extensional flow [11]. However, the extensional viscosity of polymer solutions as function of elongation rate can be described as a power-law [14, 20]:

$$\eta_E = B\epsilon^{k-1} \tag{2.11}$$

with B the consistency index or the extensional viscosity of the polymer solution at a shear rate of $1s^{-1}$ and $k > 0$ is the power-law exponent of extensional viscosity. Strain-thickening and strain-thinning are indicated by $k > 1$ and $k < 1$ respectively. For isotropic, incompressible Newtonian fluids, $k = 1$, this corresponds to an extensional viscosity η_E of $3\eta_{sh}$ for uniaxial extension [14, 18, 21], $6\eta_{sh}$ for equibiaxial extension [18] and $4\eta_{sh}$ for planar extension [14, 18].

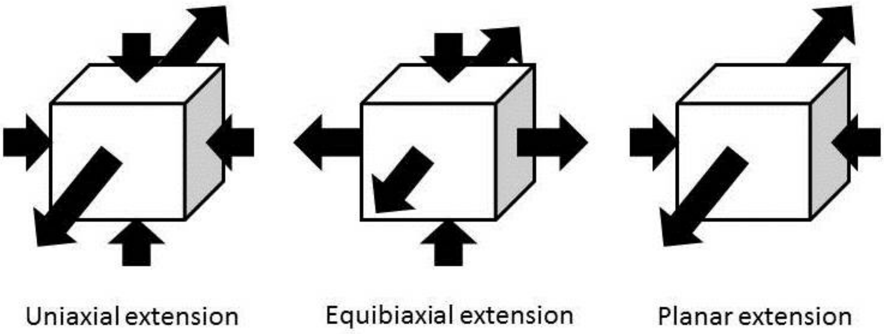

Figure 2.3: Schematic representation of uniaxial, equibiaxial and planar extension.

2.1.3. MIXED FLOW

Unfortunately, it is experimentally not possible to generate an extensional flow without any shear component [14, 22]. Especially for converging dies, where a shear flow component is inevitable due to the no slip boundary at the channel wall. In so-called mixed flows, both shear and elongational viscosity contribute to the resistance to flow. In view of the geometrical dependency and the fact that purely elongational flow is almost never achieved, the viscometers provide *an* extensional viscosity rather than *the* extensional viscosity.

To describe the resistance to flow under mixed flow conditions, it can be assumed that both viscosity effects are additive, although this is not strictly valid [14, 19, 22]:

$$\eta = \eta_{sh} + \eta_E \tag{2.12}$$

According to Wunderlich [14] the polymer dynamics can be altered considerably by a combination of shear and extensional flow, thereby undermining the additivity assumption. Adding a shear component to a purely extensional flow could have two effects [14]:

1. The polymers get stretched and aligned by the shear component in the direction of flow. Consequently, the polymers are subjected to larger frictional forces, so that the apparent extensional viscosity is increased.

2. Oppositely, the shear flow component rotates the polymer molecules out of the alignment relative to the extensional flow. Due to this tumbling, the polymers are less stretched in the extensional flow direction, hereby reducing the apparent extensional viscosity.

The predominate effect is determined by the relative magnitudes of shear and extensional flow and their relative orientation. Depending on the relative magnitudes of extension due to shear and extensional flow, three regimes can be recognized [14]:

1. **Extension dominated regime**: The shear components only have a minor impact on the flow, consequently the additional friction can be neglected. In this regime the apparent extensional viscosity is approximately equal to the extensional viscosity in purely extensional flow.
2. **Extension comparable to shear**: Depending on the relative orientation of extension due to shear and extensional flow, the apparent extensional viscosity can be larger or smaller than the extensional viscosity in purely extensional flow. Resulting from the mechanisms explained above.
3. **Shear dominated regime**: The polymers are subjected to large frictional forces due to their stretching and alignment in the extensional flow direction, hereby increasing the apparent extensional viscosity.

Since polymer solutions are visco-elastic fluids, it can be argued that an extra resistance to flow is introduced by elastic storage [20]. For polymer solutions this resistance is again a power-law function of deformation rate, while for Newtonian fluids it equals zero:

$$\psi = p\gamma^{q-1} \tag{2.13}$$

However, if the contraction-expansion geometry is symmetrical, the elastic contribution cancels out. The elastic energy stored by contraction is fully released when the solution expands again.

2.1.4. IN-SITU RHEOLOGY

Although polymer solutions commonly show shear-thinning behaviour for bulk experiments, a dilatant behaviour is observed above a certain rate in porous media (Figure 2.4). This strain hardening region can be attributed to either the extensional viscosity or the memory of polymer solutions. At low flow rates the viscosity and elasticity behaviour is almost the same as in bulk. Therefore the pressure response is mainly determined by shear viscosity. However, when the flow rate is increased the apparent in-situ rheology is significantly different. Because of the more dominant visco-elastic effects the polymer solutions show dilatant behaviour. There is not really agreement in literature at which flow rate the visco-elatic effect becomes dominant. However, it is agreed that they become important when the fluid is significantly deformed in a time comparable to the relaxation time of the fluid. The quantification of these phenomena are further enhanced by the simultaneous occurrence of polymer adsorption, retention and partial pore blockage, which also cause pressure drops to exceed their expected value [11]. While examining visco-elasticity in porous media, three principal effects have to be considered: transient time-dependence, steady-state time-dependence and dilatancy at high flow rates.

TRANSIENT TIME-DEPENDENCE

After starting or ending the displacement of polymer solutions, transient time-dependent behaviour is observed. During this period, overshoots and undershoots of stress are observed before the fluid reaches a constant value if the strain is kept constant (Figure 2.5).

STEADY-STATE TIME-DEPENDENCE

Depending on the relaxation time of the polymer solution and the time scale of the flow, the fluid may show elastic or viscous behaviour. Therefore flow in pores media can be characterized by the fluid relaxation time and average residence time of the fluid inside the pore throat. The Deborah number is defined as the ratio of the time it takes for a material to adjust to an applied stress and the characteristic time scale of an experiment:

$$De = \frac{\tau_r}{\tau_E} \tag{2.14}$$

where τ_r the relaxation time of the polymer solution and τ_E the average residence time. If $De \ll 1$ the flow is purely viscous, if $De \gg 1$ the flow is elastic.

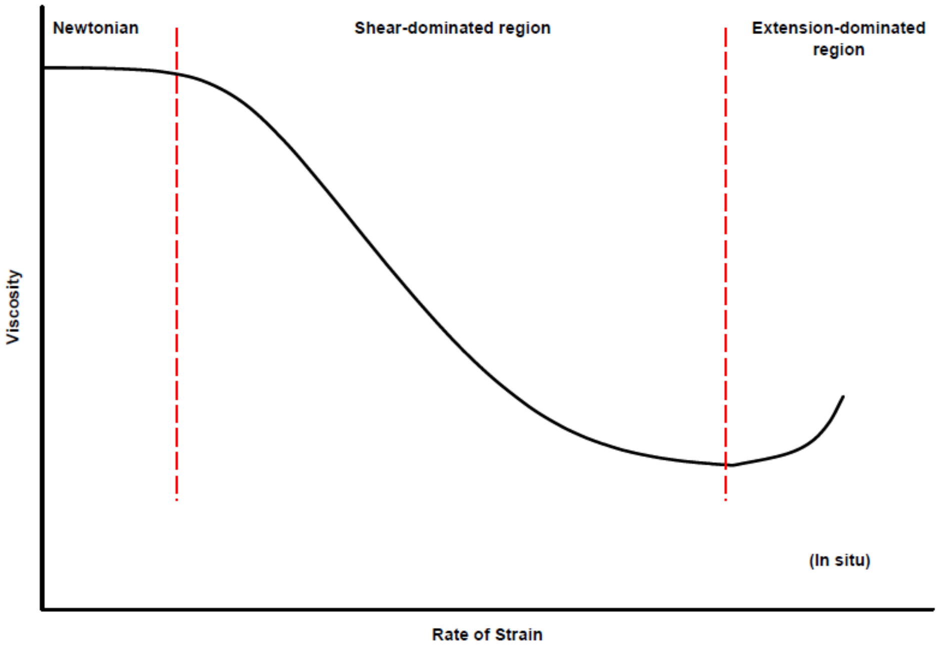

Figure 2.4: Schematic of the behaviour of polymer solutions in porous media [11].

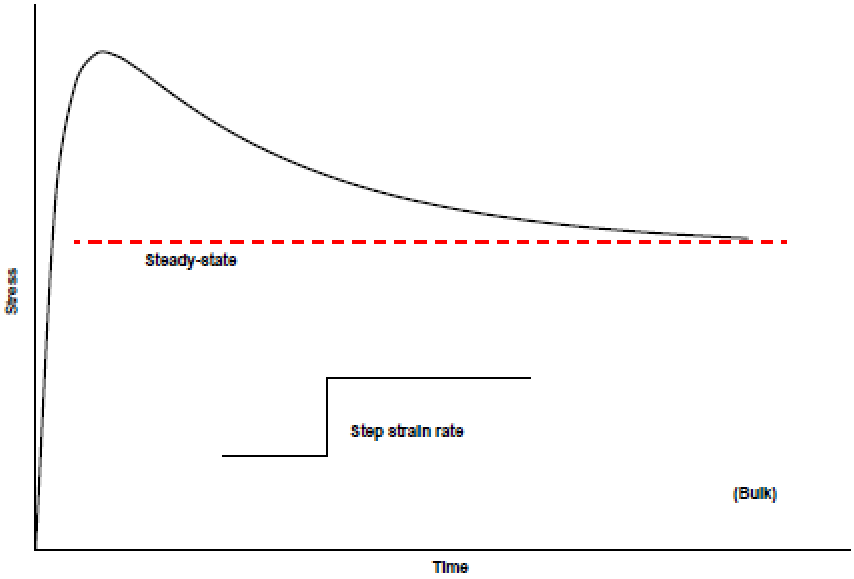

Figure 2.5: Schematic of the time dependence behaviour of polymer solutions after a step increase in flow rate [11].

Assuming the reciprocal value of the (effective) shear rate is a good approximation of the average residence time τ_E [23], the Deborah number in Equation 3.18 can be written as [6]:

$$De \equiv \frac{\tau_r}{\tau_E} = \tau_r \gamma_{eff} \tag{2.15}$$

Others [24, 25] approximate the average residence time by the reciprocal value of the extension rate:

$$\tau_E = \frac{1}{\epsilon} \tag{2.16}$$

If the transit time through a pore throat is large compared to the relaxation time of the polymer solution, no elastic effects will occur since the fluid has enough time to adjust to the changing flow field. However, if the residence time is small compared to the relaxation time, the fluid does not have time to adjust to the new flow conditions and elastic effects will occur. These elastic effects are then observed as an extra pressure drop.

Dilatancy at High Flow Rates

Dilatant behaviour is observed above a certain rate in porous media (Figure 2.4). This strain hardening region can be attributed to the memory of polymer solutions, the extension viscosity or both. The dominance of extension is further enhanced by the shear-thinning behaviour of polymer solutions. As flow rate is increased the resistance due to shear will drop, whereas the extensional viscosity will increase. As a consequence the observed resistance will be governed by strain-thickening.

Different empirical models have been proposed to describe extensional viscosity given by Equation 2.12 in porous media. All are functions of the dimensionless Deborah number and assume that the additivity of shear viscosity and extension viscosity is valid.

The model by Hirasaki and Pope [24]:

$$\eta_E = \frac{\eta_{sh}}{1 - De} \tag{2.17}$$

where De is the Deborah number.

Masuda's proposed the model [23]:

$$\eta_E = \eta_{sh} C_c De^{m_c} \tag{2.18}$$

in which C_c and m_c are empirical constants.

The model proposed by Delshad et al [6]:

$$\eta_E = \eta_{max}[1 - \exp(-(\lambda_2 De^{n_2 - 1})] \tag{2.19}$$

where η_{max}, λ_2 and n_2 are polymer-specific empirical constants.

2.2. Oscillatory Rheometry

The relaxation time, τ_r, for polymer solutions can be determined by oscillatory experiments. In these experiments a sinusoidal stress is applied by the rheometer. The resulting strain in the fluid sample can be divided into two parts: An in phase (elastic) and out of phase (viscous) response. This data provides information on energy storage and dissipation, respectively the storage modulus G' (pronounced G prime) and loss modulus $G"$ (pronounced G double prime). Together they form the complex modulus G^* as function of frequency:

$$G^* = G' + iG" \tag{2.20}$$

As stated above, the G' is a measure of the energy stored by the sample during deformation. If the stress on the fluid sample is removed this stored energy is released. This will (partially) restore the fluid to its preloaded condition. Therefore, the storage modulus described the elasticity of the fluid sample [26].

The loss modulus on the other hand describes the energy used in deforming the fluid sample. During the deformation energy is dissipated and therefore the deformation is irreversible. Thus, $G"$ describes the viscous behaviour of the fluid sample [26]. For ideally viscous flow behaviour $G' \to 0$, for ideally elastic flow behaviour $G" \to 0$ and viscoelastic flow behaviour is characterized by $G" > G'$ [26]. For a Newtonian fluid, $G' = 0$ and $\eta = \frac{G"}{\omega}$, where ω is the frequency [13].

It is proposed that the inverse of the frequency at which G' and $G"$ cross, is the relaxation time of the polymer solution [6, 7, 17, 27]. Since polymer solutions have a certain molecular weight distribution, the solution cannot be characterized by one relaxation time. Many different models exist to obtain the spectrum of relaxation times [6, 17, 28]. However, one relaxation time will be dominating since the spectrum will have a peak corresponding to the most common polymer molecule size. From the existing models the Cross-Over Point model and Rouse model are the most widely used.

Cross-Over Point Model It is suggested that the cross-over frequency between G'and G" indicates the relaxation time since they represent the elastic and viscous components respectively. The relaxation time is obtained by the inverse of the cross-over frequency.

Rouse Model If the polymer coil is described as a series of equally spaced beads and springs the relaxation spectrum is obtained by:

$$G' = \frac{c_p RT}{M} \sum_{i=1}^{N} \frac{\omega^2 \tau_i^2}{1+\omega^2 \tau_i^2} \tag{2.21}$$

$$G" = \frac{c_p RT}{M} \sum_{i=1}^{N} \frac{\omega \tau_i}{1+\omega^2 \tau_i^2} \tag{2.22}$$

where c_p is polymer concentration, t_i the relaxation times.

3

MATERIALS AND METHODS

First this chapter describes the materials used in the different experiments in section 3.1. Secondly, the concepts of the devices used in the experiments are described in section 3.2.

3.1. EXPERIMENTAL FLUIDS

Both calibration and polymer fluids were used during the experiments. This section describes which fluids and how they were prepared.

3.1.1. CALIBRATION FLUIDS

For calibration of the e-VROC (Extensional Viscometer/Rheometer On a Chip) multiple Newtonian calibration fluids of different viscosity were used (Section 3.2.2). The fluids consisted of a glycerol-water solution, olive oil and two silicon oils (Fluid 50 and Fluid 100) made by Brookfield, with serial numbers 033111 and 101786 respectively.

3.1.2. PREPARATION OF POLYMER SOLUTIONS

Three different polymer solutions were made (Table 3.1) in which the polymer type and concentration were kept constant and only the salinity was varied, no divalent salts were added to the brines. Note that the number in the name of the solutions indicates the salinity of the fluid.

Name Solutions	Polymer Type	Polymer Concentration [ppm]	NaCl concentration [ppm]
FP2500	FP3630S	1500	2500
FP5000	FP3630S	1500	5000
FP10000	FP3630S	1500	10000

Table 3.1: The different polymer solutions that were used in this research in which the polymer type and concentration were kept constant and only the salinity was varied.

The procedure to prepare these polymer solutions was as follows:

1. Calculate the required amounts of make-up water, salt, oxygen scavenger (sodium bisulphate, $NaHSO_3$), polymer and ITW.
2. Prepare the make-up water and filter over a 0.45 μ Millipore filter.
3. Weigh the correct amount of filtered make-up water into a glass bottle.
4. Add the salt and oxygen scavenger and stir until dissolved.
5. Add ITW protective package (a loading of 20% is usually adequate). ITW is a mixture of Isopropanol (15 wt%), Thiourea (7.5 wt%) and water (77.5 wt%) that protects the polymer from chemical degradation through free radical attack, especially when the fluid contains dissolved oxygen and traces of iron. A

20% ITW loading means that the total amount of Isopropanol added is equivalent to 20% of the total weight of polymer added to the solution.

6. Place the glass beaker onto a magnetic stirrer, insert a magnetic stirrer bar and create a deep water vortex.
7. Weigh out the correct amount of the dry polymer powder.
8. Sprinkle the polymer gently on the side of the water vortex, ensuring that no agglomerates ("fish eyes") are formed. If any agglomerates do form, discard the contents of the beaker and start again (the polymer should be added within 20 to 30 seconds; if it is added too fast lumps will form and if it is added too slow the solution will get too viscous for the last amount of polymer to go into solution).
9. Stir at full vortex for 5 minutes until the polymer is well-dispersed.
10. Close the bottle (to minimize oxygen dissolution) and reduce the stirrer speed to a level at which the surface of the liquid is just moving. Stir at this speed for a further 24-48 hours.
11. After stirring, filter the polymer solution through a $5\mu m$ filter.

3.2. RHEOMETRIC DEVICES

Two kinds of rheometers were used: A shear rheometer and an extension rheometer. Their working principals are explained in this section.

3.2.1. SHEAR RHEOMETER

The shear viscosity of fluid samples was measured with an Anton Paar MCR 302 using the concentric cylinder geometry. The temperature can be kept constant. Shear viscosities were measured over a range of 0.1 to 1000 s^{-1}. For the concentric geometry, Couette flow holds [13]:

$$\mu = \frac{T(b^2 - a^2)}{4\pi\Omega a b^2 L} \tag{3.1}$$

in which T is the measured torque, a and b are the radii of the inner and outer cylinders respectively (Figure 3.1) and Ω the angular frequency.

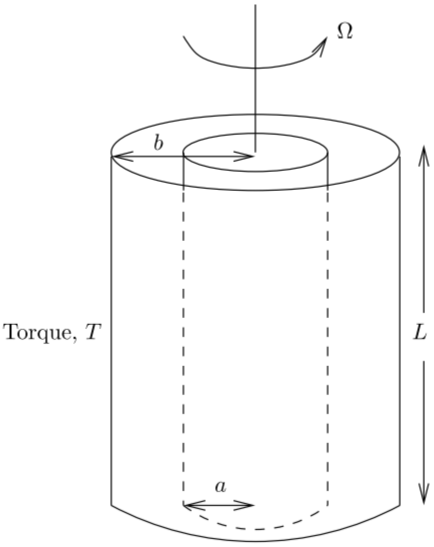

Figure 3.1: Schematic representation of the concentric cylinder rheometer.

3.2.2. E-VROC: EXTENSIONAL VISCOSITY MEASUREMENTS

To measure the extensional viscosity of fluid samples the e-VROC, a commercial device by Rheosense, was used. The e-VROC chip is engineered with a microfluidic channel of uniform width and depth. It has a hyperbolic contraction/expansion zone in the middle of the channel and four pressure sensors (Figure 3.2). When a liquid enters, it first experiences shear flow in the straight channel and then experiences an uniform planar extension in the contraction zone. This extension of the liquid causes an extra pressure drop next to the pressure drop attributed to shear. This section will follow the work published by Ober et al. [29]. An alternative analytical derivation of Newtonian flow through the contraction geometry is discussed in the next subsection that seems to provide a good alternative with respect to the interpretation of the experimental results [30].

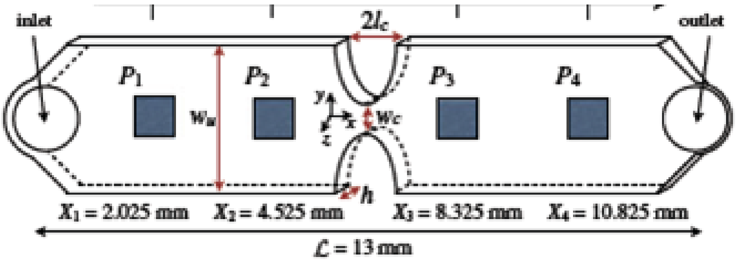

Figure 3.2: Schematic representation of the hyperbolic contraction within the e-VROC. The contraction dimensions are $h = 200\mu m$, $l_c = 400\mu m$, $w_c = 400\mu m$ and $w_u = 2920\mu m$.

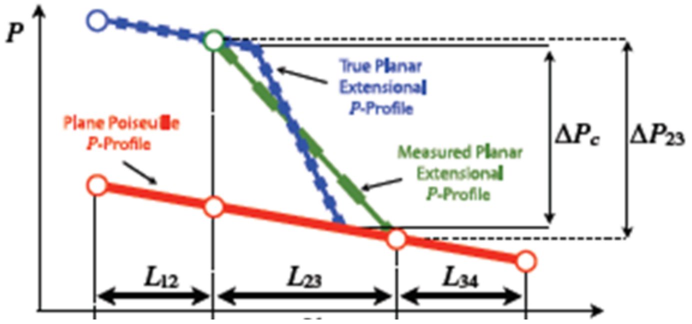

Figure 3.3: A schematic representation of a typical pressure profile over the hyperbolic planar contraction.L_{12}, L_{23} and L_{34} indicate the distance between the four pressure sensors.

The geometry of the contraction shown in Figure 3.2 can be described by:

$$w(x) = \frac{K}{x_0 + x} \tag{3.2}$$

where $w(x)$ is the width of the contraction as function of x for $0 \leqslant x \leqslant l_c$, $x_0 = l_c w_c/(w_u - w_c)$ and $K = x_0 w_u$. Neglecting shear flow contributions, a flow rate Q results in an extention rate through the contraction given by:

$$\varepsilon_a = \frac{Q}{l_c h}(\frac{1}{w_c} - \frac{1}{w_u}) \tag{3.3}$$

where w_u the width of the channel, w_c the width of the contraction, Q the flow rate, l_c the length of the contraction and h the height of the channel and contraction. The true strain or Hencky strain experienced by the fluid is maximum at the throat of the contraction and defined as:

$$\varepsilon_H = \int_0^t \varepsilon_a \, \mathrm{d}t = \ln \frac{w_u}{w_c} \tag{3.4}$$

A schematic representation of a typical pressure profile over the hyperbolic planar contraction is given in Figure 3.3. Because the pressure sensors are located outside the contraction area, the measured extensional pressure drop is bigger than the true pressure drop over the contraction. The true total pressure drop over the contraction is given by [29]:

$$\Delta P_c = \Delta_{23}\left\{1 - \frac{1}{2}(\frac{1}{P} - 1)\frac{L_{23} - 2l_c}{L}\right\} \tag{3.5}$$

in which ΔP_{23} is the pressure drop between sensors 2 and 3, $P \equiv \frac{\Delta P_{23}}{\Delta P_{14}}$, L_{23} the distance between sensors 2 and 3. If assumed that the flow through the constriction is an extension dominated mixed flow, the pressure drop over the contraction has both an elongational ΔP_e and shear ΔP_{vis} component and can be decomposed as:

$$\Delta P_c = \Delta P_e + \Delta P_{vis} \tag{3.6}$$

The pressure drop over the contraction due to shear flow can be written as [29]:

$$\Delta P_{vis} = \frac{2^{n+2}}{n+1}(\frac{2n+1}{n})^n(\frac{l_c}{h})^{n+1}\left\{(\frac{w_u}{w_u - w_c})^{n+1} - (\frac{w_c}{w_u - w_c})^{n+1}\right\}\eta\varepsilon_a = Km\varepsilon \tag{3.7}$$

where n is the power law index. For a Newtonian fluid $(n = m = 1)$ Equation 3.7 reduces to:

$$\Delta P_{vis} = 12(\frac{l_c}{h})^2\left\{\frac{w_u + w_c}{w_u - w_c}\right\}\eta\varepsilon_a \tag{3.8}$$

The associated apparent extensional viscosity can be calculated by Equation 3.9:

$$\eta_{E,a} = \frac{\Delta P_e}{\varepsilon_H \varepsilon_a} \tag{3.9}$$

in which ΔP_e the pressure drop due to fluid extension over the contraction, ε_H the Hencky (true) strain and ε_a the extensional rate respectively.

Equations 3.3 to 3.9 can only be applied when the flow is not dominated by inertia forces compared to viscous forces, so when:

$$Re_c = \frac{\rho d_h U}{\eta_0} = \frac{\rho d_h l_c \varepsilon_a}{\eta_0} < 20 \tag{3.10}$$

in which Re_c is the crtical Reynolds number, ρ the density of the fluid and d_h the hydraulic diameter of the contraction which is defined as $\frac{2hw_c}{h+w_c}$. When Re > 20 inertia forces become dominant however flow is fully laminar if $Re < 10$ [29].

Furthermore, the dimensionless Trouton number, Tr, is often used to compare extensional and shear viscosities:

$$Tr = \frac{\text{Extensional viscosity}}{\text{Shear viscosity}} \tag{3.11}$$

For an incompressible Newtonian fluid under ideal fully-developed planer extension, the Trouton number equals 4.

Before each test, the e-VROC cell was flushed with a sufficient amount of the test sample such that no air bubbles remained in the contraction geometry. Hereafter, the pressure field was allowed to equilibrate by allowing the test sample to rest for 20 minutes. After this the baseline pressure was measured the test was started. The measuring duration of each flow rate was such that the pressure profile attained a steady state value. The full experimental procedure can be found in Appendix A.

ANALYTICAL DERIVATION OF NEWTONIAN FLOW IN THE E-VROC CELL

In this section the theoretical pressure drop contributed to shear and extension over the contraction-expansion area of the e-VROC cell for a Newtonian fluid are given. The full derivation can be found in Appendix B and was provided by Paddington and De of Eindhoven University of Technology [30] . In the derivation the friction with the side walls is neglected, however the friction with the top and bottom is included. Furthermore, the expansion-contraction geometry is designed such that 'pure' elongational flow can be assumed along the center plane.

$$\Delta P_c^E = \eta Q \frac{1}{l_c h w_u} \left[\frac{48}{5} \left(\frac{w_u}{w_c} - 1 \right) ln \left(\frac{w_u}{w_c} \right) \right] \tag{3.12}$$

$$\Delta P_c^S = \eta Q \frac{1}{l_c h w_u} \left[\frac{4}{3} \left(\frac{l_c}{h} \right)^2 \left(\frac{w_u}{w_c} + 1 \right) + \left(\frac{w_u}{w_c} - 1 \right) \left(\frac{w_u}{h} \right)^2 \left(1 - \left(\frac{w_c}{w_u} \right)^2 \right) \right] \tag{3.13}$$

From these equations it can be concluded that for a Newtonian fluid the pressure drop is dominated by shear flow, when Poiseuille flow in the z-direction is assumed. Therefore, the flow through the contraction-expansion geometry is not dominated by extensional forces as assumed in the derivation of Equation 3.9 but by shear forces. The above equations will be used in Section 4.1.4 to show that they match with the experiments.

WHY MICROFLUIDICS?

In this thesis a microfluidic device is used to characterize the resistance to elongation of polymer solutions. Microfluidics is the science of systems that use small amounts of fluids (10^{-9} to 10^{-8} litres), using channels with dimensions of tens to hundreds of micrometers [31]. As a technology, microfluidics takes advantage of fundamental differences between fluid flow is large channels and fluid flow in microfluidic channels. The main advantage is the ability to measure low viscosity elastic fluids at high deformation rates while maintaining laminar flow. Therefore, large viscoelastic effects can be achieved, making microfluidics an excellent technology to study extension rheometry. If hyperbolic contractions are used in combination with microchannels a nearly constant extension rate is induced at the center line of the geometry, allowing accurate determination of the apparent extensional viscosity [32]. Besides the ability to measure at high deformation rates, microfluidic devices also reduce the effects of viscous heating, characterized by the Nahme number:

$$Na = \frac{\eta \beta \gamma^2 d^2}{kT} \tag{3.14}$$

where β is the thermal sensitivity $\frac{\partial(\log\eta)}{\partial(\log T)}$, k the thermal conductivity and T the temperature. Viscous heating can be neglected when $Na \ll 1$, since $Na \propto d^2$ microfluidic devices enable to measure at constant temperature at high deformation rates [33]. Furthermore, the small fluid samples and device dimensions induce quick measurements.

Due to the small dimensions of microfluidic devices, the flow is generally dominated by viscous forces compared to inertia forces. The relative magnitude of both forces is called the Reynolds number:

$$Re = -\frac{\rho v D}{\eta} \tag{3.15}$$

where vD is a characteristic velocity of the flow. Low Reynolds numbers represent laminar flow, at higher Reynolds numbers inertia forces become dominant and extra friction is introduced by flow turbulence. When flow is laminar it is possible to accurately compute the flow.

Fluid interface formation of complex liquids are governed by capillary and body forces. Generally, capillary forces (σ) dominate the body forces in a microfluidic device, resulting in a Bond number much smaller than one:

$$Bo = -\frac{\rho d^2 g}{\sigma} \tag{3.16}$$

Because of the large capillary forces air bubbles can have a tremendous effect on the measurements. Since polymer solution are viscoelastic and due to relative absence of of inertia, viscoelastic forces may be important [33]. Three important dimensionless groups that describe these elastic effects are the Weissenberg, Deborah and Elasticity number. The strength of the shear rate (γ) can be defined by the Weissenberg number:

$$Wi = -\gamma\tau_r \tag{3.17}$$

where τ_r is the relaxation time of the fluid. The Deborah number is defined as the ratio of the time it takes for a material to adjust to an applied stress and the characteristic time scale of an experiment:

$$De = \frac{\tau_r}{\tau_E} \tag{3.18}$$

where τ_E the average residence time. If $De \ll 1$ the flow is purely viscous since the fluid relaxes relatively quick, if however $De \gg 1$ the fluid does not relax and the time scale of the experiment and the subsequent flow is elastic. While the Deborah and Weissenberg number are similar and often the same, they have different physical interpretations. The Deborah number described the rate at which elastic energy is stored or released and therefore accounts for flows with a non-constant stretch history. Oppositely, the Weissenberg number describes a flow with constant deformation history and therefore indicates the anisotropy generated by the deformation.

All the dimensionless groups mentioned above, are functions of flow rate. The Elasticity number (El) is independent of flow rate and therefore only dependent on the fluid properties and flow geometry.

$$El = \frac{De}{Re} = \frac{\lambda\eta}{\rho d^2} \tag{3.19}$$

From Equation 3.19 it is evident that elastic effects are amplified in microfluidic geometries.

4

EXPERIMENTAL RESULTS

4.1. CALIBRATION: NEWTONIAN FLUIDS

Although the e-VROC has already been used and tested in previous studies [29, 34, 35], this study verified the shear and extensional viscosity of multiple Newtonian calibration fluids with a viscosity range of 15-100cP (Table 4.1). The shear rheometer measurements of these fluids can be found in Appendix D. From the plots it can be concluded that the fluids behave Newtonian since their viscosity is independent of shear rate. The average rheometer values are stated in Table 4.1.

Fluid Name	**Fluid Type**	**Shear Viscosity** [**mPas**]	**Density** [**kg/m^3**]	**Temperature** [**C**]
N15	$32-68w\%\ H_2O-$Glycerol	15.8	1175	25
N25	Fluid 25	26	800	60
N50	Fluid 50	49.1	960	25
N75	Olive Oil	71.6	910	23
N100	Fluid 100	97	960	25

Table 4.1: The different Newtonian fluids that were used for the calibration of the e-VROC cells.

4.1.1. PRESSURE-TIME RESPONSE

The pressure-rate relationship was examined for each fluid. Newtonian fluids show a linear dependence of pressure as function of flow rate. To ensure the quality of the measurements, the flow should be steady state. Figure 4.1 shows pressure response over time for N50. After an initial ramp after start of injection the pressure response over time is stable after about three seconds. Still some noise is observed however the magnitude of this noise is within the accuracy of the pressure transducers.

4.1.2. PRESSURE-FLOW RATE BEHAVIOUR

Figure 4.2 shows the measured pressure data within the e-VROC for N50. The same plots for the N25 to N100 can be found in Appendix D. Figure 4.3 shows a linear dependency of the pressure gradients to flow rate for N50, both before and after the contraction. It can also be concluded that the gradient before and after the contraction are the same. This is what you would expect since the dimensions before and after the contraction are the same. The same behaviour is observed for the other calibration fluids (Appendix D). Furthermore, a linear dependency over the contraction is observed. From this it is concluded that the Newtonian calibration fluids indeed show Newtonian behaviour.

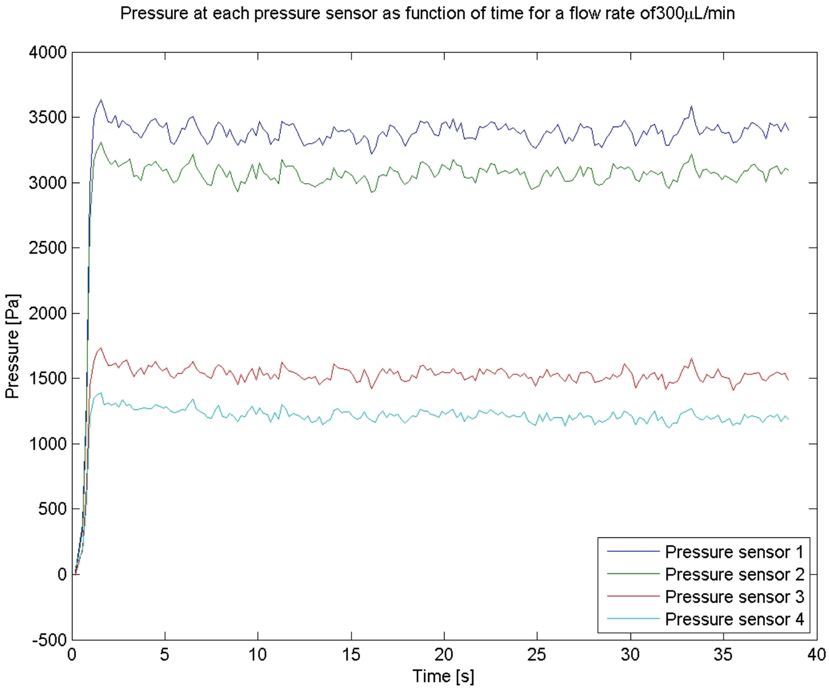

Figure 4.1: Pressure at each pressure sensor as function of time for a flow rate of 299.9$\mu L/min$ for N50.

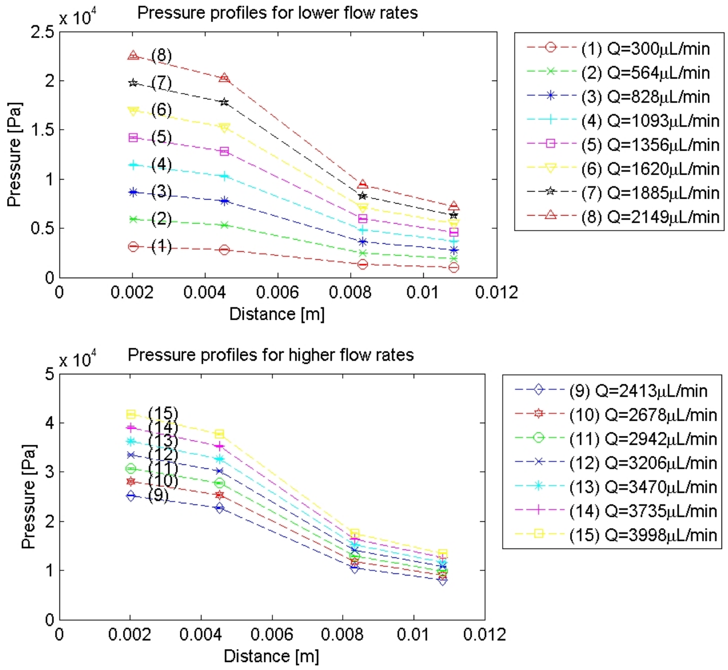

Figure 4.2: Measured pressures within the e-VROC cell for N50 for different flow rates.

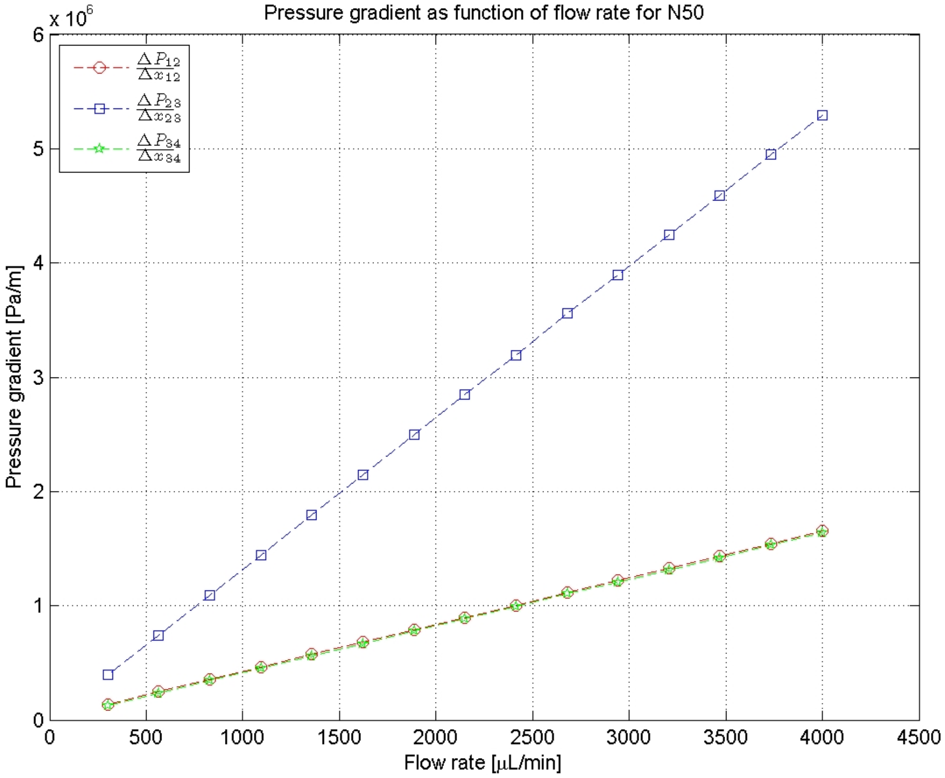

Figure 4.3: Pressure gradients as function of flow rate for N50.

4.1.3. VISCOSITY DETERMINATION

Now that Newtonian flow has been verified, the shear viscosity can be determined from the e-VROC data. Since $\frac{w_u}{h} \gg 1$ the shear viscosity for laminar Newtonian flow in the microfluidic slit channel is given by [33]:

$$\eta_{sh} = \frac{wh^3 \Delta P}{12LQ(1+\frac{h}{w})} \tag{4.1}$$

The shear viscosities at different flow rates calculated from the e-VROC pressure data are shown in Table 4.2 for N50. Although overestimating the shear viscosity, the calculated values are in good agreement with the viscosity determined by the rheometer, within 10% of the rheometer value (50cP). At low flow rates the calculated shear viscosities are more erroneous, this is likely due to the fact that the pressure traducers have higher accuracy at higher pressure e.g at higher flow rates.

Flow rate (μL/min)	**μ_{sh12} (cP)**	**μ_{sh34} (cP)**
300	55.5	52.2
564	54.7	51.9
828	53.7	52.3
1093	53.4	52.0
1356	53.2	52.0
1620	53.0	51.9
1885	52.6	51.8
2149	52.3	51.9
2413	52.0	51.7
2678	52.3	51.9
2942	52.1	51.6
3206	52.2	51.5
3470	52.1	51.5
3735	51.9	51.6
3998	52.1	51.5

Table 4.2: Shear viscosities determined from the e-VROC data for N50.

To see whether Equation 3.9 determines the extensional viscosity of a fluid or an apparent extensional viscosity, the corresponding Trouton ratio (Equation 3.11) is compared to the theoretical Trouton ratio for planar extension ($Tr = 4$). The calculated extensional viscosities (Equation 3.9) for N50 at different rates are shown in Table 4.3. Also the corresponding Trouton ratio and the Reynolds number is shown. From Table 4.3 is concluded that the apparent extensional viscosity of N50 is around 77. Almost a factor of 20 higher than the theoretical value. The Reynolds number (Equation 3.10) for all flow rates is below 20. Consequently, the high Trouton ratio is not due to an extra pressure drop resulting from turbulent effects. Therefore, it should be noted that the e-VROC device apears to be more of an extension viscosity indexer rather than an extensional rheometer [36] because it gives an indication of the extensional behaviour of a fluid but is unable to quantify the exact value.

According to [29] Trouton ratios around 70 are to be expected for Newtonian fluids measured in the e-VROC and the high apparent extensional viscosity can be attributed to two factors. Firstly, the abruptness of the contraction causes the flow divergence far upstream of the contraction (Section 5.2.1). They even reported flow divergence at three contraction lengths upstream of the contraction. Secondly, the corners of the microfluidic cell are not idealized sharp corners but are rounded such that the cross-sectional area of the contraction is 10-20% smaller than the designed cross-sectional area. These two factors result in discrepancies between measured and anticipated kinematics, therefore the actual apparent extensional viscosity is higher than its expected value [29]. However, these factors do not account for the entire discrepancy. The main reason is that the dissipation due to shear in the contraction is significant and the generated flow cannot be seen as an extension dominated flow as will be shown in Section 3.2.2.

Flow rate (μL/min)	η_e(cP)	Tr (-)	Re (-)
300	3771	74	1.3
564	3775	75	2.4
828	3798	76	3.5
1093	3813	77	4.6
1356	3829	77	5.7
1620	3846	78	6.7
1885	3844	78	7.9
2149	3851	78	9.0
2413	3847	79	10.1
2678	3865	79	11.2
2942	3848	79	12.3
3206	3849	79	13.4
3470	3850	79	14.5
3735	3855	79	15.6
3998	3852	79	16.7

Table 4.3: The extensional viscosities, the corresponding Trouton ratio and Reynolds number for N50 at the measured flow rates.

4.1.4. COMPARISON OF EXPERIMENTAL DATA TO ANALYTICAL SOLUTION

Figure 4.4 shows the comparison of the analytical prediction and the experimental pressure profile for N50. The analytical expressions of Equations 3.12 and 3.13 are able to predict the pressure drop over the contraction-expansion geometry within 2% for N50. From this it can be concluded that the experiments can be matched with the theory within experimental accuracy. Together with Equation 4.1 the measured pressure profiles can be reconstructed as shown in Figure 4.4.

$$\Delta P_c^E = \eta Q \frac{1}{l_c h w_u}\left[\frac{48}{5}\left(\frac{w_u}{w_c}-1\right) ln\left(\frac{w_u}{w_c}\right)\right] \qquad (3.12)$$

$$\Delta P_c^S = \eta Q \frac{1}{l_c h w_u}\left[\frac{4}{3}\left(\frac{l_c}{h}\right)^2\left(\frac{w_u}{w_c}+1\right)+\left(\frac{w_u}{w_c}-1\right)\left(\frac{w_u}{h}\right)^2\left(1-\left(\frac{w_c}{w_u}\right)^2\right)\right] \qquad (3.13)$$

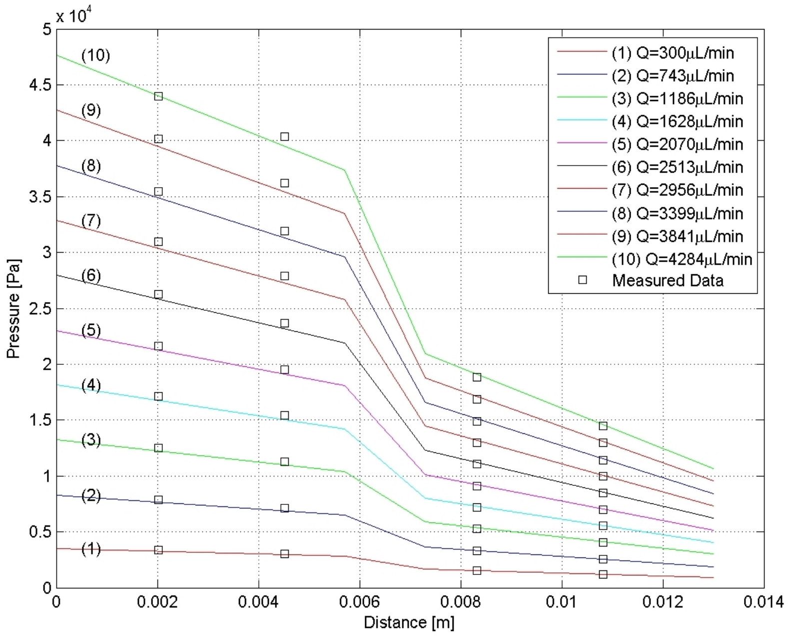

Figure 4.4: Comparison of analytical prediction and the experimental pressure profile for N50.

4.2. POLYMER SOLUTIONS

After the initial calibration of the e-VROC with different Newtonian fluids, the behaviour of three polymer solutions (FP3630S) with different salinities was studied (Table 3.1). First, the time-pressure signal was analysed at different flow rates to determine when the flow can be considered as stable. Hereafter, the pressure-profiles as function of flow rate were examined to investigate the extensional behaviour of these polymer solutions. Furthermore, the reproducibility of the experimental results is discussed and finally the effect of salinity on the extensional behaviour of FP3630S is addressed. Note that the number in the name of the polymer solutions indicates the NaCl concentration. The shear rheometer results of the three solutions can be found in Appendix C.

Name Solutions	Polymer Type	Polymer Concentration [ppm]	NaCl concentration [ppm]
FP2500	FP3630S	1500	2500
FP5000	FP3630S	1500	5000
FP10000	FP3630S	1500	10000

Table 4.4: The different polymer solutions that were used in this research in which the polymer type and concentration were kept constant and only the salinity was varied. Note that the number in the name of the polymer solutions indicates the NaCl concentration.

4.2.1. PRESSURE-TIME RESPONSE

To study the pressure response over time, FP5000 was flown through the e-VROC cell at 4 different flow rates for times varying between 15 and 30 minutes. The resulting pressure measurements are shown in Figure 4.5. The pressure ramps up for about 10 seconds, a bit longer than with the Newtonian fluids. However, at lower rates the start-up time can increase to around one minute. Furthermore, the pressure time response signals of pressure transducers 1 and 2 and transducer 3 and 4 correlate reasonably well. However, there is no correlation between the pressure transducers before and after the contraction geometry.

Unlike Newtonian fluids, the noise content of the time signals, about 400-500Pa, is above the error margin of the individual pressure transducers. Fourier analysis was done to examine the frequency content of the time signals. The noise seemed to be random (Appendix E). However, since the measured pressures are being sampled at 5Hz, it very difficult to detect any noise above 5Hz. The high noise content may be attributed to set-up and/or fluid driven features, such as:

1. Set-up
   - (a) **Stick-slip:** When two objects (e.g. plunger and barrel) slide past one-another, stick-slip motion might occur due to the friction it generates. The plunger is therefore not moving continuously but more as a discrete signal, the fluid will (although brief) stop flowing. After which, it will quickly start flowing again. Since polymer solutions have a shear dependent viscosity, these short changes in flow rate will therefore alter the viscosity of the solution. These possible changes in viscosity might explain the irregularity of the pressure-time response.
2. Fluid
   - (a) **Elasticity of polymer solutions:** Since polymer solutions have a memory with respect to deformation, the high noise content may also be explained by the fact that not all polymer molecules are in the same (relaxed) state and therefore behave differently upon extensional deformation. The residence time of the polymer in the e-VROC is between 4.8 seconds and 1.2 seconds for flow rate between 105 $\mu L/min$ and 630 $\mu L/min$. The relaxation time of a polymer solution is dependent on polymer type, salinity and polymer concentration. The residence time in contraction-expansion area is 160 and 20 milliseconds respectively. The relaxation time for HPAM3630 at a concentration of 1500ppm is around 0.1 to 1 second. This indicates that polymer molecules are still recovering from the deformation in the contraction-expansion area while they pass by third and fourth pressure sensors. From this it can be concluded that the polymer solutions show elastic deformation ($De > 1$).

     Appendix F shows the time signal response of Laponite, a non-elastic highly shear thinning artificial clay. Although, the noise content is slightly higher compared to Newtonian fluids, the noise is still within the measurement precision of the pressure transducers. Indicating that elasticity probably causes the high noise content while measuring polymer solutions.

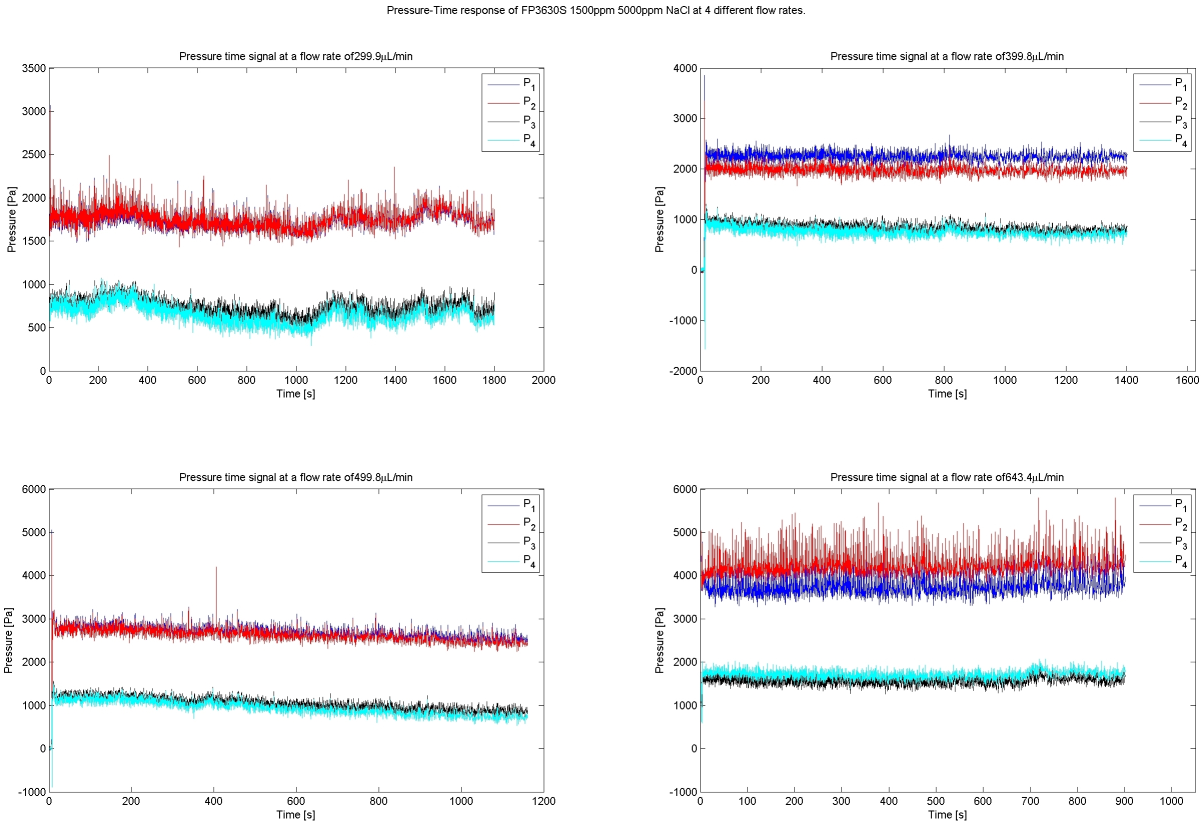

Figure 4.5: The pressure response over time of FP5000 at 4 different flow rate.

Besides the high noise content, also trends in the recorded pressure can be observed. Table 4.5 shows the corresponding trends in the measured pressure for each pressure transducer at the 4 different flow rates. Although the observed trends are generally very subtle, the trend at a flow rate of 500 $\mu L/min$ is quite perceptible. Since the trends before and after the contraction for a flow rate of 400 $\mu L/min$ are of opposite sign, also a noticeable trend in the pressure drop between transducers 2 and 3 is observed. The trends may be explained by the elasticity of the polymer, literally pulling the fluid through the microfluidic device. As a consequence the boundary condition at the outlet is not constant and causes the trend in the pressure data.

	Pressure trend [Pa/s]			
Flow Rate (μL/min)	**Pressure Sensor 1**	**Pressure Sensor 2**	**Pressure Sensor 3**	**Pressure Sensor 4**
300	-0.021	-0.028	-0.081	-0.12
400	0.10	0.072	-0.06	-0.068
500	-0.15	-0.19	-0.30	-0.38
643	0.12	0.19	0.027	0.041

Table 4.5: Observed time trends in the measured pressures for each pressure transducer at 4 different flow rates.

Hereafter only the pressure drops will be investigated rather than the individual pressures, since the shear and extensional effects can be qualified by the amount of pressure drop over the different sections of the e-VROC cell. In Figure 4.6 the moving average of the measured pressure differences is presented for 4 different flow rates. The moving average was determined over a window of 20 seconds. The figure reveals that although the time-pressure signal has a high noise content, on average the pressure is roughly constant. From the graph it can be concluded that the moving average is stable after 20-40 seconds. Although it can be argued that the moving average at a flow rate of 643$\mu L/min$ is not stable until 200 seconds. Therefore it was decided to measure for 200 seconds at each flow rate in future experiments, to ensure 'stability' of the time-pressure signal. Another thing that can be observed in Figure 4.6 is that the measured pressure differences between sensors 1 and 2 and sensors 3 and 4 for all flow rates is around 50-100Pa. This is of the same magnitude as the measurement precision of the MEMS pressure tranducers. Therefore the measured pressure drop between these sensors cannot be considered reliable and no shear viscosities can be determined for the polymer solutions.

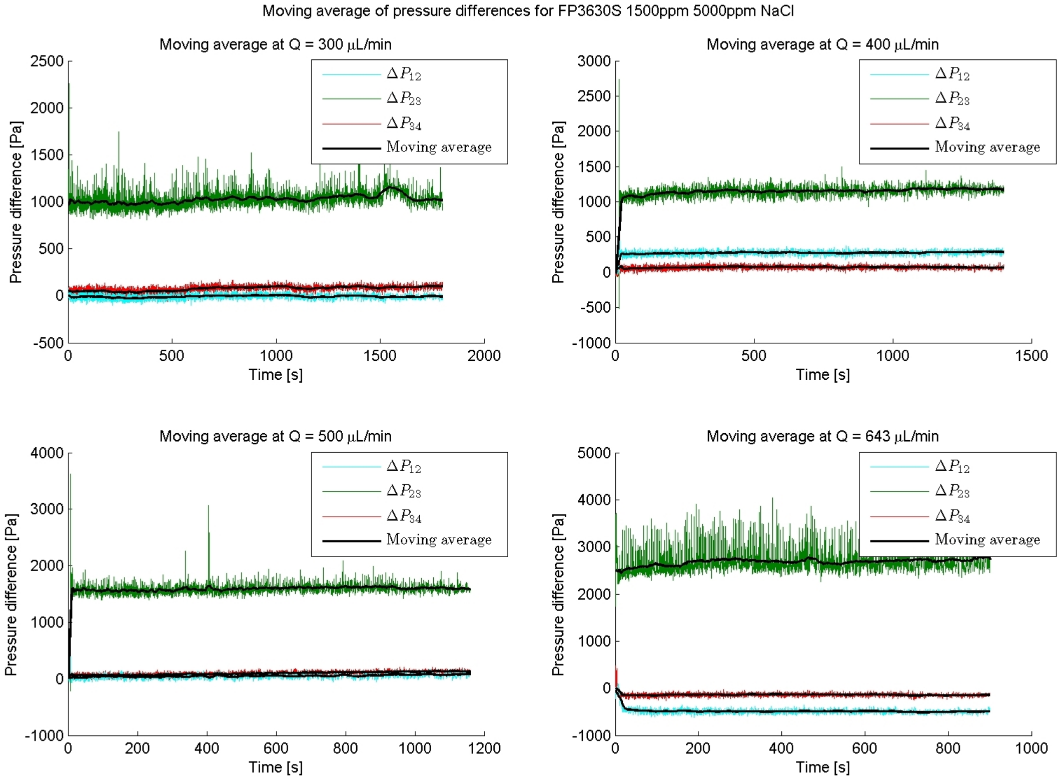

Figure 4.6: The moving average over 20 seconds of the measured pressure differences over time at 4 flow rates for FP5000.

4.2.2. PRESSURE-FLOW RATE BEHAVIOUR

Figures 4.7, 4.8 and4.9 show the pressure profiles at different flow rates for FP2500, FP5000 and FP10000 respectively. From all these graphs it is evident that most of the pressure dissipation (>90%) occurs between pressure sensor 2 and 3. Since the shear rate in the contraction is very high, the pressure dissipation due to shear is negligible because of the shear-thinning behaviour of the polymer solutions. From this it can be concluded that for the polymer solutions most of the pressure drop in the e-VROC cell can be attributed to extensional flow. Furthermore, some profiles seem to be 'unphysical' since the ΔP_{12} and ΔP_{34} are negative, resulting in an upward slope along the flow direction. However, as indicated before, the pressure drop between these sensors is so small that it is of the same magnitude as the sensitivity of the individual pressure transducers. Also the absolute standard deviation of the measured pressures increases with increasing flow rate. But when compared to the mean value, its relative value is more or less constant with flow rate (around 5%).

Figure 4.10 shows the pressure gradients between the pressure sensors as function of flow rate for the three polymer solutions. For all polymer solutions it is observed that the pressure gradients between sensors 1 and 2 and sensors 3 and 4 are small and not necessarily monotonically decreasing with rate. This again can be contributed to the fact that the pressure difference between these sensors is within the error margin of the sensors. It is also observed that the pressure gradient between sensors 2 and 3 is increasing non-linearly with flow rate. Therefore, it can be concluded that all these polymer solutions show strain-thickening behaviour, since the main pressure drop is due to elongation.

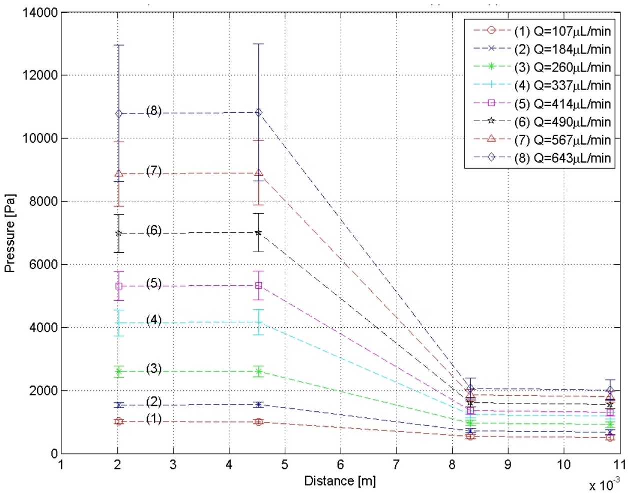

Figure 4.7: Measured pressure in the e-VROC cell for FP2500 at different flow rates. The pressure values and their error bars are based on the measured pressure over time, respectively the mean and standard deviation.

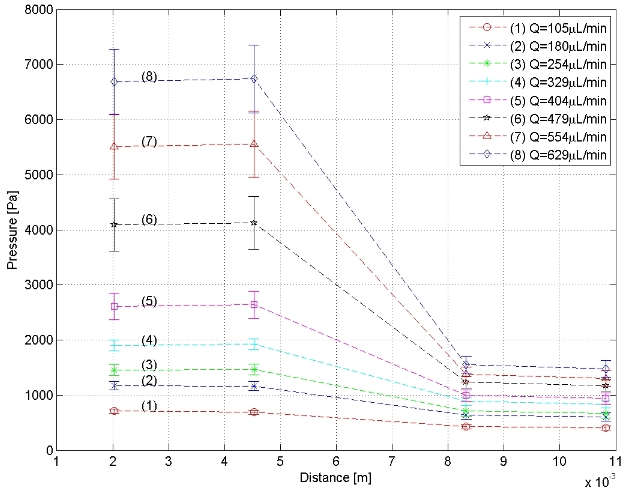

Figure 4.8: Measured pressure in the e-VROC cell for FP5000 at different flow rates. The pressure values and their error bars are based on the measured pressure over time, respectively the mean and standard deviation.

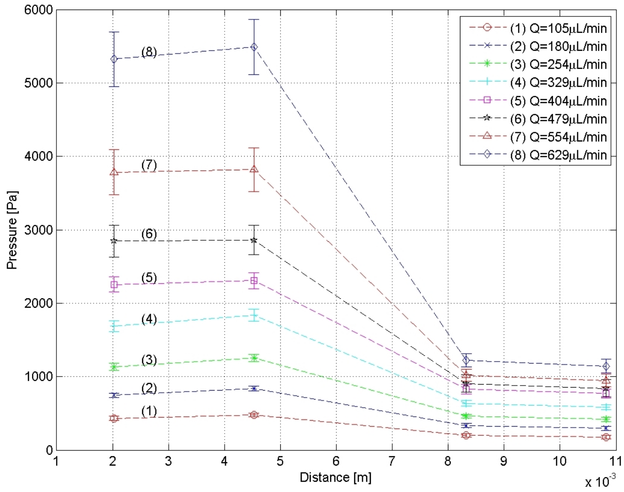

Figure 4.9: Measured pressure in the e-VROC cell for FP10000 at different flow rates. The pressure values and their error bars are based on the measured pressure over time, respectively the mean and standard deviation.

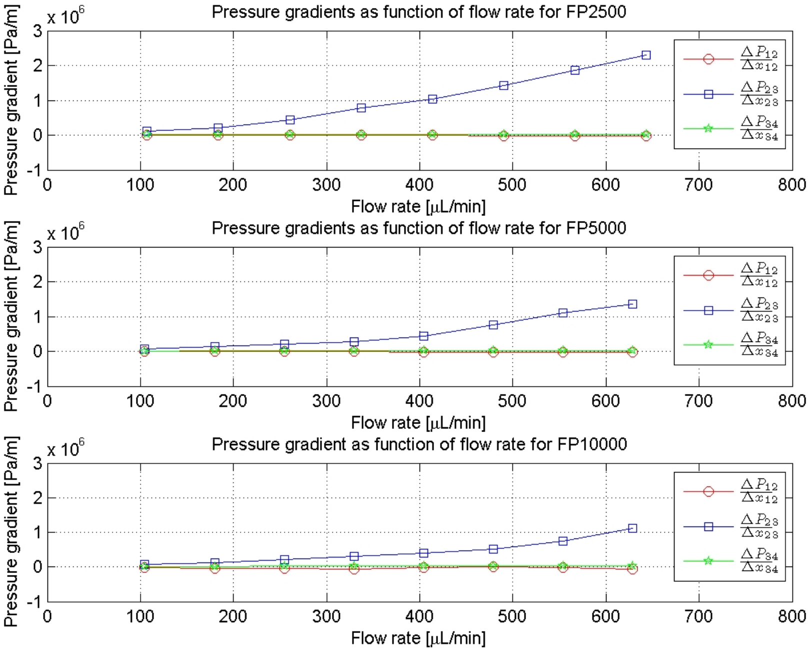

Figure 4.10: The pressure gradient between the pressure sensors as function of flow rate for the three polymer solutions.

4.2.3. REPRODUCIBILITY

For all the three polymer solutions the flow experiments were repeated twice to access the reproducibility of the results. Tables 4.6,4.7 and 4.8 show the mean value and standard deviation of the measured pressure gradients for FP2500,FP5000 and FP10000 respectively. Note that the number in the name of the solution indicate the amount of salt. Also the relative value of standard deviation and the mean is presented. The provided tables show that the pressure gradients between the pressure sensor 1 and 2 and sensors 3 and 4 are far from reproducible, because of the pressure sensitivity limit of the transducers. Also the reproducibility of the pressure gradients between sensors 2 and 3 is not obvious with relative errors ranging from 5 to 30%. Whereas, the reproducibility of the shear rheometer results is very good (Appendix C). Solution FP2500 shows quite good reproducibility, with a relative error of 5% on average. Although not enough data is available to back up the statement, it can be argued that the reproducibility is better with increasing flow rate.

	Mean value of experiments [Pa/m]			**Standard deviation of experiments [Pa/m]**			**Relative ratio [%]**		
Flow rate [$\mu L/min$]	$\frac{\Delta P_{12}}{x_{12}}$	$\frac{\Delta P_{23}}{x_{23}}$	$\frac{\Delta P_{34}}{x_{34}}$	$\frac{\Delta P_{12}}{x_{12}}$	$\frac{\Delta P_{23}}{x_{23}}$	$\frac{\Delta P_{34}}{x_{34}}$	$\frac{\Delta P_{12}}{x_{12}}$	$\frac{\Delta P_{23}}{x_{23}}$	$\frac{\Delta P_{34}}{x_{34}}$
107.3	1.98E+04	1.42E+05	1.96E+04	3.49E+04	1.63E+04	1.05E+04	176.1	11.5	53.6
183.8	5.97E+04	2.14E+05	2.36E+04	1.11E+05	1.06E+04	9.08E+03	186.7	5.0	38.4
260.4	-7.00E+03	4.34E+05	2.24E+04	2.32E+03	1.70E+04	7.82E+03	-33.1	3.9	35.0
337	-1.29E+04	8.33E+05	2.33E+04	4.23E+03	5.83E+04	1.06E+04	-32.8	7.0	45.4
413.7	-6.84E+03	1.12E+06	3.25E+04	3.91E+03	6.57E+04	1.51E+04	-57.2	5.9	46.5
490.3	-1.20E+04	1.44E+06	3.01E+04	2.39E+03	5.15E+04	1.16E+04	-19.9	3.6	38.6
566.9	-1.29E+04	1.85E+06	3.15E+04	4.06E+03	3.32E+04	1.38E+04	-31.4	1.8	44.0
643.4	-1.50E+04	2.28E+06	3.30E+04	3.93E+03	3.17E+04	1.61E+04	-26.3	1.4	48.7

Table 4.6: Data of multiple experiments using FP2500.

	Mean value of experiments [Pa/m]			**Standard deviation of experiments [Pa/m]**			**Relative ratio [%]**		
Flow rate [$\mu L/min$]	$\frac{\Delta P_{12}}{x_{12}}$	$\frac{\Delta P_{23}}{x_{23}}$	$\frac{\Delta P_{34}}{x_{34}}$	$\frac{\Delta P_{12}}{x_{12}}$	$\frac{\Delta P_{23}}{x_{23}}$	$\frac{\Delta P_{34}}{x_{34}}$	$\frac{\Delta P_{12}}{x_{12}}$	$\frac{\Delta P_{23}}{x_{23}}$	$\frac{\Delta P_{34}}{x_{34}}$
104.8	6.90E+03	7.63E+04	-3.01E+04	2.76E+04	2.30E+04	6.66E+04	400.39	30.16	-221.04
179.6	2.74E+03	1.62E+05	-2.51E+04	2.37E+04	5.74E+04	6.63E+04	866.11	35.39	-263.75
254.4	-3.93E+03	2.58E+05	-2.11E+04	1.55E+04	8.57E+04	6.57E+04	-394.34	33.21	-311.15
329.3	-7.81E+03	4.43E+05	-1.71E+04	7.70E+03	1.67E+05	6.54E+04	-98.69	37.65	-381.63
404.2	-4.48E+03	6.31E+05	-1.35E+04	2.25E+04	1.74E+05	6.53E+04	-502.07	27.52	-484.18
479.1	-1.52E+04	9.46E+05	-1.00E+04	3.96E+04	1.75E+05	6.50E+04	-260.94	18.52	-648.72
553.9	5.03E+03	1.15E+06	-7.76E+03	2.84E+04	4.86E+04	6.45E+04	565.45	4.23	-831.12
628.7	1.49E+03	1.42E+06	-5.00E+03	3.95E+04	4.65E+04	6.37E+04	2655.46	3.28	-1273.84

Table 4.7: Data of multiple experiments using FP5000.

	Mean value of experiments [Pa/m]			**Standard deviation of experiments [Pa/m]**			**Relative ratio [%]**		
Flow rate [$\mu L/min$]	$\frac{\Delta P_{12}}{x_{12}}$	$\frac{\Delta P_{23}}{x_{23}}$	$\frac{\Delta P_{34}}{x_{34}}$	$\frac{\Delta P_{12}}{x_{12}}$	$\frac{\Delta P_{23}}{x_{23}}$	$\frac{\Delta P_{34}}{x_{34}}$	$\frac{\Delta P_{12}}{x_{12}}$	$\frac{\Delta P_{23}}{x_{23}}$	$\frac{\Delta P_{34}}{x_{34}}$
104.8	-3.05E+04	7.21E+04	2.27E+04	4.45E+04	2.47E+04	2.26E+04	-145.68	34.18	99.70
179.6	-3.75E+04	1.33E+05	2.74E+04	4.65E+04	2.81E+04	2.28E+04	-123.84	21.18	83.39
254.4	-4.53E+04	2.01E+05	3.02E+04	4.33E+04	2.25E+04	2.17E+04	-95.55	11.19	71.76
329.3	-4.11E+04	2.66E+05	3.36E+04	2.88E+04	4.14E+04	2.20E+04	-70.12	15.57	65.27
404.2	-1.29E+04	3.76E+05	3.63E+04	1.19E+04	4.96E+04	2.24E+04	-92.28	13.22	61.66
479.1	1.03E+04	5.52E+05	3.96E+04	4.05E+04	8.93E+04	2.37E+04	391.32	16.17	60.00
553.9	1.62E+04	7.06E+05	4.04E+04	6.20E+04	3.27E+04	2.11E+04	383.01	4.63	52.14
628.7	6.26E+03	9.45E+05	4.24E+04	9.08E+04	1.64E+05	2.07E+04	1450.60	17.34	48.74

Table 4.8: Data of multiple experiments using FP10000.

4.2.4. REPRODUCIBILITY AND ADSORPTION HYSTERESIS

To assess the reproducibility of the experimental results with respect to adsorption hysteresis, the following sequence of fluids was flown through a clean cell. First three flow experiments with N15 were performed. Hereafter the cell was cleaned with water, after which three flow experiments with a polymer solution were performed. The cell was cleaned again with water and three experiments with N15 were carried out ones more. Figure 4.11 shows the measured pressure gradients in the e-VROC cell as function of flow rate for the N15 for the described sequence. It shows that the experiments are reproducible. The normalized standard deviation of experimental results is below 10%. It can also be observed that the pressure gradients have increased by 8% on average after the cell has been contacted with polymer. This is likely due to polymer adsorption to the surface of the e-VROC cell, hereby increasing the flow resistance. If it is assumed that the adsorption is uniform over all edges of the e-VROC cell, then the pressure gradient increase corresponds to a 4.5 μm thick layer of adsorbed polymer. However, the adsorbed polymer layer will not form a smooth surface. Therefore the apparent roughness of the cell walls increases which also induces an extra resistance to flow. Furthermore, an irregularity is observed for one the N25 flow experiments. This may be due to an air bubble inside the fluid sample affecting the pressure measurements. Applying a polymer breaker (bleach) to provide additional evidence for the polymer adsorption on the cell wall was not done due to time constraints.

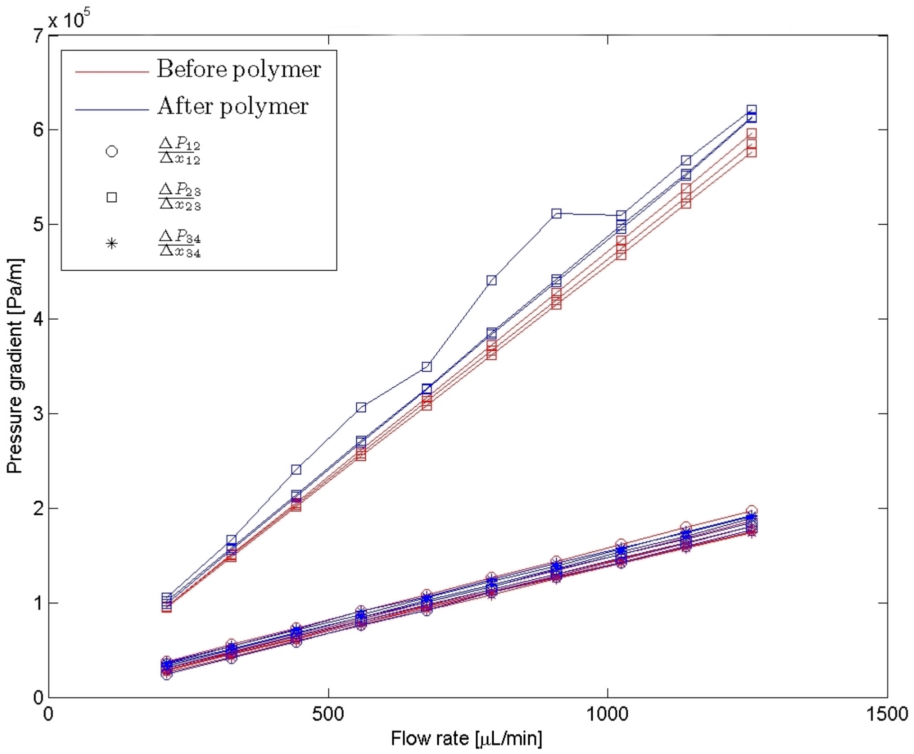

Figure 4.11: The measured pressure gradients in the e-VROC cell as function of rate for the N15 for the Glycerol-Polymer-Glycerol sequence.

4.2.5. SALINITY DEPENDENCE

The effect of salinity on the strain-thickening behaviour of FP3630S is show in Figure 4.12. An increase in salinity causes a decrease in the pressure gradient over the contraction-expansion geometry, hence the strain-thickening behaviour decreases. The conceptual model to explain this effect is as follows: As more salt is added to the solution more of the negative charges along the polymer chain are getting shielded by the Na^+ ions, causing it to shrink in size. This reduction in size reduces the flexibility of the polymer molecules, making them stiffer. Since the polymer molecules become stiffer, they are less likely to uncoil, making it easier to flow through a contraction-expansion geometry. This decrease in resistance is observed by a lower pressure drop. It can also be observed that the salinity effect is more pronounced at higher flow rates. This is in line with the conceptual model. At higher flow rates (extensional rates) the polymer has to uncoil further as it passed through a constriction. Since salt ions reduce the uncoiling of the polymer molecules, the effect is more pronounced at higher flow rates.

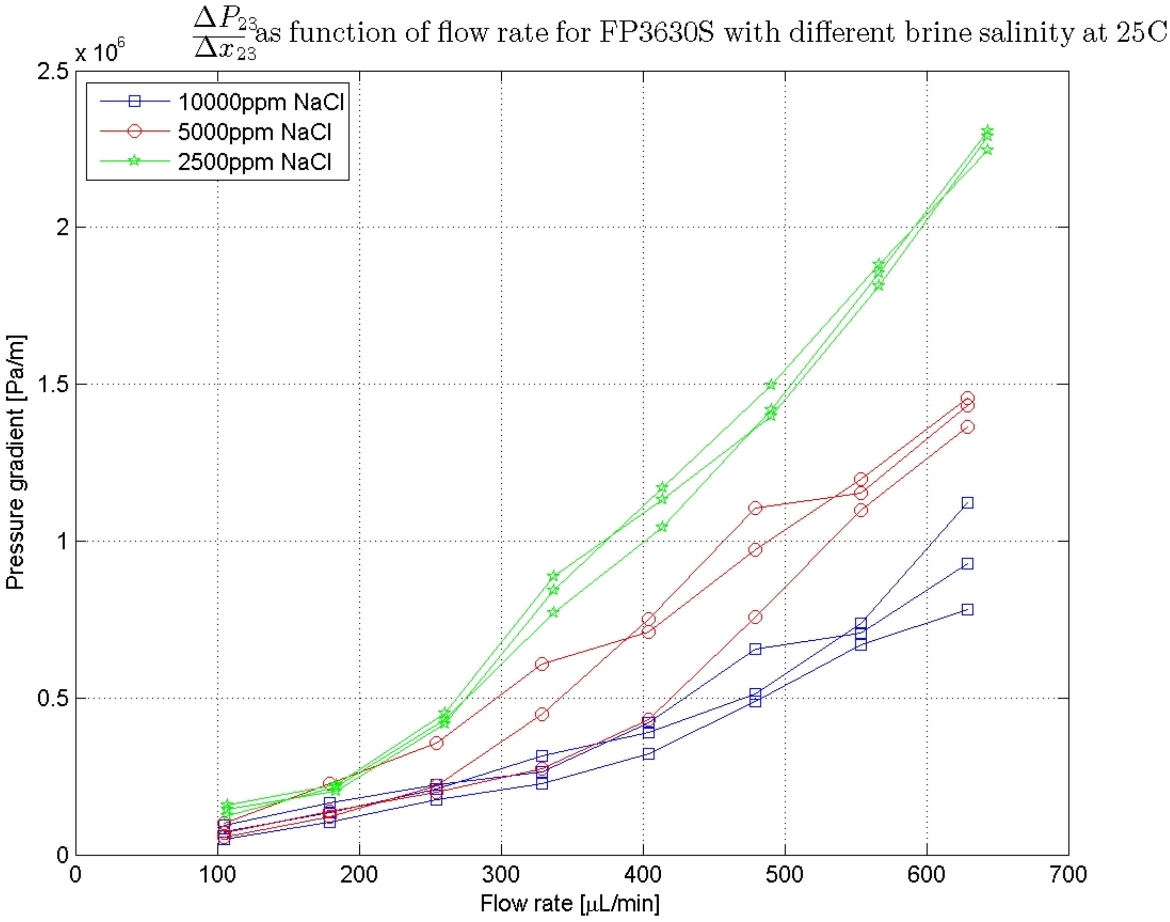

Figure 4.12: The effect of salinity on the extensional behaviour of FP3630S.

5

MODELLING

This chapter starts with a short description of the different modelling tools used in this research (GeoDict, COMSOL Multiphysics and Matlab). This section is followed by a modelling study on the experiments done with the e-VROC (Chapter 4). The last sections of the chapter are dedicated to a pore network modelling study that investigates the effect of shear and elongation viscosity on the redistribution of a macroscopic pressure drop inside a porous medium.

5.1. MODELLING TOOLS

5.1.1. GEODICT

Based on the morphology and geometry of a material or system GeoDict can predict the properties of the material/system. To assess the properties of porous media or a microfluidic device, the FlowDict Module can be used. The FlowDict module computes the material properties by solving for laminar incompressible, stationary Newtonian flows. This can be done with two kind of boundary conditions [37]:

1. Prediction of mean flow velocity for a given pressure drop.
2. Prediction of the pressure drop for a given mean flow velocity.

From the results pressures and fluid velocities at various positions within the porous media or microfluidic cell can be extracted.

5.1.2. COMSOL MULTIPHYSICS

COMSOL Multiphysics can be used to solve a variety of physical problems, considering one or multiple coupled phenomena. COMSOL solves the partial differential equations associated with the coupled phenomena using a finite element analysis. To solve the flow through the e-VROC, the Computational Fluid Dynamics (CDF) module of COMSOL Multiphysics 4.3 was used. This module allows you to solve fluid flow for numerous fluid flow applications and enables you to incorporate compressible, isothermal, Non-Newtonian, two-phase and porous media flow, both in the laminar and turbulent regime [38].

5.1.3. MATLAB

The pore network modelling code was developed in Matlab 7.11.0 (R2010b). The numerical computing environment of Matlab allows vector/matrix calculations, implementation of algorithms, numeric computing and the analysis and visualization of data using programming languages such as C, C++ and Fortran.

5.2. eVROC NUMERICAL MODELLING

In this section the Newtonian experimental measurements within the e-VROC are validated by numerical simulation. Multiple numerical techniques are used, GeoDict and COMSOL Multiphysics 4.3.

5.2.1. NEWTONIAN VALIDATION

GEODICT

Calculated profiles of the axial (stream wise) and lateral velocity components at the center ($z = \frac{h}{2}$) of the e-VROC at various axial positions are given in Figure 5.1. Far away from the contraction, the velocity profile corresponds to developed flow in a rectangular duct. Moving closer to the contraction the flow is focussed towards the centreline. The maximum axial velocity is found at the centreline ($x = 0$) and increases substantially moving towards the contraction. Furthermore, the lateral velocity increases while moving towards the contraction. However the lateral velocity also decreases again as the change in contraction width decreases.

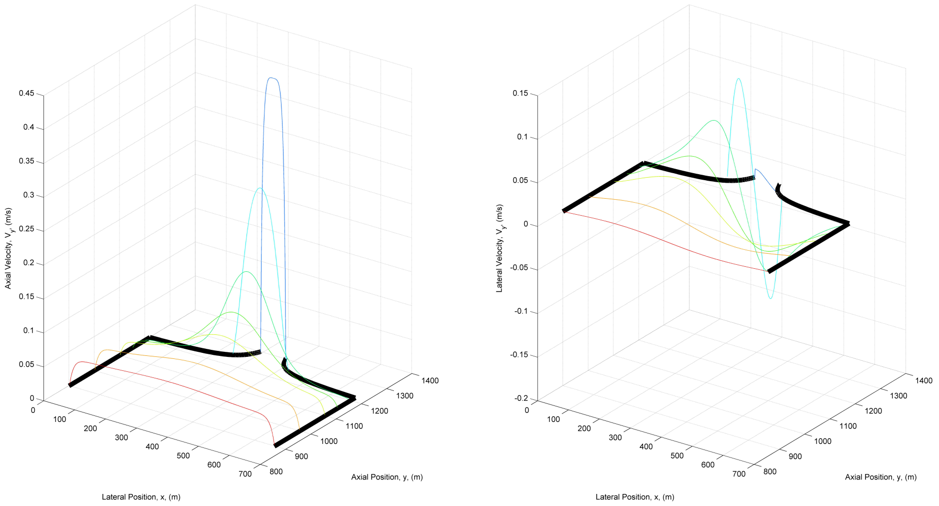

Figure 5.1: Axial and lateral velocity profiles at the center plane ($z = \frac{h}{2}$) determined numerically for several axial and lateral positions using GeoDict.

Figure 5.2 shows the velocity contour plots of the flow in all three spatial dimensions and their resulting magnitude at the center plane ($y = \frac{h}{2}$). As observed previously in Figure 5.1 the axial velocity component has its maximum at the centreline, whereas two off-center maxima can be observed for the lateral velocity component. This can be explained by the relative large depth of the channel. This causes the momentum diffusion in the x-y plane to dominate over diffusion in the z-direction. In this case, the flow in the center plane ($y = \frac{h}{2}$) approaches 2D Stokes flow. Therefore only one maximum for the axial velocity exists. Whereas two off-center maxima for the lateral velocity exist [32].

Flow convergence far before the contraction area can be observed in the pressure profile along the axial flow direction. The pressure gradient at the second pressure sensor (905) differs almost 10% from the pressure gradient at the inlet of the channel, whereas the difference equals 0.1% at the first pressure sensor (405). This indicates that significant flow convergence occurs between pressure sensors 1 and 2. This causes a higher pressure drop and therefore an apparent viscosity increase compared to flow through a microfluidic rectangular duct. Also a non-zero velocity component in the z-direction exists. However, the magnitude is small (order -4).

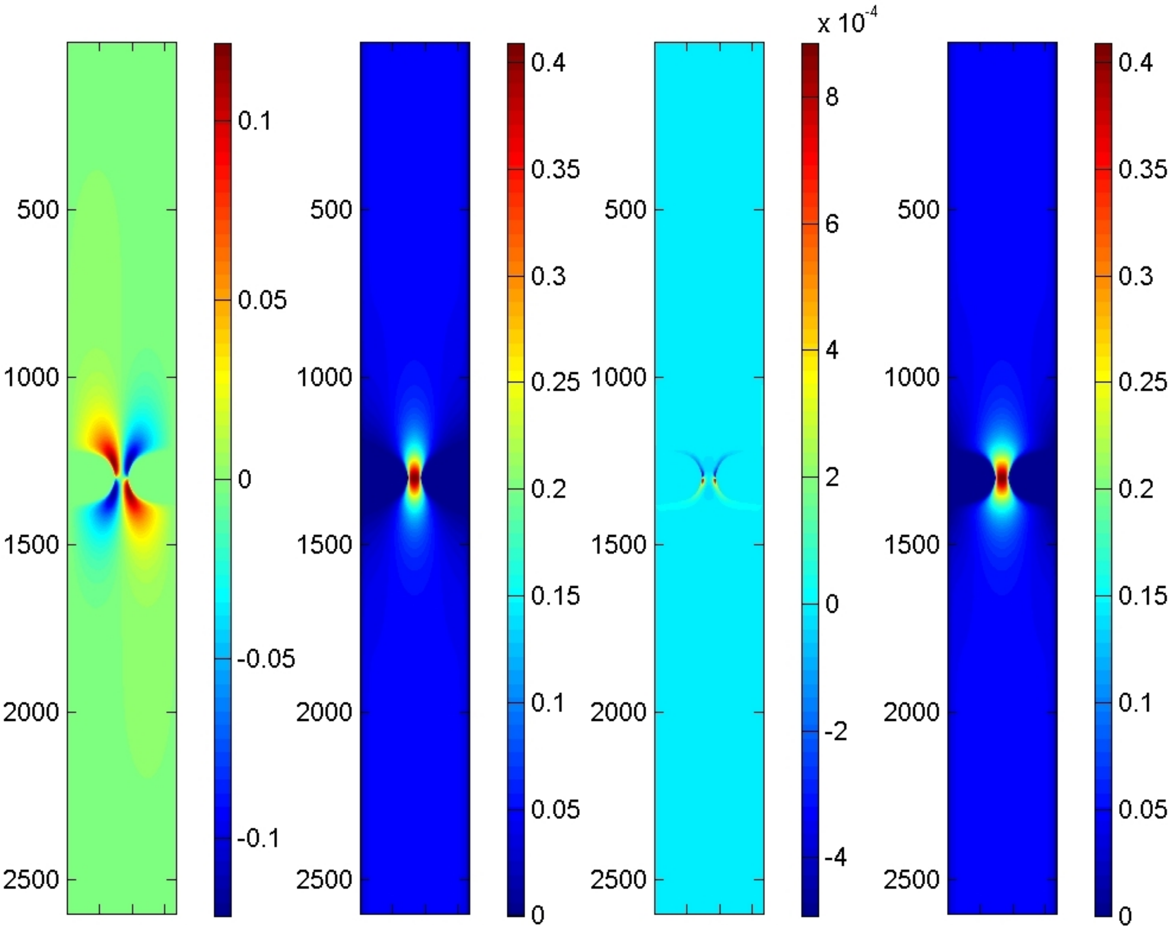

Figure 5.2: The velocity contour plots of the flow in all three spatial dimensions at the center plane ($y = \frac{h}{2}$) using GeoDict. Respectively, the lateral, axial, z-direction velocity and their resulting magnitude.

Finally, the experimental pressure data for Newtonian flow is compared to the numerical result in Figure 5.3. Also the contours of the pressure distribution is shown. The experimental data fits reasonably well with the numerical result. The difference can be explained by the non-ideal discretization since GeoDict can only handle cubic grid blocks. Therefore, errors in the dimensions of the geometry are induced causing the difference between the numerical and experimental data. Note that since the dimensions change, also the aspect ratio between the slit width and the width of the contraction slightly changes.

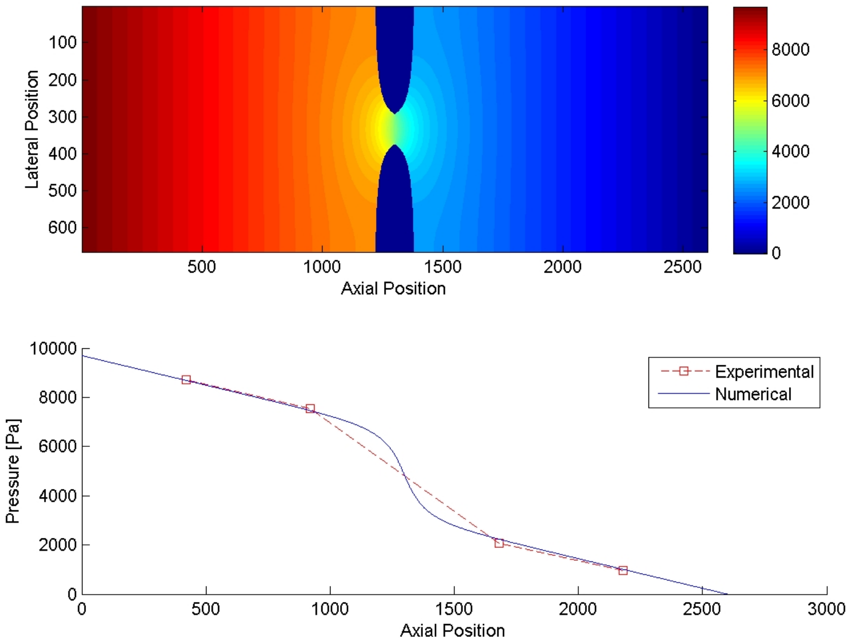

Figure 5.3: Contour plot of pressure distribution with e-VROC geometry and a comparison of experimental and numerical results of pressure profile along the flow direction at the centreline ($x = 0$) for fluid N50.

COMSOL Multiphysics

Similar to Figure 5.1, the axial (stream wise) and lateral velocity profiles at the center ($z = \frac{h}{2}$) of the e-VROC are given at various axial positions in Figure 5.4. Although more irregular compared to the GeoDict simulation, the velocity profiles generally have the same shape and are of the same magnitude as the profiles from the GeoDict simulation.

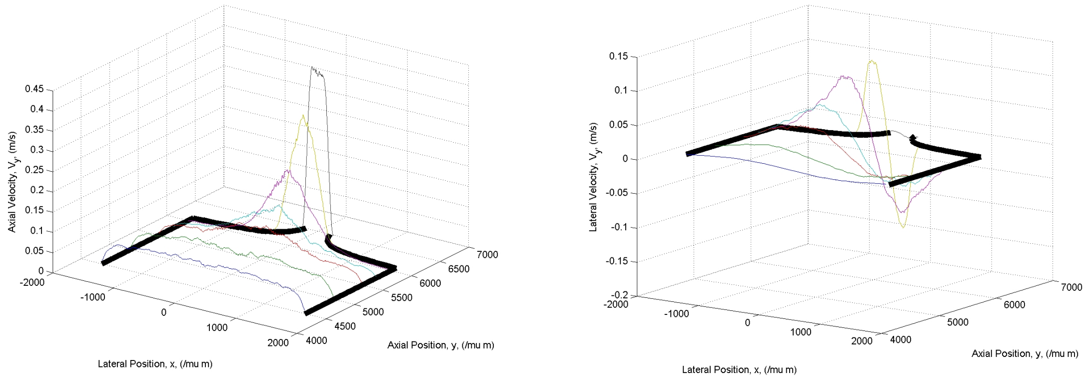

Figure 5.4: Axial and lateral velocity profiles at the center plane ($z = \frac{h}{2}$) determined numerically for several axial and lateral positions using GeoDict.

Again, the experimental pressure data for Newtonian flow is compared to the numerical results in Figure 5.5. Also this pressure profile fits reasonably well with the experimental data. In Section 4.1.3 it was already stated that the the edges of the e-VROC were not completely sharp but rounded. According to [29] the real cross-sectional area of the contraction could be 10-20% smaller than the designed cross-sectional area. This difference could explain the difference between the numerical and experimental pressure profile. The error made by COMSOL is larger than the error made by GeoDict. The opposite would be expected since the correct geometry is used in the COMSOL simulation. Whereas, in GeoDict the geometry is non-ideal discretized of GeoDict due to cubic grid blocks. Apparently, these dimension changes in the GeoDict simulation are such that the predicted pressure drop is closer to the actual pressure drop.

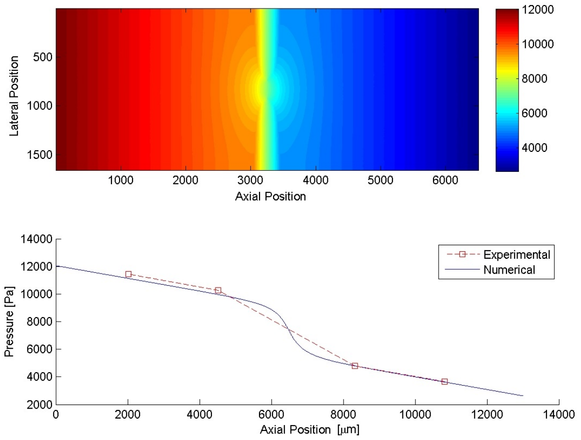

Figure 5.5: Contour plot of pressure distribution with e-VROC geometry and a comparison of experimental and numerical results of pressure profile along the flow direction at the centreline ($x = 0$) by COMSOL for fluid N50.

5.2.2. POLYMER FLOW

From the experimental pressure data it is evident that the extensional viscosity dominates as compared to the shear viscosity of polymer solutions. Still the flow of FP2500, FP5000 and FP10000 through the e-VROC is modelled with COMSOL Multiphysics using the shear-thinning Carreau viscosity model (Equation 2.8). Consequently it simulates how much of the measured pressure drop can be attributed to pure shear losses. Tables 5.1 to 5.3 show the pressure drop over the e-VROC determined by the experiments compared to numerical pressure drop determined by COMSOL for the three different polymer solutions at different flow rates. Tables 5.1 to 5.3 clearly show that the relative contribution of shear to the total pressure drop is highest at lower flow rates. This relative contribution decreases with increasing flow rate and increases with salinity. This indicates that the strain-thickening (extensional) behaviour of the polymer solutions becomes more dominant at higher flow rates and lower salinity. Furthermore, the tables show that the numerical pressures drop (shear only) determined by COMSOL do not significantly decrease when the salinity is increased from 5000 to 10000ppm NaCl. However a significant decrease in pressure drop is still observed in the experiments (both shear and extension). From this it can be concluded that the impact of salinity on the extensional viscosity of HPAM solutions is more extensive than on the shear viscosity.

Extensional rate [μ**L/min**]	$\Delta \mathbf{P}_{\mathbf{tot,num}}$ [**Pa**]	$\Delta \mathbf{P}_{\mathbf{tot,exp}}$ [**Pa**]	$\frac{\Delta \mathbf{P}_{\mathbf{tot,num}}}{\Delta \mathbf{P}_{\mathbf{tot,exp}}}$
107.3	265	511	0.52
183.8	400	864	0.46
260.4	528	1,673	0.32
337	652	2,944	0.22
413.7	775	4,008	0.19
490.3	895	5,421	0.17
566.9	1014	7,070	0.14
643.4	1132	8,780	0.13

Table 5.1: The predicted pressure drop over the e-VROC by COMSOL Multiphysics compared to the measured pressure drop for FP2500.

Extensional rate [μ**L/min**]	$\Delta \mathbf{P}_{\mathbf{tot,num}}$ [**Pa**]	$\Delta \mathbf{P}_{\mathbf{tot,exp}}$ [**Pa**]	$\frac{\Delta \mathbf{P}_{\mathbf{tot,num}}}{\Delta \mathbf{P}_{\mathbf{tot,exp}}}$
107.3	265	307	0.79
183.8	334	565	0.59
260.4	411	781	0.53
337	479	1063	0.45
413.7	542	1668	0.32
490.3	600	2912	0.21
566.9	655	4203	0.16
643.4	707	5208	0.14

Table 5.2: The predicted pressure drop over the e-VROC by COMSOL Multiphysics compared to the measured pressure drop for FP5000.

Extensional rate [μ**L/min**]	$\Delta \mathbf{P}_{\mathbf{tot,num}}$ [**Pa**]	$\Delta \mathbf{P}_{\mathbf{tot,exp}}$ [**Pa**]	$\frac{\Delta \mathbf{P}_{\mathbf{tot,num}}}{\Delta \mathbf{P}_{\mathbf{tot,exp}}}$
107.3	180	257	0.70
183.8	255	452	0.56
260.4	320	713	0.45
337	379	1103	0.34
413.7	435	1485	0.29
490.3	487	2004	0.24
566.9	538	2835	0.18
643.4	586	4179	0.14

Table 5.3: The predicted pressure drop over the e-VROC by COMSOL Multiphysics compared to the measured pressure drop for FP10000.

5.3. PORE NETWORK MODELLING

At the microscopic scale the void space of a porous medium is represented by a lattice of pores connected by throats. A voxel representation of the network can be obtained by a CT-scan image of the porous medium, shown in Figure 5.6. To make calculations easier this voxel representation is converted into a topologically equivalent network of pores and throats (Figure 5.6).

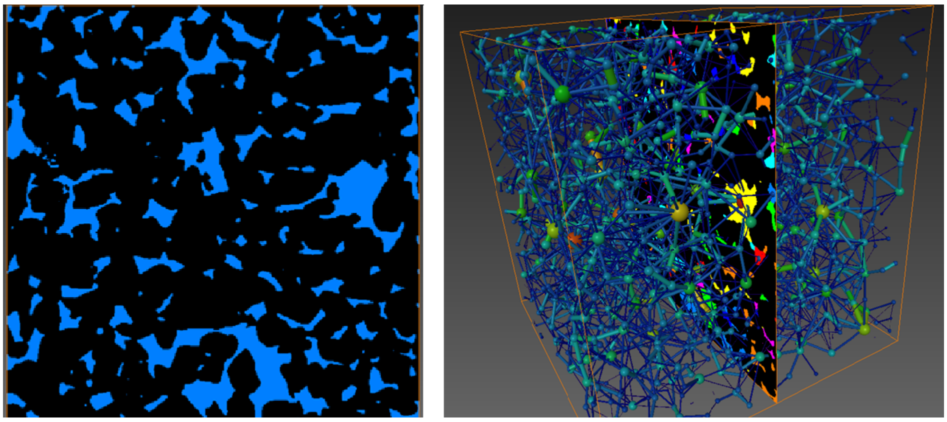

Figure 5.6: A 2D slice of the 3D CT voxel image of a rock sample and the equivalent network representation.

This so-called pore network extraction was done with the pore-network extraction code developed by Imperial College [39]. The pore networks were generated from a rectangular subset of a Boise sandstone plug with a permeability of 4.5 Darcy and a Berea sandstone with permeability of 1.1 Darcy taken from the Imperial College Department of Earth Science and Engineering website [40]. The properties of the networks used in this work are given in Table 5.4 and the sample analysis is given in Appendix G.

	Dimensions				**Core Analysis**		
Rock Sample	**x**	**y**	**z**	**Resolution** [μm]	**Permeability [mD]**	**Number of pores**	**Number of throats**
Boise	441	438	719	5	8500	8831	24812
Berea	400	400	400	5.345	1900	5341	11899

Table 5.4: The properties of rectangular subset of the Boise and Berea sandstone. The permeability of the samples were determined numerically by GeoDict.

5.3.1. MODEL FEATURES

In this work we assume that the pores can be represented by spheres and the connecting throats by circular sinusoidal tubes (Figure 5.7). Although the throats are asymmetrical along the flow direction, the corresponding elastic effects (energy storage and release) are neglected in this model. In the model it is assumed that the shape between the centres of two pores can be described by a sinusoidal tube varying between the pore body radii and the throat radius. By applying certain rules governing the transport between these pores, both macroscopic properties such as permeability and microscopic properties (pressure drop between pores) can be estimated for a given network.

The radius of the sinusoidal tube is given by:

$$R = R_t\left(1 + asin\left(\frac{2\pi z}{\lambda}\right)\right) \tag{5.1}$$

where $a = \frac{R_s}{R_t}$ is the normalized amplitude.

MATHEMATICAL FORMULATION

Here we follow the approach as used by Denys [20]. Denys derived an analytical expression for flow of a polymer liquid through a circular sinusoidal tube. Assuming the flow is at steady state and incompressible, the total pressure drop during flow can be be calculated by making use of the mechanical energy balance [20]:

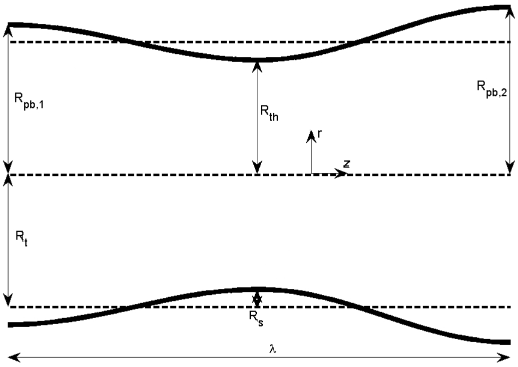

Figure 5.7: 2D-schematic of sinusoidal tube equivalent to a pore throat.

$$\Delta P_{tot} = \frac{1}{Q}\left(\int_V \left(\underline{\underline{T}}:\underline{\underline{D}}\right) dV - \int_S \underline{\underline{T}}\cdot\underline{v}\cdot\underline{n} dS\right) = \frac{1}{Q}\left(\int_{z=0}^{L}\int_{r=0}^{R} \left(\underline{\underline{T}}:\underline{\underline{D}}\right) 2\pi r dr dz - \int_S \underline{\underline{T}}\cdot\underline{v}\cdot\underline{n} dS\right) \tag{5.2}$$

here $T : D$ is the double contraction of the stress tensor and the rate of deformation tensor. The negative second term in Equation 5.2 describes the difference in surface forces between the beginning and end of the tube. Since elastic contributions are neglected, this term is not relevant.

In the derivation, Denys furthermore assumes that both the shear and elongational viscosity can be described as power-laws:

$$\eta_{elo} = g|\varepsilon|^{h-1} \tag{5.3}$$

$$\eta_{sh} = m|\gamma|^{n-1} \tag{5.4}$$

where g and m are the zero-strain and zero-shear viscosities respectively, ϵ the strain rate, γ the shear rate and h and n fluid exponents. For Newtonian fluids $n = h = 1$, for shear-thinning and strain-thinning fluids $n < 1$ and $h < 1$. Strain-thickening effects are described by $h > 1$.

Using Equations 5.3 and 5.4 it can be shown that:

$$\underline{\underline{T}}:\underline{\underline{D}} = \sum_{i,j} T_{ij} D_{ji} = g|\varepsilon|^{h+1} + m|\gamma|^{n+1} \tag{5.5}$$

LUBRICATION APPROXIMATION

The flow field in slowly varying geometries can be approximated by the Lubrication Approximation Method. In this method the results of an uniform geometry is locally adapted to a slowly varying geometry. The Lubrication Approximation Method holds if:

$$W = \frac{8a}{b\,(1+a)^2\,(1-a)^2} \ll 1 \tag{5.6}$$

and

$$\frac{\rho_f Q W}{\pi \eta_{sh} R_t} \ll 1 \tag{5.7}$$

where $b = \frac{\lambda}{R_t}$.
Assuming power-law behaviour and no-slip at the wall, the velocity in the direction of flow yields:

$$v_z = \frac{3n+1}{n+1}\frac{Q}{2}\left(1-\beta^{1+\frac{1}{n}}\right) \tag{5.8}$$

and the velocity perpendicular to the flow direction:

$$v_r = \beta v_z R_z \tag{5.9}$$

where $\beta = \frac{r}{R}$ and $R_z = \frac{dR}{dz}$
The derivatives of Equation 5.8 towards z and r give the elongational and shear rate respectively:

$$\varepsilon = \frac{3n+1}{n+1}\frac{Q}{\pi R^3}\left(\frac{3n+1}{n}\beta^{1+\frac{1}{n}} - 2\right)R_z \tag{5.10}$$

$$\gamma = \frac{3n+1}{n}\frac{Q}{\pi R^3}\beta^{\frac{1}{n}} \tag{5.11}$$

Combining Equations 5.1 to 5.11 gives the expression for the total pressure over a sinusoidal tube, which consists of two terms:

Elongational term:

$$\Delta P_{elo} = 4g\left(\kappa^2 - \kappa^{\frac{3n+1}{n}}\right)\left(\frac{2\pi a R_t}{\lambda}\right)^{h+1}\left(\frac{3n+1}{n+1}\right)^{h+1}\left(\frac{Q}{\pi R_t^3}\right)^{h}\frac{I_a}{R_t} \tag{5.12}$$

where $\kappa = \sqrt[\frac{n+1}{n}]{\frac{2n}{3n+1}}$
Shear term:

$$\Delta P_{sh} = 2m\left(\frac{3n+1}{n}\right)^{n}\left(\frac{Q}{\pi R_t^3}\right)^{n}\frac{I_b}{R_t} \tag{5.13}$$

where I_a and I_b are integrals:

$$I_a = \int_{z=0}^{\lambda}\frac{|cos(\frac{2}{\lambda})|^{h+1}}{(1+asin(\frac{2}{\lambda}))^{3h+1}}dz \tag{5.14}$$

$$I_a = \int_{z=0}^{\lambda}\frac{1}{(1+asin(\frac{2}{\lambda}))^{3n+1}}dz \tag{5.15}$$

For Newtonian fluids I_a and I_b can be computed analytically, which gives:

$$I_a = \lambda\frac{\frac{1}{2}}{(1-a^2)^{\frac{5}{2}}} \tag{5.16}$$

$$I_b = \lambda\frac{1+\frac{3}{2}a^2}{(1-a^2)^{\frac{7}{2}}} \tag{5.17}$$

It can be shown that the pressure drop due to elongation (Equation 5.12) cancels out in the limit of a cylindrical tube geometry ($a = 0$). Furthermore, it can be shown that Equation 5.13 reduce to Hagen-Poiseuille's law for Newtonian fluids ($n = h = 1$) in the limit of a cylindrical tube geometry. Equation 5.12 and 5.13 can be simplified to (note R_{elo} and R_{sh} are n and h dependent):

$$\Delta P_{tot} = R_{elo}Q^h + R_{sh}Q^n \tag{5.18}$$

By applying this equation as the transport rule between pores and a volume conservation in each pore:

$$\sum Q_{i,j} = 0 \tag{5.19}$$

the flow through the pore network can be solved by specifying boundary conditions at the inlet and outlet of the system.

5.3.2. NUMERICAL CODE DESCRIPTION

A schematic flow chart of the numerical code to solve (non-linear) flow through the pore network is shown in Figure 5.8. First the network and its properties are loaded. After which the isolated pores and dead-end branches are removed with a deletion algorithm, since these pores (and throats) do not contribute to the flow from inlet to outlet. Secondly, the fluid parameters (zero-rate viscosities and fluid exponents) are specified. From both the pore and throat properties and the fluid properties the resistance to shear and elongational flow between each pore can be calculated using Equations 5.12 to 5.17. The equations by Denys assume a sinusoidal tube varying between two values (i.e. one R_s). However since two connected pores do not have the same radius (Figure 5.7), the resistance to shear and elongational flow for the left and right side of the pore throat are calculated separately using Equations 5.12 to 5.18. The total resistance to shear and elongational is assumed to be the summation of the resistance of left and right part of the throat.

The system is solved by first solving the flow through the throats (Equation 5.18) for flow rate at the given pore pressures using a combined Secant and Regula-Falsi method [41]. This method is able to simultaneously solve scalar non-linear algebraic equations as long as the equations are monotonically increasing and properly scaled. The calculated flow rates between the pores from the secant method are then supplied to the fsolve routine of Matlab to do one iteration step in solving Equation 5.19 ($\sum Q_{i,j} = 0$). The corresponding pore pressures are again supplied to the secant solver to solve the flow through the throats (Equation 5.18). This loop continues until the flow rates between the pores satisfy both Equation 5.19 ($\sum Q_{i,j} = 0$) and the flow through the throats (Equation 5.18).

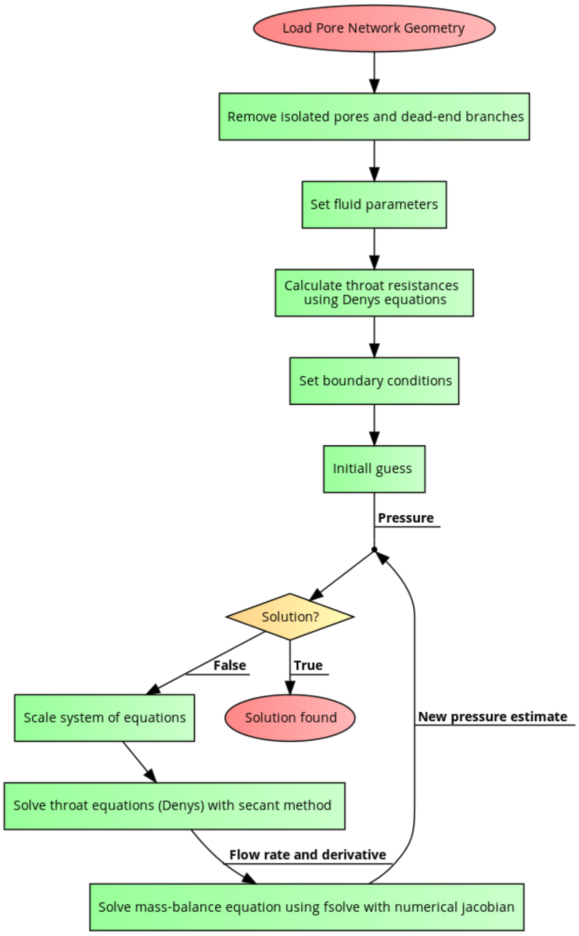

Figure 5.8: Flow chart describing the numerical code to solve the (non-linear) flow through a pore network.

5.3.3. RESULTS

This section will discuss the results of the pore network modelling. The main focus is on how a macroscopic pressure drop is redistributed in microscopic pressure drops between individual pores. First, the results of the pore network model for Newtonian flow are compared to the results given by GeoDict using the actual micro-CT image. Secondly, a comparison is made between the microscopic pressure drop distributions of Newtonian and Non-Newtonian flow using pore network modelling. Non-Newtonian flow is divided in fully shear-thinning flow (the strain-thickening effect is not incorporated) and actual polymer behaviour (both shear-thinning and strain-thickening). Table 5.5 gives an overview of the used fluid properties and boundary conditions.

Nr.	**Fluid Type**	**h**	**m** [Pa s^n]	**n**	**Total pressure** [Pa]	**Iterations Boise**	**Iterations Berea**
1	Newtonian	1	1e-3	1	36Pa	11	10
2	Shear-thinning	1	10e-3	0.75	36Pa	146	102
3	Shear-thinning	1	10e-3	0.55	36Pa	974	462
4	Shear-thinning Strain-thickening	1.25	10e-3	0.75	36Pa	92	28
5	Shear-thinning Strain-thickening	1.5	10e-3	0.75	36Pa	64	89
6	Shear-thinning Strain-thickening	1.5	10e-3	0.75	1800Pa	190	139
7	Shear-thinning Strain-thickening	1.5	10e-3	0.75	3600Pa	231	127
8	Shear-thinning Strain-thickening	1.5	10e-3	0.75	5400Pa	214	134

Table 5.5: The used fluid properties and pressure drops in the pore network models together with the number of iterations needed for the solver to converge. Note that $\frac{g}{m} = 3$ since the throats are assumed to be circular.

NEWTONIAN FLOW

Figure 5.9 shows the probability density functions of the relative pressure drop between pores to the total pressure drop for the Boise sandstone sample for both the GeoDict and pore network modelling. Furthermore, the mean (μ), variance (σ), skewness (b) and kurtosis (g) of both probability density functions are given (Appendix H). The variance is a measure for how big the spread of numbers in the sample set is. The higher the variance the bigger the spread. The skewness is a measure for how asymmetrical the sample set is around its mean. If the skewness equals zero the sample set is symmetric around its mean. A large negative number indicates a long tail to the left of the mean, whereas a large positive number indicates a long tail to the right of the mean. Kurtosis is also a measure for the shape of a distribution. If the kurtosis is smaller than zero, it indicates that the distribution is flatter than a log normal distribution. Whereas, a positive number indicates that the distribution is more peaked.

Despite the pore network model being an abstraction of reality, the pressure distributions of GeoDict and the pore network model are in good agreement. The Pore Network Modelling assumes circular pore throats whereas in reality this is rarely the case and the throats are more irregular and slit like. Furthermore, the Lubrication Approximation Method for small varying geometries is assumed to be valid (Equations 5.6 and 5.7). However, for the Boise sandstone sample, only 30% of the pore throats Equation 5.6 (W) has a value below 0.5 and for only 3% of the pore throats this value is below 0.01. Therefore, it can be concluded that generally the lubrication approximation for slowly varying geometries is not valid. This gives rise to errors.
The variance (σ) and kurtosis (g) of the GeoDict result is smaller compared to the pore network modelling result. This indicates a less peaked and less spread distribution. The mean value of relative pressure drop is around zero. Physically this implies that whereas the pore network modelling predicts no or little pressure drop between certain pores (hence no or little flow), GeoDict still predicts (a larger) flow. The variance and kurtosis for the Berea sandstone is more than twice as high as for the Boise sandstone. The pressure drop distribution for the Berea has more spread and is more peaked than for the Boise sandstone, indicating less conformance control. This can be attributed to the fact that the Berea sample on average has a lower pore connection number.

From the resulting flow rates the permeability of the samples can determined. The permeability according to the pore network modelling for the Boise sample is 620mD. Almost a factor of 14 lower than the permeability determined by GeoDict. The permeability predicted by the pore network modelling for the Berea sample is 160mD. A difference of a factor of 12 with the permeability determined by GeoDict. From this it can be concluded that although the predicted pressures in the pores are in agreement with GeoDict, the corresponding flow rates are too low. However, qualitative interpretation of the (changed) flow behaviour for Non-Newtonian flow can still be made.

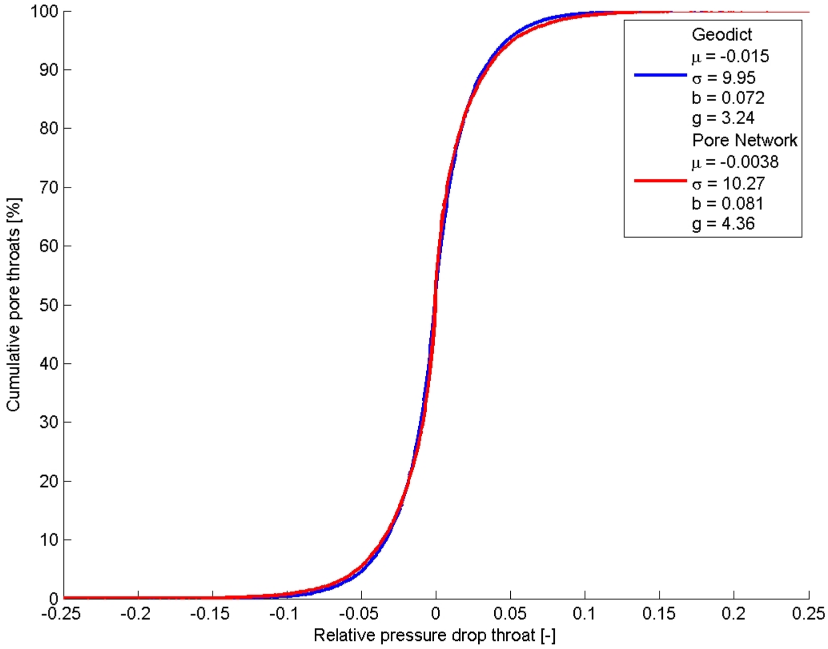

Figure 5.9: The probability density functions of the relative pressure drop between pores to the total pressure drop for the Boise sandstone sample for both GeoDict and the pore network modelling.

NON-NEWTONIAN FLOW

In this section the effect of the fluid exponents n (shear) and h (extension) on the relative pressure distribution will be investigated. First only the effect of shear-thinning is investigated. Secondly, also the effect of strain-thickening in combination with shear-thinning on the flow will be discussed.

Shear-thinning Flow Figure 5.10 shows the probability plots of the relative pressure drop between pores to the total pressure drop for the Boise and Berea sandstone sample for Newtonian and Non-Newtonian shear-thinning flow ($n < 1$ and $h = 1$). The pressure drop over the sample was kept constant. A straight line indicates that the distribution is normally distributed. The mean of the distributions is where the plots intersect with a probability of 0.5. The variance is indicated by the slope of the plot, the higher the slope the lower the variance. Any skew in the data set will show a bend (up or down) of the straight line. High positive kurtosis makes the curve more S-shaped.

It can be observed that as the exponent n decreases also the variance (σ) and kurtosis (g) decrease. This indicates that the relative pressure drop distribution has less spread and is less peaked compared to Newtonian flow. Physically, this implies that compared to Newtonian flow, flow passes through parts that are by-passed by a Newtonian fluid. Also the pressure drop has less spread indicating better conformance control for Non-Newtonian shear-thinning flow.

The effect is biggest in the Berea sample due to the lower average pore connection number of the network compared to the Boise network. From this it can be concluded that the Berea network has less interconnected flow paths. Therefore, heterogeneities in the throat resistances will have a bigger impact on the flow behaviour in the porous medium. The shear-thinning behaviour of the polymer reduce this heterogeneity effect, therefore the effect of shear-thinning is best visible in the Berea sample.

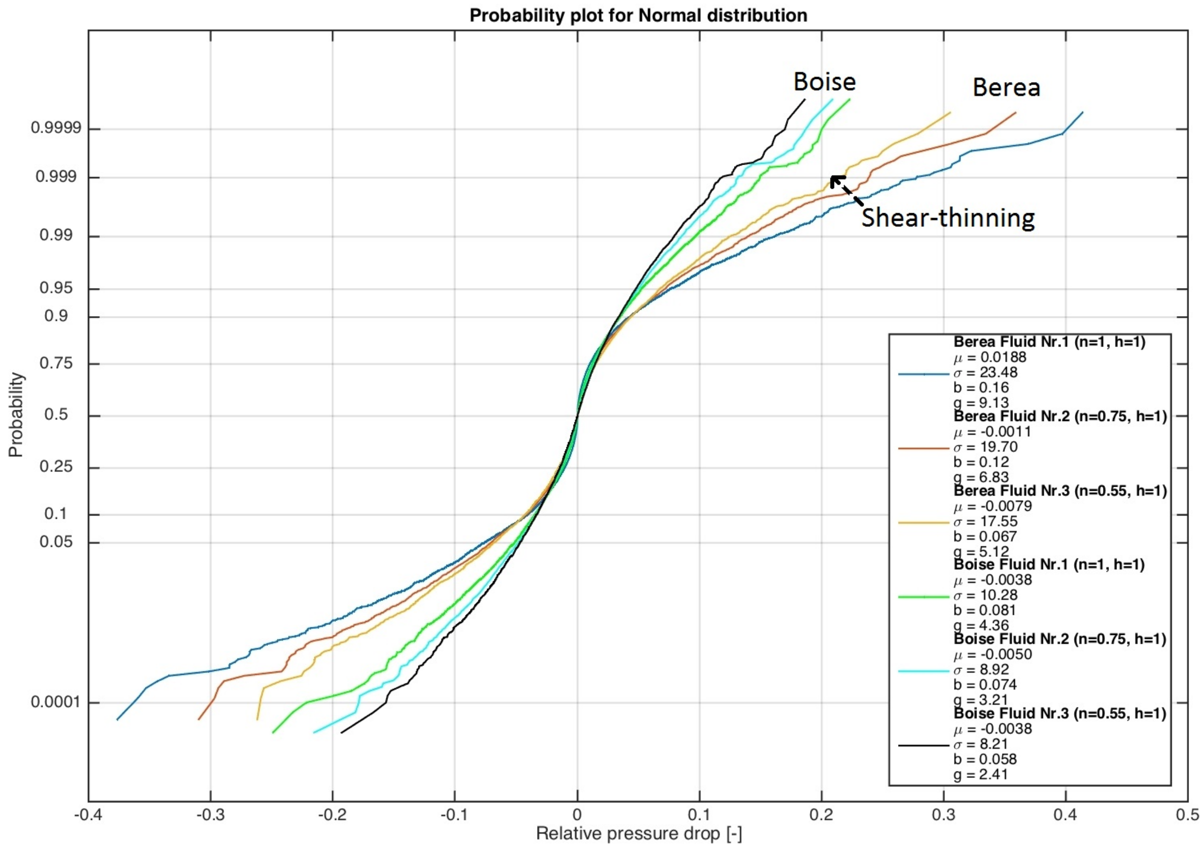

Figure 5.10: The probability plots of the relative pressure drop between pores to the total pressure drop for the Boise and Berea sandstone samples for different shear exponents n.

Shear-thinning And Strain-thickening Flow A schematic representation of Equation 5.18 is shown in Figure 5.11. Polymer solutions generally show shear-thinning and extension-thickening behaviour ($n < 1$ and $h > 1$). The pressure drop is first dominated by shear flow. However, beyond a critical flow rate the extensional forces dominated the flow.

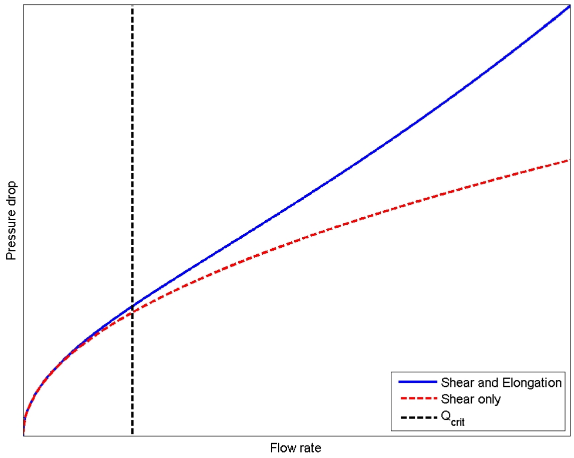

Figure 5.11: Schematic representation of Equation 5.18 describing the pressure flow rate behaviour between pores.

At pressure drops of 324Pa the flow rate in most throats is below the critical flow rate (Figure 5.11). Therefore, the flow between the majority of pores is shear dominated (1.3% and 1.9% of the throats are elongation dominated for Boise and Berea network respectively). With dominate, it is meant that the shear contribution to the pressure drop is bigger than the elongational contribution but elongational forces are not necessarily negligible. Consequently, a change in the elongational behaviour of the fluid will not significantly alter the behaviour of the fluid inside the porous medium. Also experimental studies have shown that the extensional behaviour becomes dominant at higher flow rates and pressure drops [42]. To study the effect of extensional viscosity on the flow behaviour the pressure gradient over the samples should be increased such that the flow rate in enough throats exceeds the critical flow rate.

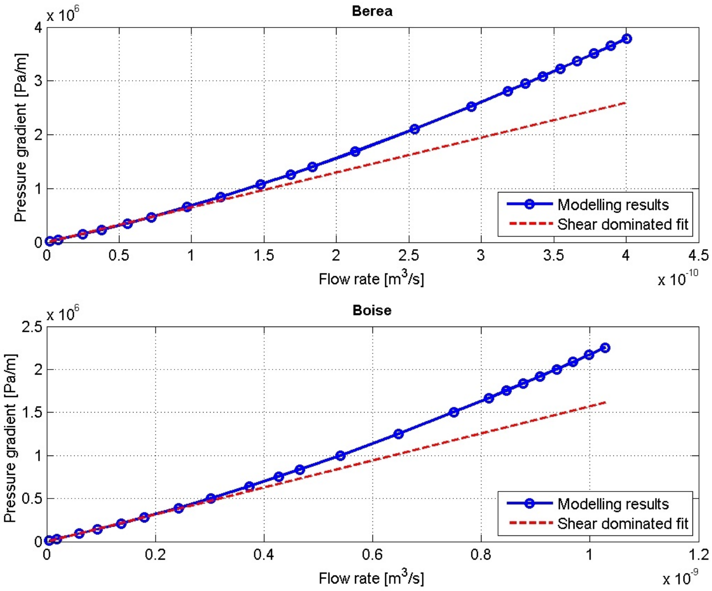

Figure 5.12: The pressure flow rate response of the Berea and Boise sample for a polymer solution ($n = 0.75$ and $h = 1.5$).

The pressure flow rate response of the Berea and Boise sample for a polymer solution (n = 0.75 and h = 1.5) is given in Figure 5.12. Two different slopes can be observed in the data. At first shear dominates the pressure drop from pore to pore. However when a certain flow rate is reached, extensional flow starts to dominated the flow and the slope increases. For both samples the transition occurs around a pressure difference of around 1800Pa. Note that the samples have different sizes and permeability. Therefore the transition is at different flow rates and macroscopic pressure gradients. Figure 5.13 shows that the transition occurs when roughly 40% of the actual flow is dominated by extension.

The probability plots of the relative pressure drop between pores to the total pressure drop of a shear-thinning and strain-thickening fluid (n = 0.75 and h = 1.5) are shown above 1800Pa to study the changed flow behaviour (Figure 5.14). The percentage of throats dominated by elongation is 17% and 19% for the Boise and Berea sample respectively at a macroscopic pressure drop of 1800Pa. For a macroscopic pressure drop of 5400Pa the percentage of throats dominated by elongation is around 37% for both the Boise and Berea sample (Figure 5.13). Increasing the pressure gradient increases the variance (σ) and kurtosis (g) of the pressure drop distributions in both samples. This indicates less conformance control. As the pressure gradient increases even more the relative impact decreases since the flow paths do not change.

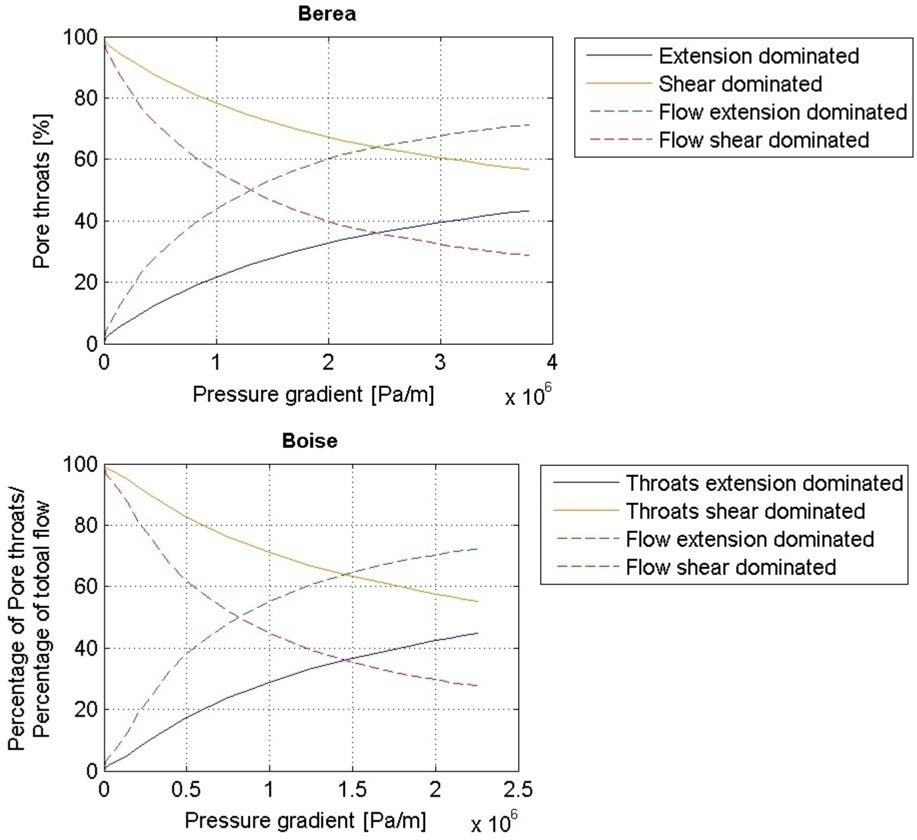

Figure 5.13: The percentage of throats and actual flow dominated by shear or extension for a polymer solution (n = 0.75 and h = 1.5).

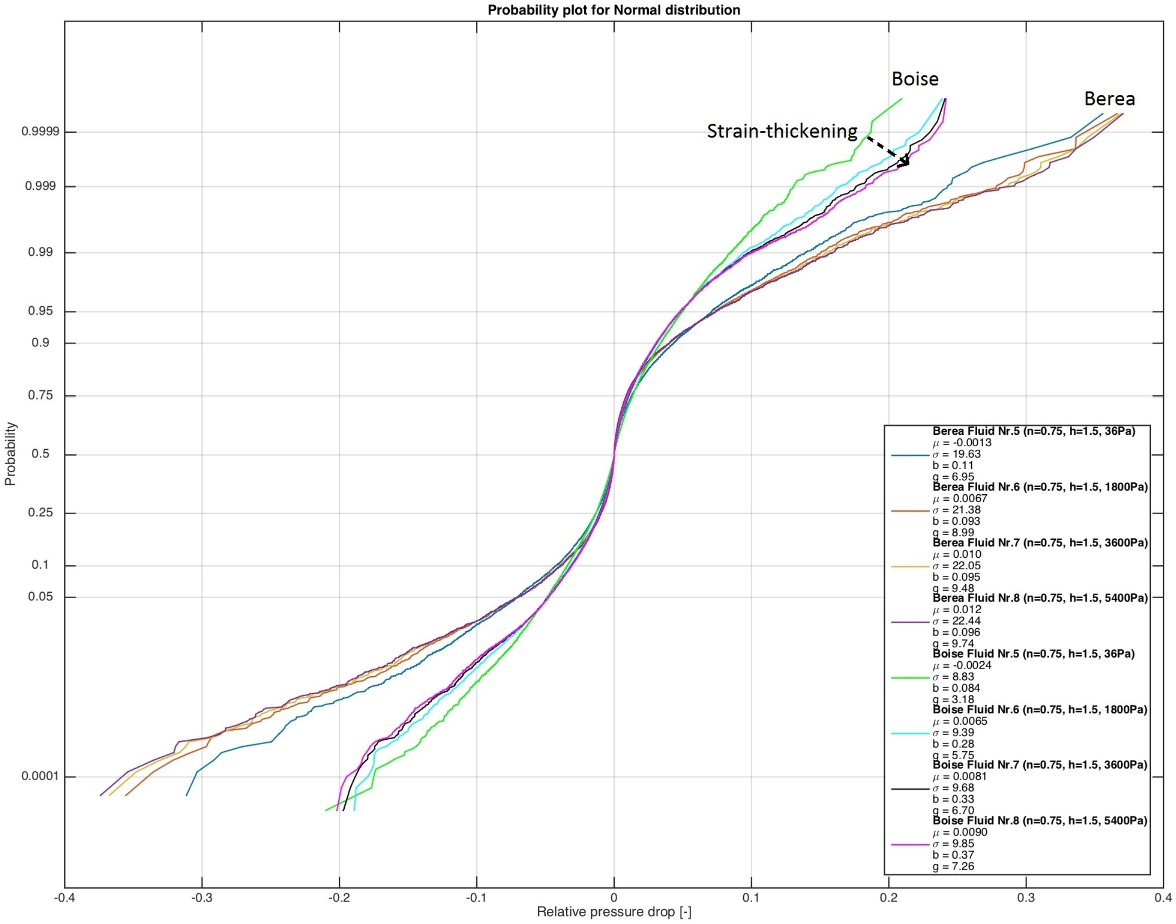

Figure 5.14: The probability plots of the relative pressure drop between pores to the total pressure drop for the Boise and Berea sandstone samples for shear-thinning and strain-thickening flow at different pressure gradients.

6

CONCLUSIONS

The conclusions drawn from this research will be split into two parts: conclusions regarding the experiments with the e-VROC and conclusion from the pore network modelling.

1. e-VROC
   (a) The provided analysis of the e-VROC pressure data (Section 3.2.2) is currently unable to determine the true extensional viscosity of a fluid. This followed from comparisons with Couette cell measurements using Newtonian fluids. The analysis can still be used as an extensional viscosity indexer in comparing different fluids.
   (b) Analytical analysis of the e-VROC geometry indicates that the shear component of the flow is large in the converging section – contrary to the claimed advantages of the hyperbolic geometry. Newtonian flow can therefore not be regarded as extension dominated.
   (c) The analytically derived equations (Equations 3.12 and 3.13) and Geodict/COMSOL simulations compare well with the experimental results and therefore can be used to estimate the pressure drop for Newtonian fluids.
   (d) A noisy pressure signal was observed when flowing HPAM3630S polymer. This is probably due to the elasticity of the solution. The residence time of the polymer in the contraction-expansion section is small (tens of milliseconds) as compared to the elastic relaxation time of the fluid (0.1-1 seconds). The latter thus predominates and shows in a pressure effect.
   (e) The resistance to extension of HPAM3630S solutions increases with increasing flow rate. Due to high flow rates near the wellbore, this may cause injectivity problems.
   (f) Adding salt to the polymer solution decreases the shear viscosity and also lowers the resistance to extension. As more salt is added to the solution more of the negative charges along the polymer chain are getting shielded by the Na+ ions, causing it to shrink in size (Section 1.3). This reduction in size reduces the flexibility of the polymer molecules, making them stiffer. Since the polymer molecules become stiffer, they are less likely to uncoil, making it easier to flow through a contraction-expansion geometry.
   (g) The e-VROC is an useful device to quantify the extensional behaviour of HPAM. However due to the large contribution of shear and low experimental reproducibility it is unable to quantify pure extensional behaviour.

2. Pore Network Modelling
    (a) The developed Matlab code enables modelling the steady state response of pore network systems. The systems contained more than 10000 non-linear throat equations. This captured both extension-thickening and shear-thinning pressure losses. This successfully demonstrated proof of concept set out at the beginning of this study. The current model (Section 5.3.1) cannot predict the permeability of the porous medium correctly.
    (b) The microscopic pressure drop distribution for Newtonian flow from the pore network modelling was in good agreement with the pressure drop distribution predicted by GeoDict.
    (c) Compared to Newtonian flow, the variance and kurtosis of the pressure drop distribution are smaller for purely shear-thinning flow (Table 5.5). This implies better conformance control in the network.
    (d) Above a critical flow rate, strain-thickening behaviour reverses this process. This increases the variance and kurtosis of the pressure drop distribution. This has a negative impact on conformance control.

7

RECOMMENDATIONS

The recommendations will be split into recommendations for both the experimental and numerical side of the research. Starting with the recommendations regarding the experimental side.

In this research the effect of salinity on the extensional behaviour of HPAM3630S was investigated, in the slit geometry of the e-VROC. Further work could also include the effects of polymer type, polymer concentration, divalent ion concentration and temperature on the extensional behaviour. These parameters may be assessed since different rocks require different polymer sizes (polymer type) due to the rock's permeability. Furthermore, the reservoir conditions will vary (temperature and brine composition) together with the oil viscosity requiring a different polymer viscosity (polymer concentration/type).

Also the time pressure signal stability and experimental reproducibility could be assessed while varying these parameters. In this way it might be possible to pinpoint the reason behind the stability and reproducibility problems.

Secondly, one would like to be able to predict the flow behaviour through a (far more complex) porous medium in the future. Such a porous medium will have multiple flow paths with consecutive contraction and expansion geometries. Before this can be achieved it is recommended to investigated the flow behaviour in a more simplistic geometry but more complex than the e-VROC geometry. Such a geometry may exist of two (or more) parallel flow paths each having a different amount of consecutive contractions. If possible it would be favourable to be able to close each flow path such that also the flow through one of these flow paths can be investigated. By having multiple consecutive contractions the effect of elasticity can be investigated which was not done in this research.

The recommendations regarding the improvement of the pore network modelling code cover both the performance and the physics of the model.The performance of the code can be improved in different ways. Although the code removes all dead-end branches and parts of the network that are not connected to the in- or outlet of the network, it does not use the internal structure of the network any further. Algorithms exist that are able to detect the shortest paths in networks and can identify parallel, paths and cycles in the networks. Making use of this knowledge, the flow through the network can be solved more efficiently. Although the fsolve routine of Matlab is quite robust, the performance is highly impacted when the non-linearity of the flow is increased. More work is needed to make the solver more efficient.

Furthermore, the physics in the model can be improved. At the moment the permeability of the rock sample is underestimated by more than one order of magnitude. From this it can be concluded that the resistance to flow between the pores is overestimated. This can have multiple causes: Either the pore network dimensions are not in agreement with the actual rock samples. Or the used transport equations overestimated the resistance to flow. More work can be done to investigate these possible causes. This may include the use of different pore network generator codes and comparing the predicted pressure drop for a pore throat geometry with the predicted pressure drop by COMSOL/GeoDict.

Furthermore, a shape factor could be included to correct the resistance to flow if the throat is non-circular. Secondly, it is assumed that the fluid is a power-law fluid, therefore as the rate approaches zero the viscosity of the fluid keeps on increasing. In reality the fluid will show Newtonian behaviour below a certain flow rate. This behaviour could be incorporated in the future model. If all these improvements are made, the modelling results could be tested against experimental work and other modelling work (GeoDict/OpenFOAM) using the micro-CT images for both Newtonian and Non-Newtonian flow.

A

RECOMMENDED EXPERIMENTAL PROCEDURE E-VROC

While carrying out the experiments with the e-VROC the following procedure was applied:

1. Will the syringe with the test sample. Be aware of any air bubble, since they can have a tremendous effect on the measurement.
2. Flush the e-VROC cell with a sufficient amount of test sample such that no air bubbles remain in the contraction-expansion geometry.
3. Let the test sample rest to allow the pressure field to equilibrate.
4. Flow the test sample through the e-VROC cell at the desired flow rates using an increasing sweep.

To determine the time needed to get a good quality measurement, it is recommended to flow the test sample at four different flow rates within the desired range for 15 to 20 minutes. From the pressure-time signals the minimum time needed for the flow to become stable can be determined.

B

ANALYTICAL DERIVATION OF NEWTONIAN FLOW IN THE E-VROC CELL

In this section an analytical derivation is made to determine the theoretical pressure drop contributed to shear and extension over the contraction-expansion area for a Newtonian fluid. The derivation was done and provided by Padding and De of Eindhoven University of Technology [30]. In the derivation the friction with the side walls is neglected, however the friction with the top and bottom is included. Furthermore, the expansion-contraction geometry is designed such that 'pure' elongational flow can be assumed along the center plane.

Kinematics If ε_c is the elongational rate at the centerplane, the tensor gradient $\nabla\mathbf{u}$ at the center plane can be written as:

$$\nabla\mathbf{u} = \begin{bmatrix} \varepsilon_c & 0 & 0 \\ 0 & -\varepsilon_c & 0 \\ 0 & 0 & 0 \end{bmatrix} \text{for } x \in [0, l_c] \tag{B.1}$$

$$\nabla\mathbf{u} = \begin{bmatrix} -\varepsilon_c & 0 & 0 \\ 0 & \varepsilon_c & 0 \\ 0 & 0 & 0 \end{bmatrix} \text{for } x \in [l_c, 2l_c] \tag{B.2}$$

If we define $u_x = u_0$ and $u_y = 0$ at $x = 0$ then we get:

$$u_x = \begin{cases} u_0 + \varepsilon_c x & : x \in [0, l_c] \\ u_0 + \varepsilon_c x\,(2l_c - x) & : x \in [l_c, 2l_c] \end{cases}$$

$$u_y = \begin{cases} -\varepsilon_c y & : x \in [0, l_c] \\ \varepsilon_c y\,(2l_c - x) & : x \in [l_c, 2l_c] \end{cases}$$

Mass Balance The analytical expression for the width of the channel in the contraction-expansion area can be determined by a mass balance. The mass balance states:

$$u_x(x)\, w(x) = c \tag{B.5}$$

where $w(x)$ is the width of the channel as function of x and c a constant. When we substitute Equation B.3 in to Equation B.5 and apply $w(0) = \frac{C}{u_0} = w_u$ as boundary condition we get:

$$w(x) = \begin{cases} \frac{w_u}{1+\frac{\varepsilon_c}{u_0} x} & : x \in [0, l_c] \\ \frac{w_u}{1+\frac{\varepsilon_c}{u_0}(2l_c - x)} & : x \in [l_c, 2l_c] \end{cases}$$

Furthermore if we apply $w(l_c) = \frac{w_u}{1+\frac{\varepsilon_c}{l_c}x} = w_c$ the expression for the elongational rate at the centerplane ε_c becomes:

$$\varepsilon_c = \frac{u_o}{l_c}\left(\frac{w_u}{w_c} - 1\right) \tag{B.7}$$

Full kinematics If Poisseuille flow is assumed in the z-direction then:

$$u_x(z) = u_0\left(1 - \left(\frac{2z}{h}\right)^2\right)\text{for} x < 0 z \in [-\frac{h}{2}, \frac{h}{2}] \tag{B.8}$$

Suppose the Poiseuille profile also exists in the contraction-expansion profile, then:

$$u_x(x,z) = \begin{cases} (u_0 + \varepsilon_c x)\left(1 - \left(\frac{2z}{h}\right)^2\right) & : x \in [0, l_c]\text{and}\nabla\mathbf{u} = 0 \\ (u_0 + \varepsilon_c(2l_c - x))\left(1 - \left(\frac{2z}{h}\right)^2\right) & : x \in [l_c, 2l_c]\text{and}\nabla\mathbf{u} = 0 \end{cases}$$

$$u_y(x,z) = \begin{cases} -\varepsilon_c y\left(1 - \left(\frac{2z}{h}\right)^2\right) & : x \in [0, l_c]\text{and}\nabla\mathbf{u} = 0 \\ \varepsilon_c y\left(1 - \left(\frac{2z}{h}\right)^2\right) & : x \in [l_c, 2l_c]\text{and}\nabla\mathbf{u} = 0 \end{cases}$$

$$u_z(x,z) = 0\text{for } x \in [0, 2l_c]\text{and}\nabla\mathbf{u} = 0 \tag{B.11}$$

From this the tensor gradient $\nabla\mathbf{u}$ is written as:

$$\nabla\mathbf{u} = \begin{bmatrix} 0 & 0 & 0 \\ 0 & 0 & 0 \\ -u_0\frac{8z}{h^2} & 0 & 0 \end{bmatrix} \text{for } x < 0, x > 2l_c \tag{B.12}$$

$$\nabla\mathbf{u} = \begin{bmatrix} \varepsilon_c\left(1 - \left(\frac{2z}{h}\right)^2\right) & 0 & 0 \\ 0 & -\varepsilon_c\left(1 - \left(\frac{2z}{h}\right)^2\right) & 0 \\ -(u_0 + \varepsilon_c x)\frac{8z}{h^2} & \varepsilon_c y\frac{8z}{h^2} & 0 \end{bmatrix} \text{for } x \in [0, l_c] \tag{B.13}$$

$$\nabla\mathbf{u} = \begin{bmatrix} -\varepsilon_c\left(1 - \left(\frac{2z}{h}\right)^2\right) & 0 & 0 \\ 0 & \varepsilon_c\left(1 - \left(\frac{2z}{h}\right)^2\right) & 0 \\ -(u_0 + \varepsilon_c(2l_c - x))\frac{8z}{h^2} & -\varepsilon_c y\frac{8z}{h^2} & 0 \end{bmatrix} \text{for } x \in [l_c, 2l_c] \tag{B.14}$$

Deformation leads to a stress in the fluid. For a Newtonian fluid, the non-zero stress components correspond to the non-zero $\nabla\mathbf{u}$ components, therefore the stress tensor is symmetric:

$$\tau = \begin{bmatrix} \tau_{xx} & 0 & \tau_{xz} \\ 0 & \tau_{yy} & \tau_{yz} \\ \tau_{xz} & \tau_{yz} & 0 \end{bmatrix} \tag{B.15}$$

The tensor can be interpreted as a summation of the elongational and shear stress:

$$\tau = \tau_{\mathbf{e}} + \tau_{\mathbf{s}} = \begin{bmatrix} \tau_{xx} & 0 & 0 \\ 0 & \tau_{yy} & 0 \\ 0 & 0 & 0 \end{bmatrix} + \begin{bmatrix} 0 & 0 & \tau_{xz} \\ 0 & 0 & \tau_{yz} \\ \tau_{xz} & \tau_{yz} & 0 \end{bmatrix} \tag{B.16}$$

The elongational viscosity is then defined as:

$$\eta_E = \frac{\tau_{xx} - \tau_{yy}}{\varepsilon} = \frac{\tau_{xx}(x,z) - \tau_{yy}(x,z)}{\varepsilon_c\left(1 - \left(\frac{2z}{h}\right)^2\right)} \tag{B.17}$$

And the shear viscosity is defined as:

$$\eta_s = \frac{\tau_{xz}}{-\frac{\partial u_x}{\partial z}} = \frac{\tau_{yz}}{-\frac{\partial u_y}{\partial z}} \tag{B.18}$$

Note that the device will always measure an average elongational viscosity because of extensional rate from 0 to ε_c are present.

Stress tensor for a Newtonian fluid The stress tensor is defined as (See Navier-Stokes):

$$\tau = \eta\left[\nabla\mathbf{u} + (\nabla\mathbf{u})^T\right] = \begin{bmatrix} 2\varepsilon_c\left(1-\left(\frac{2z}{h}\right)^2\right) & 0 & -\left(u_0+\varepsilon_c x\right)\frac{8z}{h^2} \\ 0 & -2\varepsilon_c\left(1-\left(\frac{2z}{h}\right)^2\right) & \varepsilon_c y\frac{8z}{h^2} \\ -\left(u_0+\varepsilon_c x\right)\frac{8z}{h^2} & \varepsilon_c y\frac{8z}{h^2} & 0 \end{bmatrix} \text{for } x \in [0, l_c] \tag{B.19}$$

$$\tau = \eta\left[\nabla\mathbf{u} + (\nabla\mathbf{u})^T\right] = \begin{bmatrix} -2\varepsilon_c\left(1-\left(\frac{2z}{h}\right)^2\right) & 0 & -\left(u_0+\varepsilon_c\left(2l_c-x\right)\right)\frac{8z}{h^2} \\ 0 & 2\varepsilon_c\left(1-\left(\frac{2z}{h}\right)^2\right) & -\varepsilon_c y\frac{8z}{h^2} \\ -\left(u_0+\varepsilon_c\left(2l_c-x\right)\right)\frac{8z}{h^2} & -\varepsilon_c y\frac{8z}{h^2} & 0 \end{bmatrix} \text{for } x \in [l_c, 2l_c] \tag{B.20}$$

Dissipation of energy per unit volume

$$\tau : \nabla\mathbf{u} = \underbrace{4\eta\varepsilon_c^2\left(1-\left(\frac{2z}{h}\right)^2\right)^2}_{\text{extensional flow dissipation}} \underbrace{+\eta\left(u_0+\varepsilon_c x\right)^2\left(\frac{8z}{h^2}\right)^2 + \eta\varepsilon_c^2 y^2\left(\frac{8z}{h^2}\right)^2}_{\text{shear flow dissipation}} \text{for } x \in [0, l_c] \tag{B.21}$$

Total energy dissipation due to extensional flow The total energy dissipated in the expansion-contraction can be defined as:

$$E = E^E + E^S = Q\Delta P = \int_V \tau : \nabla\mathbf{u}\, dV \tag{B.22}$$

Since the expansion-contraction geometry is symmetric the total dissipated energy due to extensional flow can be written as:

$$E^E = 2\int_0^{l_c}\int_{-\frac{1}{2}w(x)}^{\frac{1}{2}w(x)} dxdy \int_{-\frac{h}{2}}^{\frac{h}{2}} 4\eta\varepsilon_c^2\left(1-\left(\frac{2z}{h}\right)^2\right)^2 dz \tag{B.23}$$

Since $\int_{-\frac{1}{2}w(x)}^{\frac{1}{2}w(x)}$ is equal to Equation B.6 this equation becomes:

$$E^E = 8\eta\varepsilon_c^2\int_0^{l_c}\frac{w_u}{1+\left(\frac{w_u}{w_c}-1\right)\frac{x}{l_c}} dxdy \int_{-\frac{h}{2}}^{\frac{h}{2}}\left(1-\left(\frac{2z}{h}\right)^2\right)^2 dz \tag{B.24}$$

$$E^E = 8\eta\varepsilon_c^2\int_0^{l_c}\frac{w_u}{1+\left(\frac{w_u}{w_c}-1\right)\frac{x}{l_c}} dxdy \int_{-\frac{h}{2}}^{\frac{h}{2}}\left(1-2\left(\frac{2z}{h}\right)^2+\left(\frac{2z}{h}\right)^4\right) dz \tag{B.25}$$

$$E^E = 8\eta\varepsilon_c^2\left[w_u \ln\left(1+\left(\frac{w_u}{wc}-1\right)\frac{x}{l_c}\right)\frac{l_c}{\frac{w_u}{wc}-1}\right]_0^{l_c}\left[z-\frac{8z^3}{3h^2}+\frac{16z^5}{h^4}\right]_{-\frac{h}{2}}^{\frac{h}{2}} \tag{B.26}$$

$$E^E = 8\eta\varepsilon_c^2 w_u \ln\left(\frac{1+\left(\frac{w_u}{wc}-1\right)}{1}\right)2h\left(\frac{1}{2}-\frac{8}{3}\left(\frac{1}{2}\right)^3+\frac{16}{5}\left(\frac{1}{2}\right)^5\right) \tag{B.27}$$

Substitution of EquationB.7 result in:

$$E^E = 8\eta\left(\frac{u_o}{l_c}\left(\frac{w_u}{w_c}-1\right)\right)^2\frac{2w_u l_c h}{\frac{w_u}{w_c}-1} ln\left(\frac{w_u}{w_c}\right)\left(\frac{1}{2}-\frac{1}{3}+\frac{1}{10}\right) \tag{B.28}$$

$$E^E = 16\eta u_o^2\frac{w_u h}{l_c}\left(\frac{w_u}{w_c}-1\right) ln\left(\frac{w_u}{w_c}\right)\frac{8}{30} \tag{B.29}$$

Total flow rate The total flow rate through the contraction-expansion can be defined as:

$$Q = \int_{-\frac{1}{2}w_u}^{\frac{1}{2}w_u} dy \int_{-\frac{h}{2}}^{\frac{h}{2}} u_0 \left(1 - \left(\frac{2z}{h}\right)^2\right) dz \tag{B.30}$$

$$Q = W_u u_0 \left[z - \frac{4}{3}\frac{z^3}{h^2}\right]_{-\frac{h}{2}}^{\frac{h}{2}} = \frac{2}{3} h w_u u_0 \tag{B.31}$$

Pressure drop due to extensional flow Dividing Equation B.29 by the flow rate Q and Substituting Equation B.31 into Equation B.29 gives:

$$\Delta P_c^E = \frac{E^E}{Q} = 16\frac{8}{30}\frac{3}{2}\eta\frac{1}{l_c}u_0\left(\frac{w_u}{w_c} - 1\right) ln\left(\frac{w_u}{w_c}\right) \tag{B.32}$$

Substitution of Equation B.7 gives:

$$\Delta P_c^E = 6.4\eta\varepsilon_c ln\left(\frac{w_u}{w_c}\right) \tag{B.33}$$

Using Equation B.31 Equation B.29 can also be written in terms of flow rate:

$$\Delta P_c^E = 16\frac{8}{30}\frac{3}{2}\eta\frac{1}{l_c}\frac{Q}{\frac{2}{3}w_u h}\left(\frac{w_u}{w_c} - 1\right) ln\left(\frac{w_u}{w_c}\right) \tag{B.34}$$

$$\Delta P_c^E = 9.6\eta\frac{Q}{h l_c}\left(\frac{1}{w_c} - \frac{1}{w_u}\right) ln\left(\frac{w_u}{w_c}\right) \tag{B.35}$$

Dissipation of energy due to shear flow

$$E^S = 2\int_0^{l_c} dx \int_{-\frac{1}{2}w(x)}^{\frac{1}{2}w(x)} dy \int_{-\frac{h}{2}}^{\frac{h}{2}} dz \left[\eta\left(u_0 + \varepsilon_c x\right)^2\left(\frac{8z}{h^2}\right)^2 + \eta\varepsilon_c^2 y^2\left(\frac{8z}{h^2}\right)^2\right] \tag{B.36}$$

$$E^S = 2\eta\left(\frac{8}{h^2}\right)^2\int_0^{l_c} w(x)\left(u_0 + \varepsilon_c x\right)^2 dx \int_{-\frac{h}{2}}^{\frac{h}{2}} z^2 dz + 2\eta\left(\frac{8}{h^2}\right)\varepsilon_c^2\int_0^{l_c}\left[\int_{-\frac{1}{2}w(x)}^{\frac{1}{2}w(x)} y^2 dy\right] dx \int_{-\frac{h}{2}}^{\frac{h}{2}} z^2 dz \tag{B.37}$$

$$E^S = 2\eta\left(\frac{8}{h^2}\right)^2\int_0^{l_c}\frac{w_u}{1 + \left(\frac{w_u}{w_c} - 1\right)\frac{x}{l_c}} u_0^2\left[1 + \left(\frac{w_u}{w_c} - 1\right)\frac{x}{l_c}\right]^2 dx \int_{-\frac{h}{2}}^{\frac{h}{2}} z^2 dz + 2\eta\left(\frac{8}{h^2}\right)\varepsilon_c^2\int_0^{l_c}\left[\frac{1}{3}y^3\right]_{-\frac{1}{2}w(x)}^{\frac{1}{2}w(x)} dx \int_{-\frac{h}{2}}^{\frac{h}{2}} z^2 dz \tag{B.38}$$

$$E^S = 2\eta\left(\frac{8}{h^2}\right)^2 w_u u_0^2\int_0^{l_c}\left[1 + \left(\frac{w_u}{w_c} - 1\right)\frac{x}{l_c}\right] dx \left[\frac{1}{3}z^3\right]_{-\frac{h}{2}}^{\frac{h}{2}} + 2\eta\left(\frac{8}{h^2}\right)\varepsilon_c^2\frac{1}{12}\int_0^{l_c} w(x)^3 dx \left[\frac{1}{3}z^3\right]_{-\frac{h}{2}}^{\frac{h}{2}} \tag{B.39}$$

$$E^S = 2\eta\left(\frac{8}{h^2}\right)^2 w_u u_0^2\left[x + \frac{1}{2}\left(\frac{w_u}{w_c} - 1\right)\frac{x^2}{l_c}\right]_0^{l_c}\frac{1}{12}h^3 + 2\eta\left(\frac{8}{h^2}\right)^2\varepsilon_c^2\frac{1}{12}\int_0^{l_c}\left[\frac{w_u}{1 + \left(\frac{w_u}{w_c} - 1\right)\frac{x}{l_c}}\right] dx \frac{1}{12}h^3 \tag{B.40}$$

$$E^S = 2\eta\left(\frac{8}{h^2}\right)^2 w_u u_0^2 l_c\left[1 + \frac{1}{2}\left(\frac{w_u}{w_c} - 1\right)\right]\frac{1}{12}h^3 + 2\eta\left(\frac{8}{h^2}\right)^2 u_0^2\frac{1}{l_c^2}\left(\frac{w_u}{w_c} - 1\right)^2\frac{1}{12}w_u^3\left[-\frac{1}{2\left(\frac{w_u}{w_c} - 1\right)\frac{1}{l_c}}\frac{1}{\left[1 + \left(\frac{w_u}{w_c} - 1\right)\frac{x}{l_c}\right]^2}\right]_0^{l_c}\frac{1}{12}h^3 \tag{B.41}$$

$$E^S = 2\eta\left(\frac{8}{h^2}\right)^2 u_0^2\frac{w_u l_c h^3}{12}\frac{1}{2}\left(1+\frac{w_u}{w_c}\right)+2\eta\left(\frac{8}{h^2}\right)^2 u_0^2\frac{w_u^3 h^3}{12 l_c}\frac{1}{12}\frac{1}{2}\left(\frac{w_u}{w_c}-1\right)\left[1-\frac{1}{\left[1+\left(\frac{w_u}{w_c}-1\right)\right]^2}\right] \tag{B.42}$$

$$E^S = \frac{8^2\times 2}{12\times 2}\eta u_0^2\frac{w_u l_c}{h}\left(\frac{w_u}{w_c}+1\right)+\frac{8^2\times 2}{12^2\times 2}\eta u_0^2\frac{w_u^3}{h l_c}\left(\frac{w_u}{w_c}-1\right)\left[1-\left(\frac{w_c}{w_u}\right)^2\right] \tag{B.43}$$

$$E^S = \frac{16}{3}\eta u_0^2\frac{w_u l_c}{h}\left(\frac{w_u}{w_c}+1\right)+\frac{4}{9}\eta u_0^2\frac{w_u^3}{h l_c}\left(\frac{w_u}{w_c}-1\right)\left(1-\frac{w_c}{w_u}\right)\left(1+\frac{w_c}{w_u}\right) \tag{B.44}$$

Pressure drop due to shear in terms of flow rate

$$\Delta P_c^S = \frac{E^S}{Q} = \frac{16}{3}\eta\frac{1}{Q}\left(\frac{Q}{\frac{2}{3}w_u h}\right)^2\frac{w_u l_c}{h}\left(\frac{w_u}{w_c}+1\right)+\frac{4}{9}\eta\frac{1}{Q}\left(\frac{Q}{\frac{2}{3}w_u h}\right)^2\frac{w_u^3}{h l_c}\left(\frac{w_u}{w_c}-1\right)\left(1-\frac{w_c}{w_u}\right)\left(1+\frac{w_c}{w_u}\right) \tag{B.45}$$

$$\Delta P_c^S = \frac{E^S}{Q} = \frac{4}{3}\eta Q\frac{l_c}{w_u h^3}\left(\frac{w_u}{w_c}+1\right)+\eta Q\frac{w_u}{l_c h^3}\left(\frac{w_u}{w_c}-1\right)\left(1-\frac{w_c}{w_u}\right)\left(1+\frac{w_c}{w_u}\right) \tag{B.46}$$

$$\Delta P_c^S = \frac{E^S}{Q} = \frac{4}{3}\eta Q\frac{l_c}{h^3}\left(\frac{1}{w_c}+\frac{1}{w_u}\right)+\eta Q\frac{w_u}{l_c h^3}\left(\frac{1}{w_c}-\frac{1}{w_u}\right)\left(w_u^2-w_c^2\right) \tag{B.47}$$

In summary:

$$\Delta P_c^E = \eta Q\frac{1}{l_c h w_u}\left[\frac{48}{5}\left(\frac{w_u}{w_c}-1\right)ln\left(\frac{w_u}{w_c}\right)\right] \tag{B.48}$$

$$\Delta P_c^S = \eta Q\frac{1}{l_c h w_u}\left[\frac{4}{3}\left(\frac{l_c}{h}\right)^2\left(\frac{w_u}{w_c}+1\right)+\left(\frac{w_u}{w_c}-1\right)\left(\frac{w_u}{h}\right)^2\left(1-\left(\frac{w_c}{w_u}\right)^2\right)\right] \tag{B.49}$$

Example If $w_u = 3.314mm$, $w_c = 0.400mm$, $l_c = 0.800mm$ and $h = 0.1965mm$ then Equations B.48 and B.49 become

$$\Delta P_c^E = \eta Q\frac{1}{l_c h w_u}\left[147.9\right] \tag{B.50}$$

$$\Delta P_c^S = \eta Q\frac{1}{l_c h w_u}\left[205.2+2041.9\right] \tag{B.51}$$

C

CALIBRATION FLUID DATA

Fluid Name	**Fluid Type**	**Shear Viscosity** [**mPas**]	**Density** [**kg**/**m**^{3}]	**Temperature** [**C**]
N15	$32-68w\%\ H_2O$−Glycerol	15.8	1175	25
N25	Fluid 25	26	800	60
N50	Fluid 50	49.1	960	25
N75	Olive Oil	71.6	910	23
N100	Fluid 100	97	960	25

Table C.1: The different Newtonian fluids that were used for the calibration of the e-VROC cells.

C.1. SHEAR RHEOMETER DATA

Shear viscosity sweep of N15

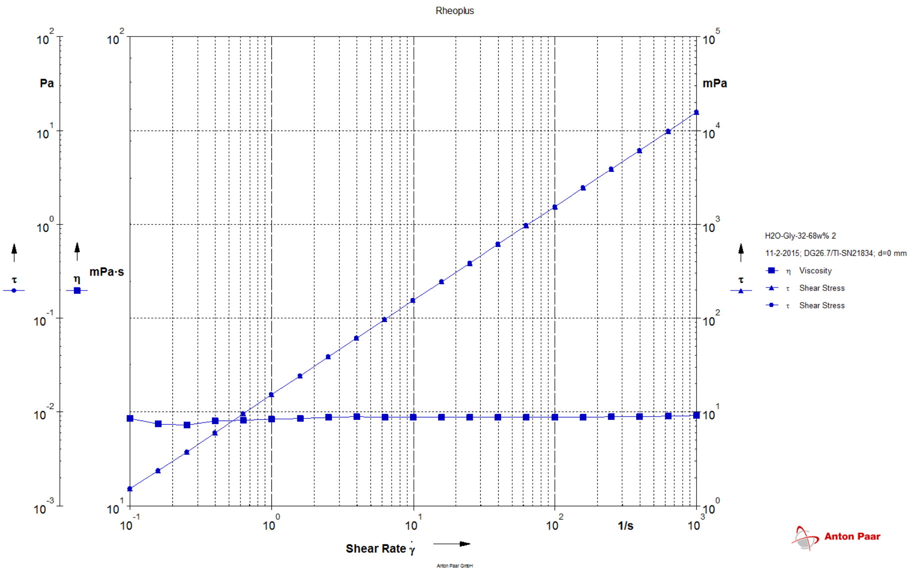

Figure C.1: Viscosity of N15 for different shear velocities.

Shear viscosity sweep of N25

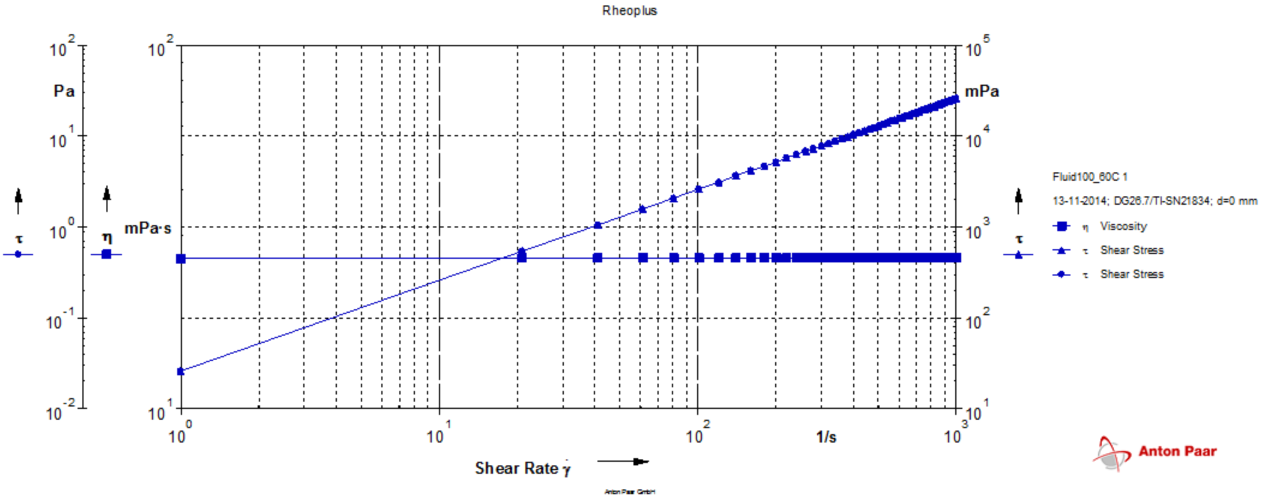

Figure C.2: Viscosity of N25 for different shear velocities.

Shear viscosity sweep of N50

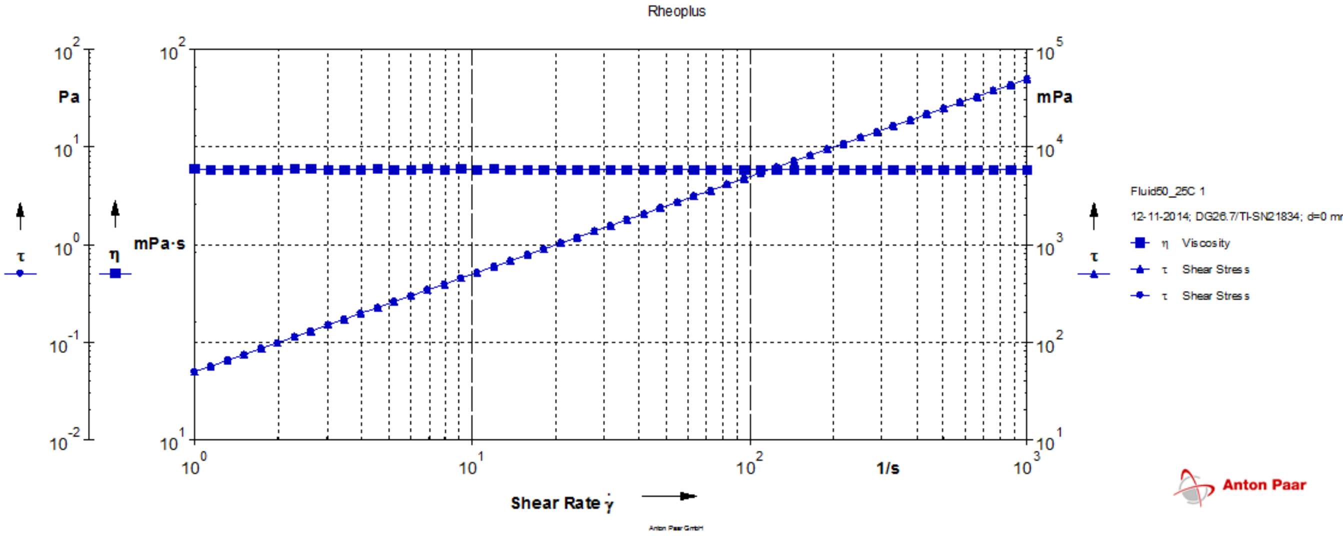

Figure C.3: Viscosity of N50 for different shear velocities.

Shear viscosity sweep of N75

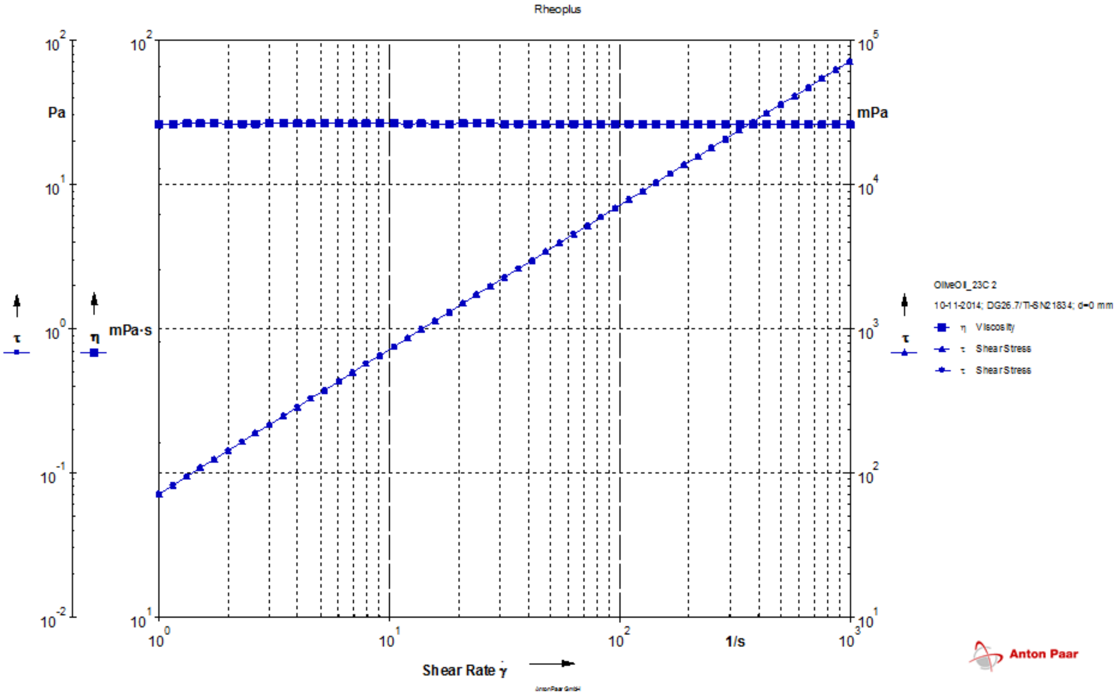

Figure C.4: Viscosity of N75 for different shear velocities.

Shear viscosity sweep of N100

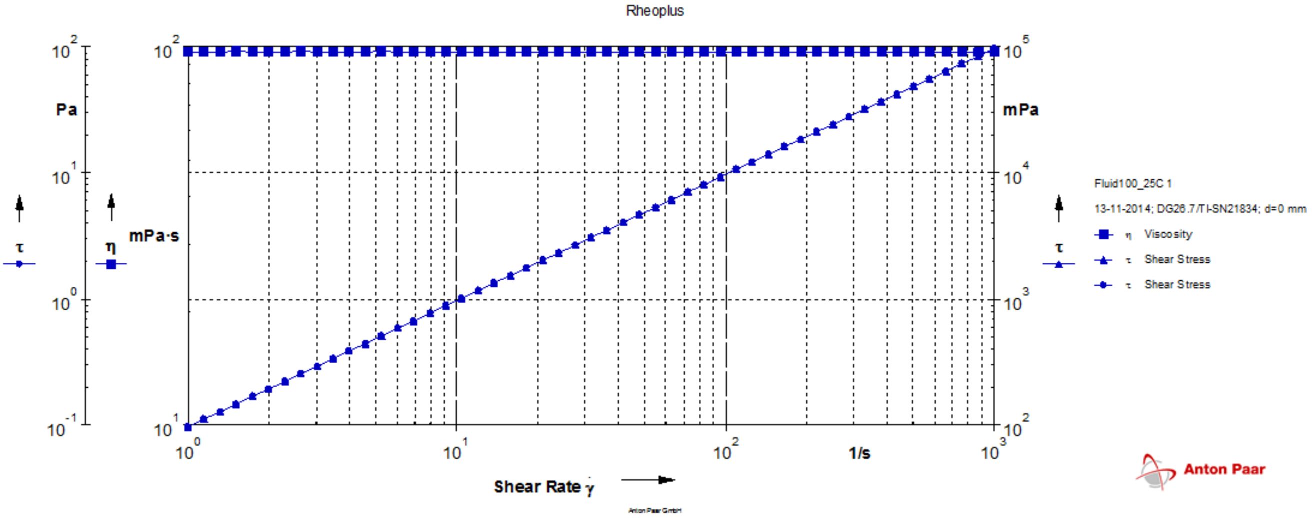

Figure C.5: Viscosity of N100 for different shear velocities.

C.2. E-VROC MEASURED DATA

Pressure profiles of N25

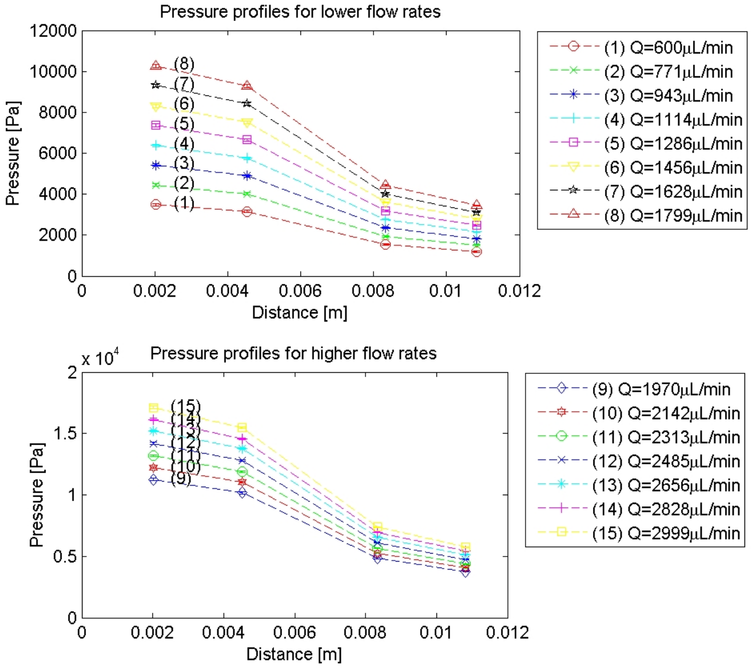

Figure C.6: Measured pressures within the e-VROC cell for N25 for different flow rates.

Pressure profiles of N75

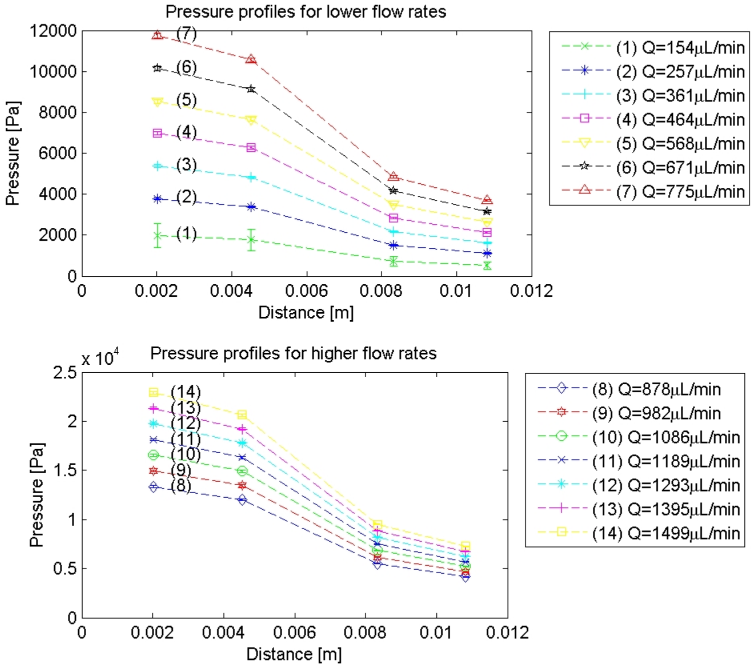

Figure C.7: Measured pressures within the e-VROC cell for N75 for different flow rates.

Pressure profiles of N100

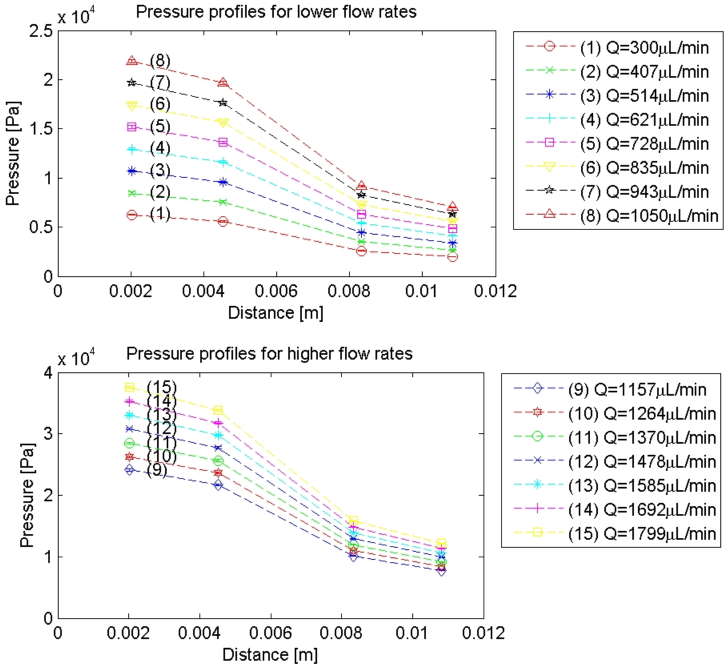

Figure C.8: Measured pressures within the e-VROC cell for N100 for different flow rates.

C.3. PRESSURE GRADIENTS AS FUNCTION OF FLOW RATE

Pressure gradients plot of N25

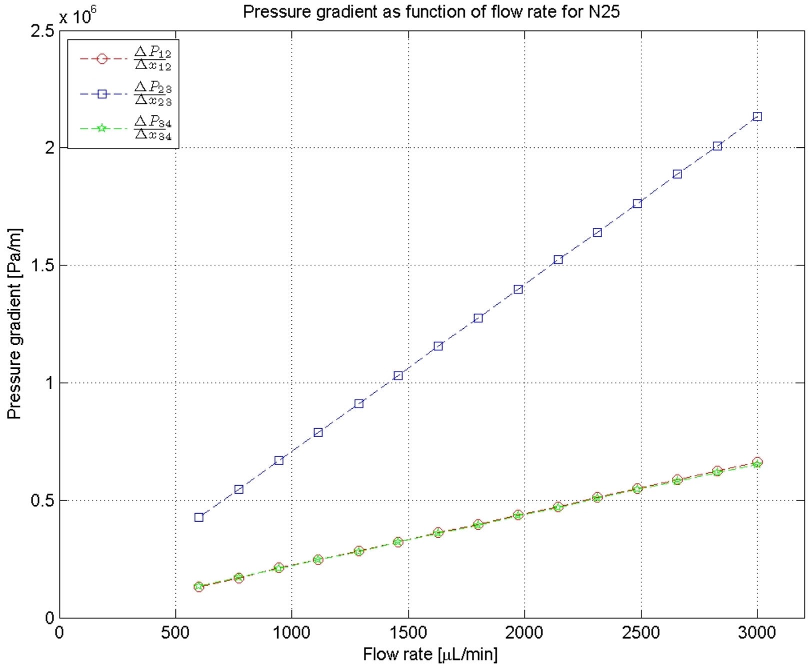

Figure C.9: Pressure gradients plot for N25.

Pressure gradients plot of N75

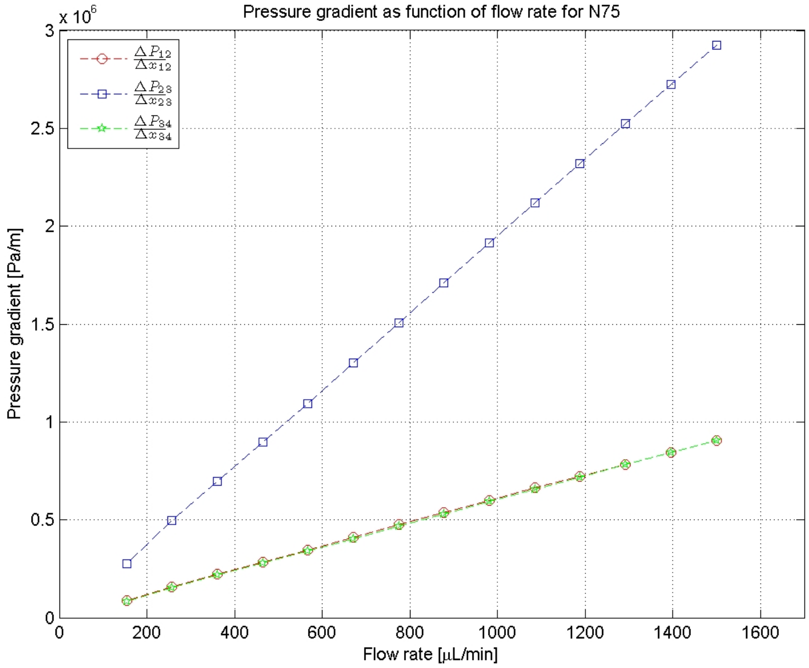

Figure C.10: Pressure gradients plot for N75.

Pressure gradients plot of N100

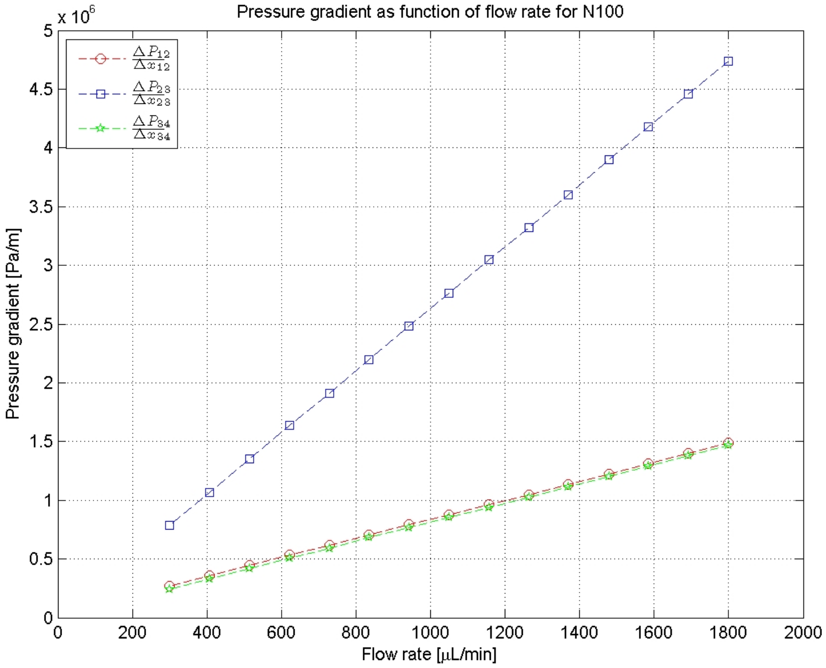

Figure C.11: Pressure gradients plot for N100.

C.4. E-VROC SHEAR VISCOSITY

Shear viscosity of N25

Flow rate [μL/min]	$\mu_{\mathbf{sh12}}$ [cP]	$\mu_{\mathbf{sh34}}$ [cP]
600	25.9	26.5
771	26.0	26.3
943	26.6	26.3
1114	26.2	26.3
1286	26.2	26.0
1456	26.2	26.2
1628	26.4	26.2
1799	26.3	26.1
1970	26.3	26.3
2142	26.1	25.9
2313	26.3	26.1
2485	26.3	26.2
2656	26.3	26.0
2828	26.2	25.9
2999	26.2	25.9

Table C.2: Shear viscosities determined from the e-VROC data for N25.

Shear viscosity of N75

Flow rate ($\mu L/min$)	$\eta_{sh,12}$ (cP)	$\eta_{sh,34}$ (cP)
153.6	66.4	64.7
257.1	72.7	71.5
360.7	72.8	71.6
464.3	72.7	71.4
567.9	72.5	71.3
671.4	72.7	71.3
775	72.7	71.4
878.6	72.5	71.5
982.1	72.5	71.9
1085.7	72.4	71.7
1189.3	72.0	71.8
1292.9	71.9	71.7
1396.4	71.8	71.7
1500	71.6	71.5

Table C.3: Shear viscosities determined from the e-VROC data for N75.

Shear viscosity of N100

Flow rate ($\mu L/min$)	$\eta_{sh,12}$ (cP)	$\eta_{sh,34}$ **(cP)**
300	105.9	96.9
407.1	104.2	96.2
514.3	103.1	96.4
621.4	101.9	97.0
728.6	100.9	96.4
835.7	100.3	96.9
942.9	99.6	96.6
1050	98.9	96.5
1157.1	98.7	96.4
1264.3	98.2	96.3
1371.4	98.1	96.2
1478.6	98.3	96.7
1585.7	98.4	96.8
1692.9	98.3	96.5
1800	98.1	96.7

Table C.4: Shear viscosities determined from the e-VROC data for N100.

C.5. Extensional viscosity, Trouton and Reynold numbers

Extensional viscosity, Trouton and Reynold numbers of N25

Flow rate ($\mu L/min$	η_e **(cP)**	**Tr**	**Re**
600	2078	79.9	2.2
771.4	2069	79.6	2.8
942.9	2053	79.0	3.4
1114.3	2056	79.1	4.0
1285.7	2065	79.4	4.7
1457.1	2054	79.0	5.3
1628.6	2061	79.3	5.9
1800	2061	79.3	6.5
1971.4	2061	79.3	7.1
2142.9	2076	79.8	7.8
2314.3	2060	79.2	8.4
2485.7	2065	79.4	9.0
2657.1	2073	79.7	9.6
2828.6	2071	79.7	10.3
3000	2075	79.8	10.9

Table C.5: The extensional viscosities, the corresponding Trouton ratio and Reynolds number for N25 at the measured flow rates

Extensional viscosity, Trouton and Reynold numbers of N75

Flow rate ($\mu L/min$	η_e **(cP)**	**Tr**	**Re**
153.6	5233	73.1	0.062
257.1	5610	78.4	0.19
360.7	5608	78.3	0.32
464.3	5619	78.5	0.45
567.9	5592	78.1	0.58
671.4	5624	78.5	0.71
775	5641	78.8	0.84
878.6	5656	79.0	0.98
982.1	5669	79.2	1.1
1085.7	5684	79.4	1.2
1189.3	5679	79.3	1.4
1292.9	5690	79.5	1.5
1396.4	5688	79.4	1.6
1500	5682	79.4	1.7

Table C.6: The extensional viscosities, the corresponding Trouton ratio and Reynolds number for N75 at the measured flow rates

Extensional viscosity, Trouton and Reynold numbers of N100

Flow rate ($\mu L/min$	η_e **(cP)**	**Tr**	**Re**
300	7518	77.5	0.29
407.1	7537	77.7	0.40
514.3	7573	78.1	0.50
621.4	7600	78.4	0.60
728.6	7604	78.4	0.71
835.7	7628	78.6	0.81
942.9	7639	78.8	0.92
1050	7646	78.8	1.0
1157.1	7664	79.0	1.1
1264.3	7644	78.8	1.2
1371.4	7644	78.8	1.3
1478.6	7663	79.0	1.4
1585.7	7661	79.0	1.5
1692.9	7657	78.9	1.6
1800	7659	78.9	1.7

Table C.7: The extensional viscosities, the corresponding Trouton ratio and Reynolds number for N100 at the measured flow rates

D

POLYMER SHEAR RHEOMETRY

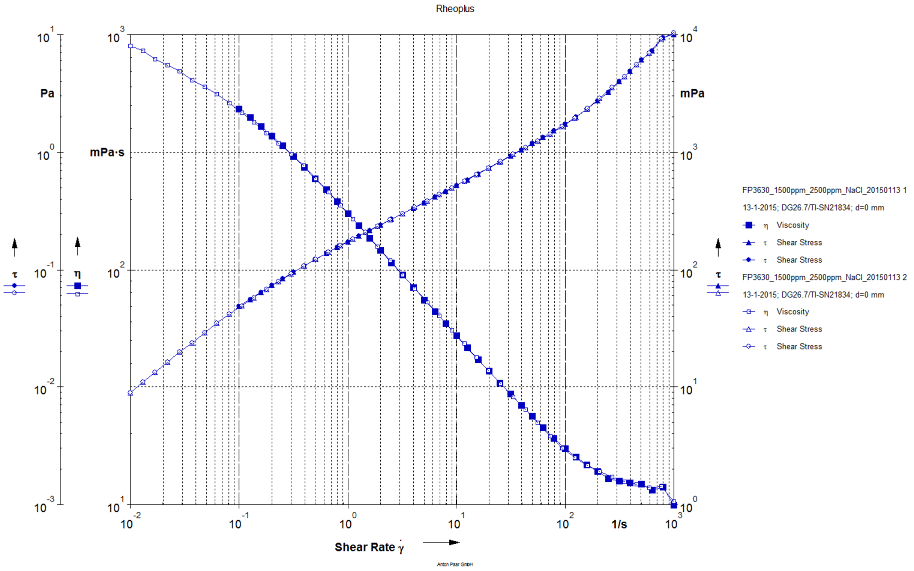

Figure D.1: Two shear viscosity scans of FP2500 at different shear rates.

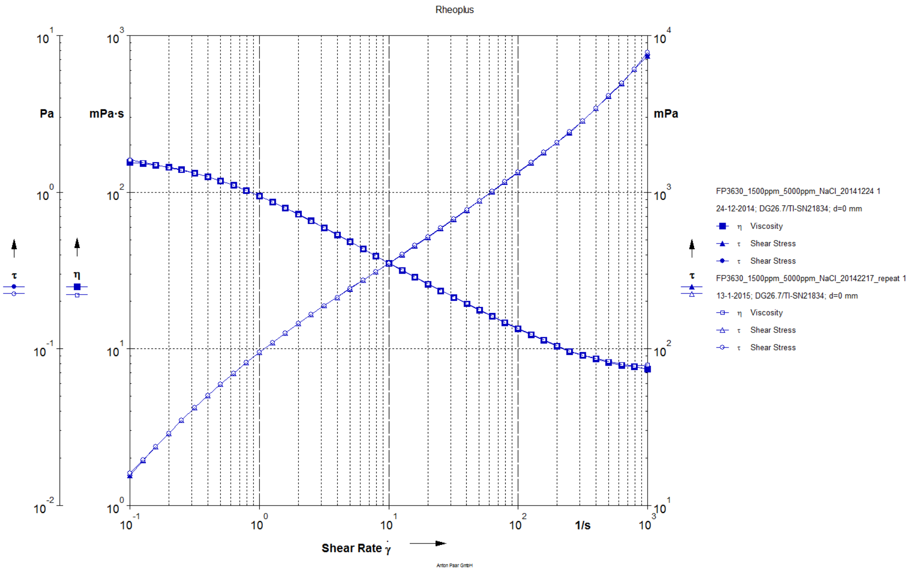

Figure D.2: Two shear viscosity scans of FP5000 at different shear rates.

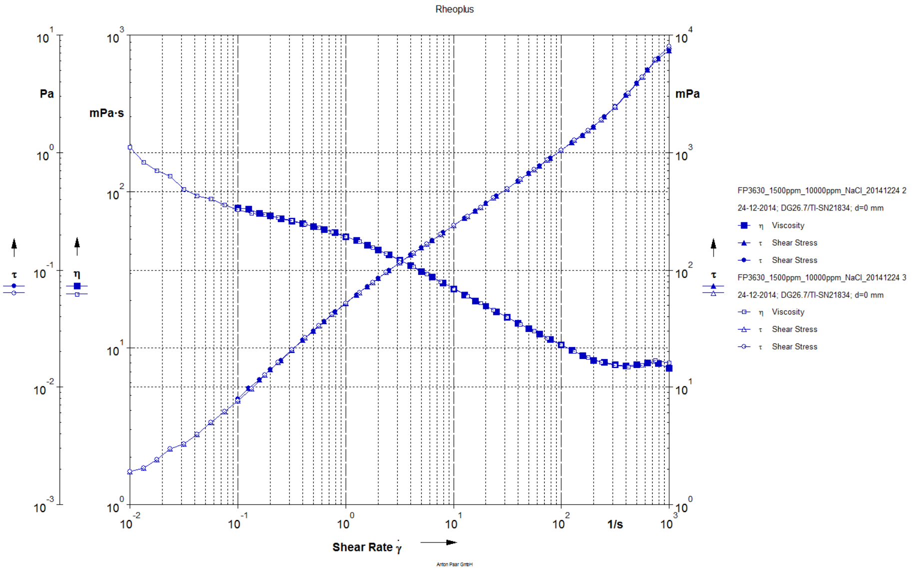

Figure D.3: Two shear viscosity scans of FP10000 at different shear rates.

E

NOISE ANALYSIS OF POLYMER TIME SIGNAL

Figure E.1 shows the single-sided amplitude spectrum of the pressure as function of time for FP5000 measured by the first pressure transducer at a flow rate of 300 $\mu L/min$. If there is a noise of a certain frequency present in the time signal, the single-sided amplitude spectrum shows a peak at the frequency of the noise. However, Figure E.1 only shows a peak at a frequency of zero. This indicates that there is no dominant oscillation present in the time signal, hence the noise appears to be random. However, since the sampling frequency is 5Hz, it very hard to detect any noise with a higher frequency. Therefore, there could still be frequent noise on the time signal however its frequency cannot be quantified.

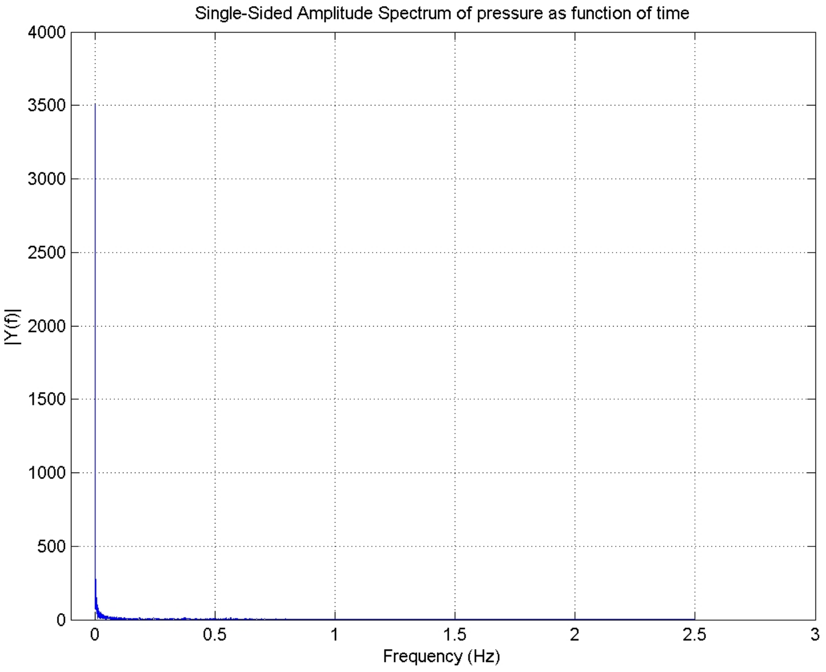

Figure E.1: single-sided amplitude spectrum of the pressure as function of time for FP5000 measured by the first pressure transducer at a flow rate of 300 $\mu L/min$.

F

TIME SIGNAL RESPONSE LAPONITE

To test if the elastic behaviour of the FP3630S was causing the high noise content of the time-pressure signal, a Laponite solution was flown through the e-VROC cell. Laponite is an artificial clay and highly shear thinning. Laponite ($Na^{+0.7}\left[\left(Si_8Mg_{5.5}Li_{0.3}\right)O_{20}\left(OH\right)_4\right]^{-0.7}$) consists of nano-disks which are positively charged at the sides and negatively charged at the top and bottom. Because of this property the disks will form a house of cards like structure (Figure F.1). When the fluid is deformed the structure is (partial) destroyed. As a result of this structure demolition, Laponite has no memory regarding deformation history, thus completely inelastic. Although it is a very different kind of system compared to FLOPAAM, it is a perfect fluid to test the hypothesis that the elasticity of FLOPAAM might causes the high noise content in the time-pressure signal.

Figure F.2 shows the measured pressures over time in the e-VROC cells for a Laponite solution. Although a slightly higher noise content is observed as compared to Newtonian fluids, 90% of the measured pressures is within 200Pa of the measured mean, which is within the measurement precision of the MEMS tranducers. From this it can be concluded that the high noise content of the FP3630S samples is likely not due to their shear thinning behaviour but should probably be attributed to elasticity.

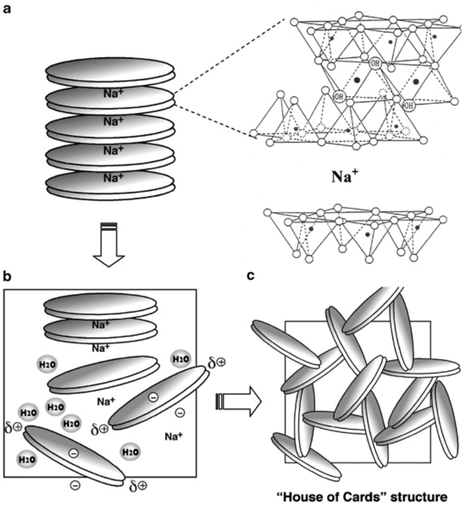

Figure F.1: The morphology and structure building of Laponite [43].

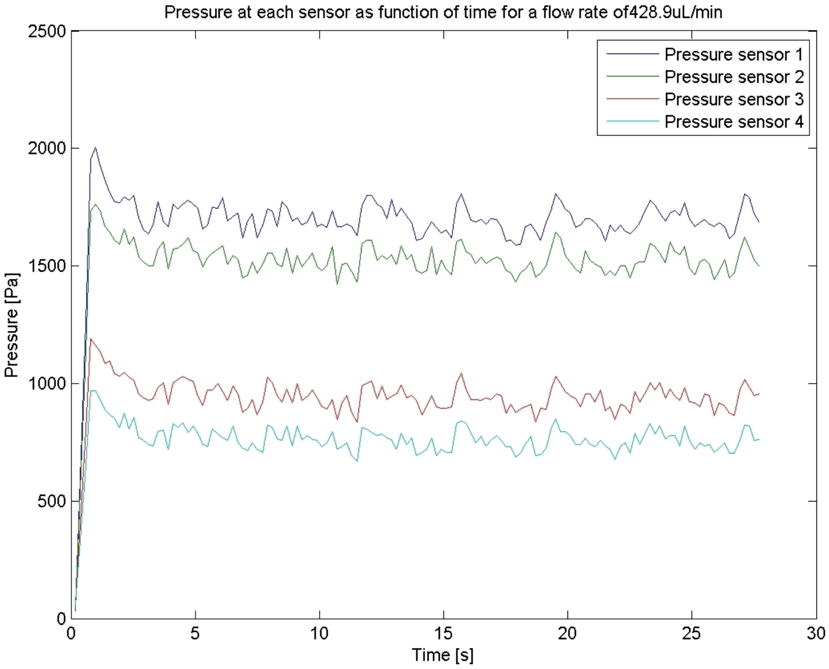

Figure F.2: Pressure at each pressure sensor as function of time for a flow rate of 428.9 $\mu L/min$ for a Laponite solution.

G

CORE ANALYSIS OF BOISE AND BEREA SANDSTONE

In this research, a Boise sandstone core was used in the pore network modelling. A micro-CT image was made to extract the properties of the voxel space of the core.

Before properties can be extracted from the micro-CT image, a difference between void space and rock has to be made. The micro-CT provides an gray-scale image and can be visualized in AVIZO. Darker colors indicate higher density material, whereas light colors indicate low density material. Therefore a difference between void space and rock can be made based on the histogram of grey colors (Figure G.1). Two large peaks are observed, the left peak indicating pore space and the right peak indicting rock. The boundary between rock and void is chosen at the minimum be between these peak. Everything to the left of the boundary is considered void space and everything to the right of this boundary is considered to be rock. But before the micro-CT images can be used in any other procedures it needs to be watersheded first.

Besides rock and void there exists a third phase, namely the surrounding space around the sample, which has a very low density density and is therefore currently considered as void space. However, we do not want the fluid to flow outside the sample, therefore this open space around the rock sample has to be set to be impermeable (hence as rock). This is the so-called watershedding.

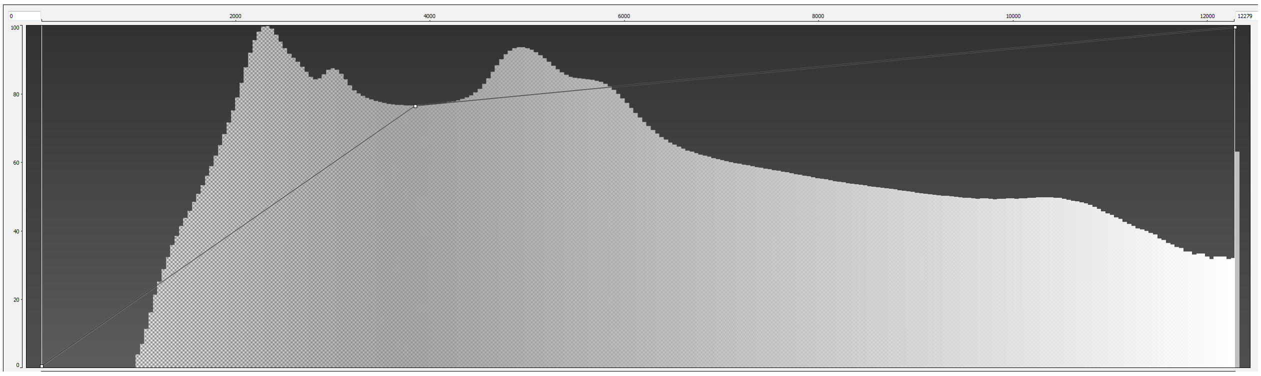

Figure G.1: Histogram of the color scale of the Boise sandstone sample.

G.1. PORE NETWORK EXTRACTION

An algorithm to extract the geometry of the pore space from voxel images, was developed by Hu Dong [39]. This so-called maximum ball algorithm determines the radius of the maximum inscribes sphere that touches the pore walls. From the size of these maximum balls it is determined with part of the void space represents pore bodies or pore throats.

A clustering algorithm groups the maximum balls into pore bodies and pore throats. The cluster algorithm allows the maximum ball ('parent') to absorb its neighbouring balls within a certain radius from its center (Figure G.2). If a ball is absorbed it will be mark as an 'child' of the principal ('parent') ball. By doing this a family tree is formed. In the algorithm the common ancestor of each cluster is defined a pore. When a maximum ball is connected to two cluster (occurs in two family trees) its is defined as a throat (Figure G.3).

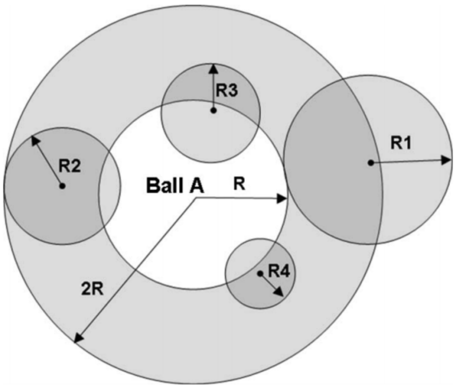

Figure G.2: Schematic of single cluster of principal maximum ball and neighbouring balls [39].

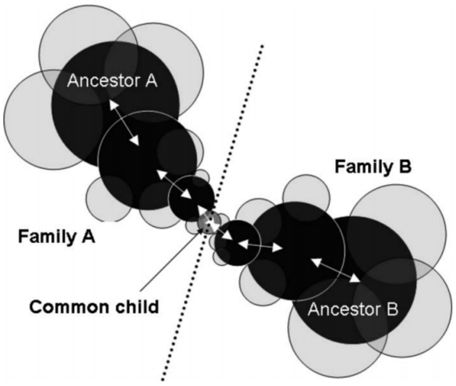

Figure G.3: Schematic of two family trees. Ancestor A and B defined as pore and the common child defined as throat [39].

G.1.1. PORE GEOMETRY

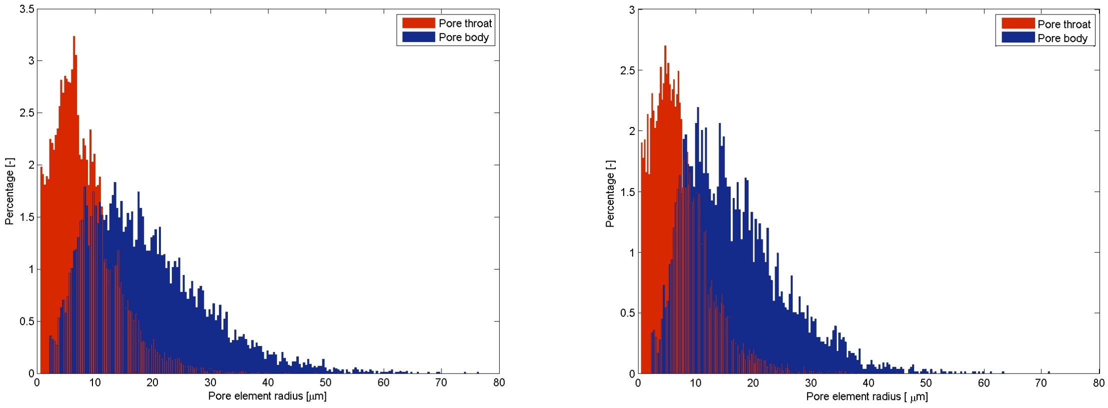

(a) Boise

(b) Berea

Figure G.4: Pore body and throat radius distribution for the Boise and Berea sandstone.

G.1.2. COORDINATION NUMBER

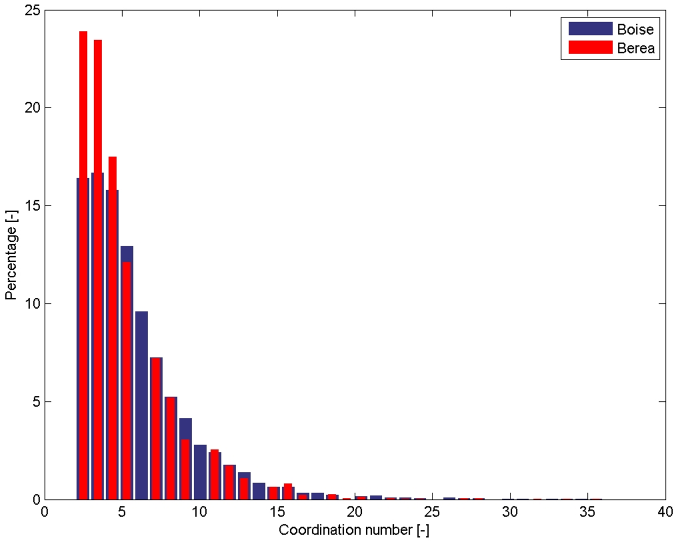

Figure G.5: Coordination number distribution for the Boise sandstone.

H

MOMENTS OF PROBABILITY DENSITY FUNCTIONS

The four moments to compare the different probability density function are the mean, variance, skewness and kurtosis. They are calculated as follows:

Mean The mean is the average of the sample set.

$$\mu = \frac{1}{n} \sum_{i=1}^{n} x_i \tag{H.1}$$

Variance The variance is a measure for how big the spread of numbers in the sample set is. The higher the variance the bigger the spread.

$$\sigma = \frac{1}{n} \sum_{i=1}^{n} \left(x_i - \mu\right)^2 \tag{H.2}$$

Skewness The skewness is a measure for how asymmetrical the sample set is around its mean. If the skewness equals zero the sample set is symmetric around its mean. A large negative number indicates a long tail to the left of the mean, whereas a large positive number indicates a long tail to the right of the mean.

$$b = \frac{\frac{1}{n} \sum_{i=1}^{n} \left(x_i - \mu\right)^3}{\left[\frac{1}{n-1} \sum_{i=1}^{n} \left(x_i - \mu\right)^2\right]^{\frac{3}{2}}} \tag{H.3}$$

Kurtosis Kurtosis is also a measure for the shape of a distribution. If g is smaller than zero, it indicates that the distribution is flatter (broad and short) than a log normal distribution. Whereas, a positive number indicates that the distribution is more peaked (small and high).

$$g = \frac{\frac{1}{n} \sum_{i=1}^{n} \left(x_i - \mu\right)^4}{\left[\frac{1}{n} \sum_{i=1}^{n} \left(x_i - \mu\right)^2\right]^2} - 3 \tag{H.4}$$

LIST OF FIGURES

LIST OF TABLES

BIBLIOGRAPHY

[1] *Building a sustainable energy future,* `http://reports.shell.com/sustainability-report/2013/our-approach/building-a-sustainable-energy-future.html`, accessed: 2014-10-28.

[2] *Key World Energy Statistics*, Tech. Rep. (International Energy Agency, 2014).

[3] C. G. C. E. Tzimas, A. Georgakaki and S. Peteves, *Enhanced Oil Recovery using Carbon Dioxide in the European Energy System*, Tech. Rep. (DG JRC Institute for Energy, 2005).

[4] L. W. Lake, *Enhanced oil recovery* (Old Tappan, NJ; Prentice Hall Inc., 1989).

[5] J. Sheng, *Synergistic mechanisms of asp flooding,* `http://www.upstreampumping.com/article/production/synergistic-mechanisms-asp-flooding`, accessed: 2015-06-01.

[6] M. Delshad, D. H. Kim, O. A. Magbagbeola, C. Huh, G. A. Pope, F. Tarahhom, *et al.*, *Mechanistic interpretation and utilization of viscoelastic behavior of polymer solutions for improved polymer-flood efficiency,* in *SPE Symposium on Improved Oil Recovery* (Society of Petroleum Engineers, 2008).

[7] D. H. Kim, S. Lee, C. H. Ahn, C. Huh, G. A. Pope, *et al.*, *Development of a viscoelastic property database for eor polymers,* in *SPE Improved Oil Recovery Symposium* (Society of Petroleum Engineers, 2010).

[8] R. S. Seright, T. Fan, K. Wavrik, R. d. C. Balaban, *et al.*, *New insights into polymer rheology in porous media,* SPE Journal **16**, 35 (2011).

[9] W. Cannella, C. Huh, R. Seright, *et al.*, *Prediction of xanthan rheology in porous media,* in *SPE Annual Technical Conference and Exhibition* (Society of Petroleum Engineers, 1988).

[10] K. S. Sorbie, *Polymer-improved oil recovery* (Springer Science & Business Media, 2013).

[11] T. Sochi, *Flow of non-newtonian fluids in porous media,* Journal of Polymer Science Part B: Polymer Physics **48**, 2437 (2010).

[12] R. B. Bird, W. E. Stewart, and E. N. Lightfoot, *Transport phenomena* (John Wiley & Sons, 2007).

[13] E. Hinch, *Lecture 1: Introduction,* University Lecture.

[14] B. K. Wunderlich, *Complex Microfluidics*, Ph.D. thesis, Technische Universität München (2012).

[15] J. Oldroyd, *On the formulation of rheological equations of state,* Proceedings of the Royal Society of London. Series A. Mathematical and Physical Sciences **200**, 523 (1950).

[16] C. F. F. Vincent A. Hackley, *Guide to rheological nomenclature for liquid-based particle systems,* (2001).

[17] R. G. Larson, *The structure and rheology of complex fluids*, Vol. 4 (Oxford university press New York, 1999).

[18] J. M. Dealy, *Official nomenclature for material functions describing the response of a viscoelastic fluid to various shearing and extensional deformations,* J. Rheol **39**, 253 (1995).

[19] C. J. Petrie, *Extensional viscosity: A critical discussion,* Journal of non-newtonian fluid mechanics **137**, 15 (2006).

[20] K. F. J. Denys, *Flow of polymer solutions through porous media* (TU Delft, Delft University of Technology, 2003).

[21] F. T. Trouton, *On the coefficient of viscous traction and its relation to that of viscosity,* Proceedings of the Royal Society of London. Series A **77**, 426 (1906).

[22] D. Binding, *Contraction flows and new theories for estimating extensional viscosity,* in *Techniques in Rheological Measurement* (Springer, 1993) pp. 1–32.

[23] Y. Masuda, K.-C. Tang, M. Miyazawa, S. Tanaka, *et al.*, *1d simulation of polymer flooding including the viscoelastic effect of polymer solution,* SPE reservoir engineering **7**, 247 (1992).

[24] G. Hirasaki, G. Pope, *et al.*, *Analysis of factors influencing mobility and adsorption in the flow of polymer solution through porous media,* Society of Petroleum Engineers Journal **14**, 337 (1974).

[25] F. Durst, R. Haas, and B. Kaczmar, *Flows of dilute hydrolyzed polyacrylamide solutions in porous media under various solvent conditions,* Journal of Applied Polymer Science **26**, 3125 (1981).

[26] T. G. Mezger, *The rheology handbook: for users of rotational and oscillatory rheometers* (Vincentz Network GmbH & Co KG, 2006).

[27] V. Castelletto, I. Hamley, W. Xue, C. Sommer, J. Pedersen, and P. Olmsted, *Rheological and structural characterization of hydrophobically modified polyacrylamide solutions in the semidilute regime,* Macromolecules **37**, 1492 (2004).

[28] R. Haas and F. Durst, *Viscoelastic flow of dilute polymer solutions in regularly packed beds,* in *Progress and Trends in Rheology* (Springer, 1982) pp. 212–217.

[29] T. J. Ober, S. J. Haward, C. J. Pipe, J. Soulages, and G. H. McKinley, *Microfluidic extensional rheometry using a hyperbolic contraction geometry,* Rheologica Acta **52**, 529 (2013).

[30] Padding, J.T. and De, S., personal communication (2014).

[31] G. M. Whitesides, *The origins and the future of microfluidics,* Nature **442**, 368 (2006).

[32] M. S. N. Oliveira, M. A. Alves, F. T. Pinho, and G. H. McKinley, *Viscous flow through microfabricated hyperbolic contractions,* Experiments in fluids **43**, 437 (2007).

[33] C. J. Pipe and G. H. McKinley, *Microfluidic rheometry,* Mechanics Research Communications **36**, 110 (2009).

[34] A. Dupas, I. Hénaut, J.-F. Argillier, and T. Aubry, *Mechanical degradation onset of polyethylene oxide used as a hydrosoluble model polymer for enhanced oil recovery,* Oil & Gas Science and Technology–Revue d'IFP Energies nouvelles **67**, 931 (2012).

[35] J.-F. Argillier, A. Dupas, R. Tabary, I. Henaut, P. Poulain, D. Rousseau, T. Aubry, *et al.*, *Impact of polymer mechanical degradation on shear and extensional viscosities: Toward better injectivity forecasts in polymer flooding operations,* in *SPE International Symposium on Oilfield Chemistry* (Society of Petroleum Engineers, 2013).

[36] Ober, T. and e-VROC vendor, personal communication (2014).

[37] I. O. Wiegmann, A. and A. Schindelin, *Computer aided engineering of filter materials and pleated filters,* Global Guide of the Filtration and Separation Industry , 191 (2010).

[38] *Simulation Software for All Fluid Flow Applications,* `http://www.comsol.com/cfd-module`, accessed: 2015-02-11.

[39] H. Dong and M. J. Blunt, *Pore-network extraction from micro-computerized-tomography images,* Physical Review E **80**, 036307 (2009).

[40] *Berea sandstone,* https://www.imperial.ac.uk/engineering/departments/earth-science/research/research-groups/perm/research/pore-scale-modelling/micro-ct-images-and-networks/berea-sandstone/, accessed: 2015-6-03.

[41] Romate, Johan, *A vector secant method for simultaneous solution of scalar nonlinear algebraic equations.* personal communication (2015).

[42] R. Armstrong, N. Evseev, O. M. Gurpinar, L. A. Hathon, D. V. Klemin, O. Dinariev, S. Berg, S. Safonov, M. Myers, H. de Jong, *et al.*, *Application of digital rock technology for chemical eor screening,* in *SPE Enhanced Oil Recovery Conference* (Society of Petroleum Engineers, 2013).

[43] K. Haraguchi, *Synthesis and properties of soft nanocomposite materials with novel organic/inorganic network structures,* Polymer journal **43**, 223 (2011).